Identifying the ejected population from disintegrating multiple systems

by

Alexandra Ka Po Yip

A Masters Thesis submitted to

The University of Hertfordshire

In partial fulfilment of the requirements

of the degree of

MSc BY RESEARCH

Centre for Astrophysics Research

School of Physics Astronomy and Mathematics

The University of Hertfordshire

September 2015

Abstract

Kinematic studies of the Hipparcos catalogue have revealed associations that are best explained as disintegrating multiple systems, presumably resulting from a dynamical encounter between single/multiple systems in the field (Li et al. 2009). In this project I have searched for disintegrating multiple systems in three database/catalogues; Dwarf Archive, the Hipparcos Main Catalogue, and the Gliese-Jahreiß Catalogue. My techniques were able to identify systems containing stars, as well as star/brown dwarf components. Distance constraints from parallax and spectrophotometry allowed me to identify common distance associations. Proper motion measurements allowed me to separate common proper motion multiples from my sample of disintegrating candidates. And proper motion and positional information allowed me to select candidate systems based on relative component positions that were tracked back and projected forward through time. Four candidate disintegrating multiple systems have been identified, all quadrupoles. One of these four systems contains a UCD (GJ 570 D). Another consists mainly of known members of the open cluster IC 2602, and the other two systems consist of M-K dwarfs and K dwarfs respectively. In addition I have identified two candidate disintegrating double systems, each containing one UCD component. The first one consists of a T1 dwarf and a white dwarf. The second one (the eta CrB system) has been previously identified as a bound multiple system, though my analysis suggested it could be disintegrating. In addition I have identified three multiples (previously unreported or with un-reported components) with component spectral types of; K1+K5 (spectroscopic binary), M0+M2 and M1+M3.5+M4. I discussed the properties of all these systems as well as the sample overall, considering sources of uncertainty and contamination, and discussed future work on the sample and to expand this area of research.

Acknowledgements

I would like to thank my principal supervisor Professor David Pinfield and second supervisor Doctor Ben Burningham for giving me the wonderful opportunity to work on this extremely interesting project, and for giving me all the support I needed in order to complete this research. I would also like to thank Dr Jim Collett and Dr Andreas Georgiou for all the support in various areas, in addition to the continuous supplies of tea and snacks whenever I hit a mental block. I would very much want to thank Dr Federico Marocco for supporting me through thick and thin in any possible way you can think of. Big thanks to Dr Philp Taylor for all the technical support from the side-line. Furthermore, all of the friendly and helpful staffs and colleagues from the Centre of Astrophysics Research (CAR), my aunties and uncles who always believed in me, and my friends Melody Wong, Suki Wong, Karen Conroy and Ian Conroy whom always give me helpful advice dealing with life issues on the side, so I can concentrate on my work. Special thanks to Mr. Fu, my secondary school science teacher, who I am sure follows my progress from above, whose wonderful teaching resulted in me clicking then falling for science. Last but not least, I would have not been able to complete this MSc without the full support from my mum Jenny Ng spiritually and financially.

Contents

List of Figures

List of Tables

In this Thesis

The main findings of my research will be presented in this Thesis. I will discuss topics in the light of current published data and theories, in addition with the implications and new opportunities offered by these results for future study in these particular areas. In the first chapter, I will present sufficient background in this field with related literature to explain the importance of my work and how my research provides a significant contribution to knowledge in these areas. The set of requirements I used to select my candidate systems and methods applied in this work will be listed and described in Chapter 2. The results obtained by this project and discussion thereof shall be reported in Chapter 3. Finally, the future work and conclusions of my findings will be present in Chapter 4.

Chapter 1

1. Background

1.1 Introduction

The theory of brown dwarfs was first proposed by Kumar (1963). From the properties of completely convective models of stars from 0.09 to 0.04 solar masses, assuming non-relativistic degeneracy of the stellar material, Kumar noticed a lower limit to the mass of a main sequence star, which was approximately 0.07 solar masses ($M_\odot$). The most up-to-date value of the minimum mass for hydrogen-burning is $\sim 0.075\ M_\odot$. Stars whose mass is below this limit will not go through the normal stellar evolution, due to the fact that the potential energy produced by gravitational contraction is not sufficient to ignite hydrogen fusion in their core. These objects were therefore considered failed stars and were called 'Black Dwarfs' at the time. Though there were a few other names suggested beside 'Black Dwarf' (e.g. 'Infrared Dwarf'; Davidson 1975), none of them was unambiguous. Hence the need for a new name for these intermediate objects became urgent. It was then that Tarter (1975) suggested in her Ph.D. thesis the term 'Brown Dwarf', because the colour 'Brown' in a colour palette is somewhere between 'Red' and 'Black'. This new name has been accepted by the 'sub-stellar objects community' and has become widely used nowadays.

Since these objects are intrinsically faint due to the lack of fusion, the first brown dwarf candidate, GD 165B, was observed only in the late 1980's with the aid of infrared telescopes by Becklin & Zuckerman (1988), orbiting around a white dwarf (however GD 165B at the time was not recognised as a brown dwarf). The first two unambiguous brown dwarfs, GL 229B (a T7 dwarf with a mass of 20-50 M_J, companion to an M1 dwarf; Nakajima et al. 1995) and Teide 1 (found in the Pleiades cluster as a free-floating M8 dwarf with a mass of 40-70 M_J; Rebolo et al. 1995) were discovered only another 7 years later. The number and type of brown dwarfs discovered increased exponentially as infrared technology advanced with the improvement in the sensitivity of the instruments, and led to the extension of the Morgan-Keenan spectral classification system of stars (Morgan, Keenan, & Kellman 1943), with the introduction of three new spectral classes: L, T (Burgasser et al. 2002; Geballe et al. 2002; Kirkpatrick 2005; Burgasser et al. 2006a), and more recently Y (Cushing et al. 2011). In the past years, astronomers have been using observations to improve our understanding of how brown dwarfs form, their mass spectrum (the sub-stellar initial mass function; IMF), and their atmospheric properties.

Brown dwarfs are found either as field objects or as cluster/moving group members. They have been observed as isolated objects, in binary systems (i.e. brown dwarf-brown dwarf; star-brown dwarf) and also in higher order multiple systems (see https://jgagneastro.wordpress.com/list-of-ultracool-dwarfs/ for a census of known ultracool dwarfs).

Dynamical interactions of these multiple systems with nearby stellar objects/multiples could lead to the disintegration of the system. There has been some limited analysis of disintegrating multiple systems in the field using Hipparcos data (Li et al. 2012). Other related studies in the disintegrating

multiple systems domain are the numerical experiments on binary-binary encounters (Mikkola 1983), the dynamical evolution of star clusters (e.g. Aarseth 2004), focusing in particular on the slingshot mechanism as one of the formation scenario for triple systems (due to binary-binary encounters; Saslaw et al. 1974) in addition to simulations on the effect that negative total energy has on triple systems (e.g. Anosova 1990).

In this thesis, I have used parallaxes and proper motions provided from astrometric surveys of stellar objects and brown dwarfs to look for the evidence of disintegrating multiple systems with cool nearby components. I have identified a set of possible candidate systems which can be used to search for additional fainter objects in these associations using surveys including UKIDSS, SDSS, VISTA and WISE. This work will contribute further clues to the limited study on the probability of cool objects being ejected by disintegrating systems, as well as introducing an alternative route to locate those extra dim objects.

In the following sections of chapter 1, the background information on ultra-cool dwarfs (population's properties, spectral types, etc.) will be presented in section 1.2. Then in section 1.3, I will describe the definition as well as the formation theories for these cool objects. I will then discuss in section 1.4 the properties and proposed formation theories for multiple systems, as well as the dynamical interactions that can lead to their disintegration. Last, the motivation for this thesis will be presented in section 1.5.

1.2 Ultra-cool populations

Among the population of celestial objects those with effective temperature below 2500 K ($\lesssim$ M7) are generally referred to as ultra-cool dwarfs. This class includes very low-mass stars (hereafter LMSs), brown dwarfs (hereafter BDs) and giant extrasolar planets (hereafter ESPs), and it is in particular on the last two types of objects that I will focus in this thesis, as possibly ejected members of disintegrating multiple systems. A more detail discussion of the properties of these ultra-cool objects will be present in the following sections.

1.2.1 Effective temperature

To clarify, ultra-cool dwarfs (hereafter UCDs) as mentioned above is a temperature-based definition, referring to objects that have effective temperature (T_{eff}) that are below 2500K, whereas BDs are objects that have a mass that is below $0.075\mathrm{M}_{\odot}$. Hence not all UCDs are BDs. For example, LMSs will cool, but eventually reach a minimum luminosity they can maintain through steady internal fusion, becoming early L spectral type UCDs. On the other hand, since BDs cannot sustain stable hydrogen burning, they will just darken gradually over their lifetime while most of the energy produced from gravitational contraction is radiated away.

There are four types of UCDs observed up to date: M, L, T and Y. One of the main differences between them is their T_{eff}. Most M dwarfs are stars and have T_{eff} ranging between 2300K and 3800K whereas the T_{eff} for L dwarfs is approximately between 1400K and 2300K. The T_{eff} of T dwarfs is from around 500K to 1400K and since Y dwarfs are cooler than the T dwarfs so their T_{eff} is below 500K. I will explain the atmospheric differences that occur with the temperature changes in section 1.2.3 to 1.2.6 below.

Both the age and mass of these sub-stellar objects influence the distribution of their T_{eff} and luminosity (i.e. (Luminosity, T_{eff}) = Function (Mass, Age); lower mass BDs are cooler and fainter than the more massive ones of the same age but are physically larger) and can be predicted by

evolutionary models (i.e. Chabrier & Baraffe 2000; Saumon & Marley 2008; Allard et al. 2013; Allard 2014). The evolution of T_{eff} (in K) with age (in Gyrs) for various objects of various masses (e.g. LMSs, BDs and ESPs) is shown in Figure 1.1 (Figure 8 from Burrows et al. 2001). The blue lines represent the stars and the green lines correspond to BDs that have mass above 13 M_J (the deuterium limit) whereas the BDs and ESPs that have mass equal or below 13 M_J are shown by red lines. The gold dots mark the ages for a given mass at which 50% of the deuterium has been burned and the magenta dots mark, for a given object, when 50% of the lithium has been burned. The horizontal dashed lines indicated the approximate realms for the L and T dwarfs as the regions of L and T dwarf are still poorly determined. It also shows that the majority of BDs evolve from spectral types M (late) to L to lastly T.

Essentially, stars at the lowest mass end contract at a rapid rate as pre-stellar objects; hence they undergo a decline in luminosity in the first phases of their evolution. They will then join the main sequence and become stable due to the energy output from the fusion within their core. Their radius, luminosity and T_{eff} remain constant throughout their lifetime and become late M or early L dwarfs, and reach relatively compact states where the radius is roughly equivalent to the radius of Jupiter.

At the beginning of the evolution of these low-mass stars and high-mass BD, there is a short deuterium burning phase (within ~20 Myr) depending on their mass (Chabrier & Baraffe 2000). Sub-stellar objects will then carry on with their contraction, cooling and fading slowly and steadily. They will then evolve from spectral type M to L then T and the least massive ones will eventually become Y dwarfs.

Sub-stellar objects below the deuterium burning limit such as low-mass BDs and planets never reach the tremendously compact phases where their radii stabilize to approximately the radius of Jupiter, which is typical at the higher mass end of the BDs regime.

In general, the radius of a stellar object is approximately a linear function of its mass when it is young. On the other hand sub-stellar objects undergo a mass-radius relation inversion after ~100 Myr. Originally more massive brown dwarfs will end up with smaller radii (the objects with the largest radii are those with mass around 4 M_J, e.g. Zapolsky & Sappeter 1969; Hubbard 1977) as their internal structure is under the influence of electron degeneracy pressure, and the electron density is the only parameter that plays a role. In this case, more massive objects become extremely dense in order to balance their higher self-gravity.

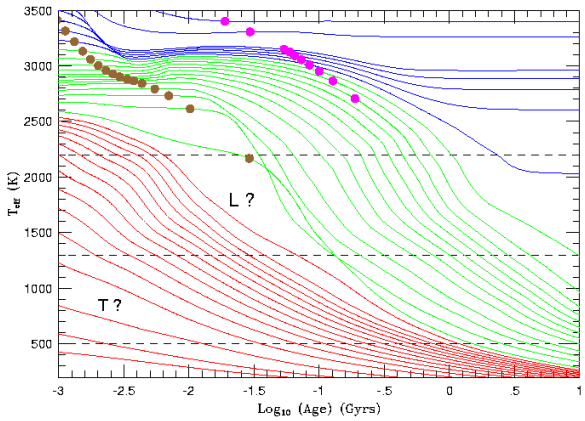

Figure 1.1: The evolution of T_{eff} (in K) with age (in Gyrs) for various mass such as LMSs, BDs and ESPs (Figure 8 from Burrows et al. 2001).

1.2.2 Spectral type distribution

The Morgan-Keenan (MK) system of classification (Morgan, Keenan, & Kellman 1943) is the standard stellar classification for stars based on their spectral characteristics. The measurement of the photospheric temperature of an object can describe the ionization of its photosphere. Analysing it can help deduce the chemical elements present in the candidate object from the absorption lines in the spectrum. The temperature conditions that are necessary for a certain excitation of those elements can be determined from the spectrum as well.

The different spectral classes being used for main sequence stars are OBAFGKM (Morgan, Keenan, & Kellman 1943), where type O indicates the most massive and hottest stars and type M indicates the smallest and coolest stars in the main sequence, hence lying in the red part of the spectrum. There is a number accompanying each letter between 0 and 9 representing tenths of the range between two classes. To determine the spectral type of a star, both its optical spectrum and NIR spectrum are used. More often astronomers use optical spectra for O to M as they are more temperature dependent (Morgan, Keenan, & Kellman 1943) and the majority of the flux is emitted at optical wavelengths. In addition, the earlier spectral types in the main sequence are determined via atomic lines but molecular absorption bands are used to classify M dwarfs as these bands start to appear in G stars and strengthen along K and M.

Spectral type L (Kirkpatrick et al. 1999), T (Burgasser et al. 2006a) and Y (Burrows et al., 2003; Kirkpatrick 2008) were later added to the previous MK system after the discovery of GL 229B by Nakajima et al. (1995). Note that while the temperature of these sub-stellar objects drops, dust grains and clouds start to form. In addition, their metallicity and surface gravity also play an important role in affecting their spectral type.

Kirkpatrick et al. (1993) was the first group to analyse the spectrum of GD 165B and deduced it to be an intermediate transition object between stars and giant planets. In general, the spectrum of GD 165B lacks common and typical feature of M dwarfs such as the absorption bands of titanium(II) oxide (TiO). Additionally, it cannot be a planet either due to the absence of the spectral features of Jupiter and Saturn, methane (CH_4) and ammonia (NH_3) respectively. However, the first unambiguous brown dwarf ever observed was GL 229B, by Nakajima et al. in 1995. Not only the absorption bands of CH_4 can be seen in its spectrum, but it also shows a general similarity with the spectrum of Jupiter (Oppenheimer et al. 1998). PPI 15 and Teide 1 in the Pleiades were also identified to be BD candidates around the same time (Stauffer et al. 1994; Rebolo et al. 1995) and lithium (Li) was detected in their spectra for the first time; they were then confirmed to be sub-stellar objects as well (Basri et al. 1996; Rebolo et al. 1996).

As more and more of these new objects were found it became clear that they belonged to two different groups. The spectra of some of these newly found sub-stellar objects were similar to GD 165B, therefore very different from M dwarf. Additionally, objects with spectra similar to GL229B showed a clear distinction from both M dwarf and GD 165B alike. This made necessary an extension to the MK system of classification and two new spectral classes were then added. Type L was introduced for GD 165B type of objects and type T was introduced for GL 229B type of objects (Kirkpatrick 2005). An example of spectral sequence from M dwarfs to giant planets is shown in Figure 1.2 (reproduced from Cushing et al. 2006).

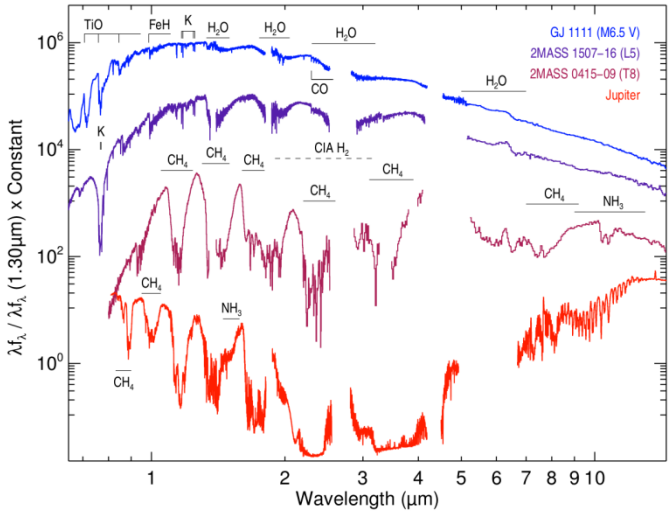

Figure 1.2: An example of spectral sequence, showing a late M dwarf (in blue, at the top) a L dwarf (in purple), a T dwarf (in magenta) and the spectrum of Jupiter (in bright red, at the bottom). The differences between the 4 types of object are clear (Cushing et al. 2006).

However, even cooler objects were being discovered continuously (e.g. Lucas et al. 2010; Liu et al. 2011) but the coolest and faintest objects identified to date were found by the latest NASA IR satellite WISE (Kirkpatrick et al. 2011; Cushing et al. 2011).

A more detailed description of the spectral types will be given in the following sub-sections.

1.2.3 M dwarfs

M dwarfs are a mixture of cold and old low-mass hydrogen burning stars as well as high-mass and young BDs. Only the very young BDs are hot enough to be late M dwarfs i.e. from $\sim$M6.5 and onward. An example of these young BDs are the members of the young open cluster Pleiades which have an estimated age of $\sim 100 - 200\ Myr$. In 1991, one way to classify objects between K5 to M9 was suggested by Kirkpatrick et al. (1991), where spectral features as well as the spectral slope around the 6300 to 9000 Å region was used. This is because the peak of the spectral energy distribution of M dwarfs, as well as the main absorption features, are located in the redder part of the optical spectrum because of their lower temperature (Berriman & Reid 1987; Liebert et al. 1984).

The most characteristic features of M dwarfs across the red part of the electromagnetic spectrum are the absorption bands of water (H_2O) and the weakening metal-oxide bands. TiO is found in K7 to M6 dwarfs and produces especially strong absorption bands in the early-M dwarf's spectra. Vanadium oxide (VO) is also found in late-type objects (e.g. Kirkpatrick et al. 1991). The presence of metal hydrides such as iron(I) hydride (FeH), magnesium hydride (MgH) and calcium hydride (CaH) also causes additional important absorption bands for this spectral type. Ca I, Na I, K I and Ca II cause the main atomic lines within M dwarf's optical spectra.

1.2.4 L dwarfs

The following spectral class is type L which was defined and categorized by Kirkpatrick et al. (1999) for the optical spectra and Geballe et al. (2002) for the NIR spectra. L dwarfs contain a mixture of old LMSs and intermediate age BDs. The combination of both atomic lines and molecular absorption

bands can be found in the spectra of early-Ls. The most prominent lines and bands that were used to distinguish L dwarfs from other low-mass objects are caused by the presence of alkali metals such as Na, K, rubidium (Rb) and cesium (Cs), metal-oxides (mainly TiO and VO) and hydrides such as chromium(II) hydride (CrH), FeH, MgH and CaH. The absorption lines of Na and K start to deepen while the absorption bands of TiO and VO become shallow and almost invisible for objects in mid-L spectral classes. Then in the spectra of late-Ls, it can be seen that the bands of $\mathrm{H_2O}$ have deepen while hydrides bands have become weaker. Moreover, the deep line of calcium (Ca) and the strong band of carbon monoxide (CO) at wavelength $\sim 2.1\ \mu m$ and $\sim 2.3\ \mu m$ respectively are the main sources of opacity in the red end of the spectra (i.e. $\sim 2 - 2.3\ \mu m$).

More complex molecules are "trapped" into dust grains that form layers of clouds inside the photosphere of L dwarfs, having a strong influence in shaping the emergent spectral energy distribution (e.g. Helling et al. 2008; Helling & Casewell 2014). In addition, while Rayleigh scattering by dust clouds reddens emerging flux, warm dust can also "re-warm" the atmosphere.

Though the optical and the IR classification schemes are influenced by different atmospheric phenomena, yet numerous studies showed that, with a few exceptions, optical-based and IR-based L spectral types overlap (i.e. Reid et al. 2001b; McLean et al. 2003).

1.2.5 T dwarfs

As time progressed, more low-mass objects were discovered and it was the discovery of GL 229B (Nakajima et al. 1995) that forced the introduction of the new spectral class T. Its classification scheme based on optical spectra was defined by Burgasser et al. (2003b). Nevertheless, as most T dwarfs are too faint for optical spectroscopy, the classification scheme based on NIR spectra by Burgasser et al. (2006a) is the one being widely used. There are solely BDs in this class as hydrogen burning stars never become cold enough to be T dwarfs. In addition, due to the prominent CH_4 absorption bands that can be observed within their spectra, T dwarfs are also called methane dwarfs. Moreover, hydride bands disappear in this class while the depth of H_2O bands increases as they become the main absorbers in the mid- and late-T type objects. Furthermore, the absorption lines from alkali metals (Na and K) in the optical spectrum are on the edge of merging due to their depth and width (Burgasser et al. 2006a). Separated by the absorption bands of CH_4 and H_2O, the four peaks (1.08, 1.27, 1.59 and 2.08 μm) in the spectrum are a characteristic of late-T spectra (note that the CIA of H_2 causes the peak at $\sim 2.08\ \mu m$ to be further damped as well as T dwarfs to look relatively blue in terms of NIR colours, besides the absence of dust).

1.2.6 Y dwarfs

The coolest objects discovered so far are classified as Y dwarfs. They share similar masses and temperatures as gas giant planets. Although the theory have not yet been confirmed, but the existence of H_2O clouds in these objects at 300-400K have been predicted (Morleys et al. 2014). Only a few of these cool objects have recently been discovered (Cushing et al. 2011; Kirkpatrick et al. 2011) and the archetypal Y Dwarf is WISEP J1828+2650 (Cushing et al. 2011). The classification scheme is only preliminary due to the limited sample size, but from the spectra obtained by Kirkpatrick et al. (2012) some peculiar characteristics have been identified, which can be used to distinguish type Y from type T. Model atmospheres of cool BDs predict the hotter T dwarfs, which are blue in NIR colours, turn red again when their T_{eff} drops between 300 and 400K, because the blue tail of the spectral energy distribution collapses. Consequently, the turning to the red of the NIR spectrum was one of the triggers forcing the creation of a new Y spectral type (Burrows et al. 2003; Kirkpatrick 2008).

Y dwarfs show absorption bands of H_2O, CH_4 and NH_3, which begin to play a more important role in shaping the NIR spectra. Note that moving to later types, H_2O bands become deeper, while atomic lines become shallower. On the other hand, Na condenses out of the gas phase into sodium sulfide (Na_2S), and K as well be condenses into clouds as potassium chloride (KCl), hence their lines in the optical spectrum become weak. Though, at T_{eff} of approximately 350K, a reasonable amount of H_2O, CH_4 and NH_3 condenses into clouds too, and since all three bands blend together the detection of the NH_3 is a challenge (note that only if the spectra have high enough signal-to-noise ratio, NH_3 might be observable in the H-band in some Y dwarfs).

1.3 Brown dwarfs

BDs are known as intermediate objects between stars and planetary mass objects, and hold the key to bridging the gap between the two. Although BDs are faint and difficult to detect and measure, they are far from being rare. The number ratio of brown dwarfs to stars, possibly dependent on their environment, according to various surveys vary between 1/6 and 1/3 (e.g. Luhman et al. 2007; Kirkpatrick et al. 2012, Scholz et al. 2012).

1.3.1 Difference between brown dwarfs and planets

The line drawn between BDs and giant exoplanets is rather fine. The limited understanding of these faint objects lead to the development of a working definition (which will evolve as the knowledge of the subject grows with additional data being gathered) by the International Astronomical Union (IAU). These statements compromise between definitions and are based solely on formation mechanism or on the deuterium-burning mass. Though, numerous astronomers have a preference on the formation-based definition (see Pinfield et al. 2013), however, for it to become practical, further progress in both observational techniques and theoretical modelling is necessary. The working definition of brown dwarfs and planets was first issued on 28 Feb 2001 and last modified 28 Feb 2003 (Boss et al. 2003), exactly as follows:

- Objects orbiting around solar-type stars with true masses above the limiting mass for the thermonuclear fusion of deuterium (currently calculated to be 13 Jupiter masses for objects of solar metallicity) are “brown dwarfs” (no matter how they formed), while objects with true masses below this limiting mass are “planets”.

- Free-floating objects in young star clusters (which presumably formed in the same manner as stars and have not been shown to be ejected from planetary systems) with masses below the limiting mass for thermonuclear fusion of deuterium are not “planets,” but are “sub-brown dwarfs” (or whatever name is most appropriate).

In other words, if a sub-stellar object has true mass $0.013 < M_{\odot} < 0.075$ it is currently considered to be a “brown dwarf” regardless of how it was formed or where it is located. The lower limit of the interval, $0.013\ M_{\odot}$, is the deuterium-burning limit, here consider the cut-off between planets and BDs, and $0.075\ M_{\odot}$ is the hydrogen-burning limit which is the cut-off between stars and BDs.

1.4 Multiple systems

When two stars in a star system (primary and secondary) orbit around their common centre of mass, they are called a “binary star”, and this is due to the gravitational pull/interaction between them (same principle for multiple systems). The primary in this case is the brighter/more massive star between the two and the dimmer/less massive one is called the secondary or companion star. The secondary could be either a sub-stellar object or a main-sequence star. There is observational

evidence from the study of a few pre-main-sequence systems indicating a strong likelihood for both components to be born very closely in time, with a maximum difference of about 10^6 years (e.g. Bodenheimer, Ruzmaikina, & Mathieu 1992; Strom 1991). The secondary shares the same metallicity as well as the same age of the primary, given they both originate in a short time interval, giving extra constraints on its composition and mass (e.g., Burgasser et al. 2000a). Further, if the components are consistent with having equal brightness this implies that they are likely to be a near equal mass binary. Furthermore, there is evidence that binary systems (independently of their range of orbital periods) and isolated young stars are more likely to have a disk around them (Mathieu 1992).

One of the fundamental goals for this project is to look for disintegrating multiple systems, which are considered to be extremely rare. The estimated amount of single stars is approximately $2/3$ of the total stellar population of the Milky Way, while $1/3$ of it consists of binaries or multiple star systems (Lada 2006). Moreover, hierarchical multiple systems are relatively common and according to Fekel (1981), most of their period ratios are usually within the range of $10 - 10^4$ (e.g. our Earth is a primary to our moon with a short period of a month, and our Sun is a wide companion to our Earth, with a much longer period of a year). To improve the understanding of these binary/multiple systems, various observational facts such as the non-negligible occurrence of multiple systems, the overall binary frequency, as well as the distributions of eccentricity, period and mass ratio among the individual binaries are still awaiting to be fully explained.

For both close by star-forming regions and inside our solar neighbourhood, LMSs (especially M dwarfs) outnumber by a relatively large margin all other types of star. In addition the star formation process can also be tested by the observation of binary properties. Dynamical interactions, star formation and even the origin of Galactic field stars can be deduced from the chief characteristics of M-dwarf's companions, e.g. mass ratio, separation distribution and multiplicity fraction. For orbital separations in diverse ranges, close by M dwarfs (that have low luminosities and high proper motions) allow the identification of multiple systems and co-moving binaries. Initial studies focused mainly on solar-type stars (Duquennoy & Mayor 1991; Raghavan et al. 2010) but nowadays have been expanded with the first informative study of M dwarfs (Fischer & Marcy 1992) and also of A-type stars (De Rosa et al., 2014).The binary fraction of the least massive stellar objects (also the most common stellar population) became more accurate thanks to these studies that looked for binaries consisting of components with various masses. This is fundamental to understand the formation and nature of stellar and sub-stellar binaries. Brief background/properties of these binary/multiple systems will be present in the following sections.

1.4.1 General properties

There is more than just one type of binary systems, and the way they appear to the observer is one of the main characteristics used to classify them. A basic review of the types of binary will be in the next section.

1.4.1.1 Observational classification of binary system

Overall, there are four main types of binaries, each one further divided into a variety of sub-types. The first main type is the Visual Binaries (e.g. the Castor system), where the periodic motion of both components is observable in the sky (e.g. Dupuy & Liu 2012). One variety of this type are called Astrometric Binaries when only the motion of one star is visible (and can be detect optically). Astrophysicists can obtain from visual binaries their orbital pattern (e.g. McCaughrean et al. 2004), but a lot of them have very long orbital periods of a few centuries (or even millennia) leading to poorly known or very uncertain orbits.

Another way in which binaries can be detected is via indirect techniques such as spectroscopy. The binary components' orbital motion causes periodic Doppler shifts, which are detectable in one or more spectral lines, hence the name Spectroscopic Binaries. When the Doppler shifts are measurable for both binary components then the system is called double-lined spectroscopic binary. Otherwise, the system is named single-lined spectroscopic binary when only one of the component's Doppler shift can be measured. In addition, the time variation of these spectroscopic binaries's spectrum can also be obtained (e.g. Burgasser et al. 2010).

Another type of binary systems is the Photometric Binaries, where the colour (or flux) of the system appears to have a periodic variation. However, this is not a reliable way to be certain that these systems are real binaries, as they can be confused with variable stars (e.g. Cepheids, RR Lyrae variables) since they can as well have similar periodic variations.

The last main type of binary systems is the Eclipsing binaries, where during part of the orbit, one star eclipses the other (i.e. one star passes in front of the other, causing a significant variation in the light output for the system). Depending on the inclination of the orbit relative to the line of sight, the binary will only eclipse if the orbit is aligned with the line of sight, or is tilted by a very small angle. If the orbit is tilted by a large angle, then the binary will not eclipse. This type of binaries is fundamental to determine basic stellar parameters of stars (i.e. mass and radius).

Ultimately, these binary systems are fundamentally important because astronomers can obtain the masses of their components by calculating their orbits (e.g., Zapatero Osorio et al. 2004). In addition, their subsequent evolution and their formation can be revealed by their orbit. Once the orbit of these binary/multiple systems is determined, scientists can then find out the amount of angular momentum in the system by looking at the mass of the components and the period of the binary.

1.4.1.2 Orbital period properties and eccentricities of binary system

Binary/multiple systems can either be so close to the point of almost being in contact with each other ($\sim$ a few AU or nearer) or so far apart ($\sim$ a few hundreds of thousands AU) that one can only indicate that they are indeed in connection by looking at their common proper motion. Generally, the separation of binary/multiple systems determines their orbital period (P_{orb}), ranging from $\sim$ 11 mins to 10^6 yrs (Podsiadlowski 1989). The larger the separation the longer the P_{orb}, and vice versa. Furthermore, Duquennoy and Mayor (1991) found the period distribution of main-sequence binaries in the range 0 < log P_{orb} (days) < 9 to be unimodal and best described by a Gaussian-type relation (a smooth distribution) with a median period (single maximum) of approximately 180 years, where each decade of log P_{orb} contains 10% of the systems from 10^{-3} yrs to 10^7yrs. It is handy to bear in mind that for a relatively approximate period distribution, the distribution in log P_{orb} is logarithmically flat (i.e. $f(\log P_{orb}) \simeq constant$).

Moreover, given that binaries/multiple systems are likely to have formed with a wide range of eccentricities, there is also a relationship between the eccentricity of the orbit and the period of a binary star. Field main-sequence binary systems, where the eccentricity is small and with a short period (i.e. $P_{orb} < 10\ d$) end up being circularized via tidal interactions, while if the separation between the components is wide, then a highly elliptical orbit is possible (Duquennoy & Mayor 1991). The distribution of eccentricities for these systems is in general widely scattered $e \equiv \sqrt{1 - b^2/a^2}$, where *a* is the semi-major axis and *b* is the semi-minor axis.

The eccentricities from well-determined orbits are essential to derive the angular momentum of the formation process. This information can then be used to estimate other stellar parameters indirectly,

such as density and radius. Prior of having their empirical mass-luminosity relationship determined, then the masses of single stars can also be estimated. Mass is the fundamental property of any stellar object, since it can be used to determine its entire life history.

On the other hand, some properties of relatively low-mass binaries, i.e. multiplicity fraction, orbital semi-major axes, and mass ratio can be studied in a statistical way by using a large sample without the information of orbital motion. These studies have given very important constraints on formation models at very low masses (e.g. Allen 2007). An example can be seen in Figure 1.3, showing the period distribution of BDs companions to main sequence stars. There is a clear lack of short period binaries (i.e. P < 100 days) compared to long period binaries (i.e. 100 < P < 10000 days). This is known as the "brown dwarf desert" (e.g. Ma & Ge 2014; Stamatellos & Herczeg 2015).

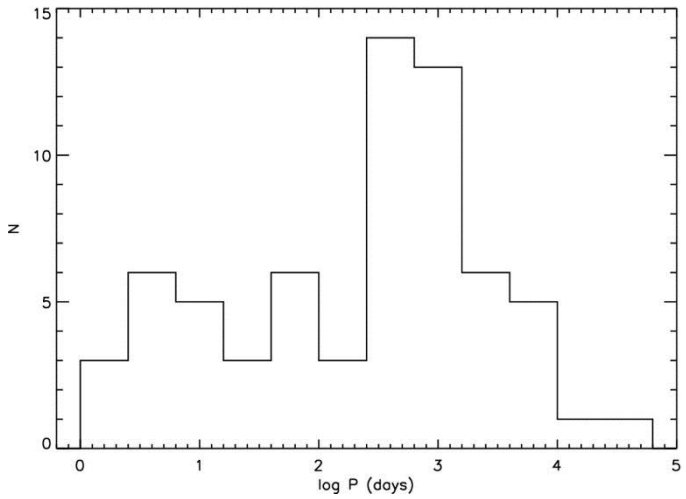

Figure 1.3: The period distribution of BDs companions to main sequence stars, from Ma & Ge 2014 (Fig.1). Long period binaries are much more numerous than short period binaries.

1.4.1.3 Mass ratio distribution

To have a reliable set of constraints on the formation models is fundamentally important to determine the possible dominant formation scenario for various stellar objects, especially very low-mass stars. Naturally, the knowledge of the properties of these very dim objects will aid providing the set of constraints necessary. The mass ratio distribution (i.e. $q = \mathrm{M}_2/\mathrm{M}_1$, where M_1 is the primary and M_2 is the secondary) is one of the properties of low-mass binaries that can provide appropriate constrains to the formation models. Though *q* seems to be dependent on the mass regime, but none the less is not precisely determined. Generally, if the primary star is massive then there is a much higher likelihood for the secondary to be in a similar mass regime. However, there is not a similarly clear pattern for LMSs. Although the exact numbers are not known, binary surveys have suggested that massive stars have a higher fraction of interacting binary systems of 50% compared to lower mass objects, where the fration is 30% (e.g. Duquennoy & Mayor 1991; Kobulnicky & Fryer 2007). The inconsistence in mass ratio distribution between massive stars and LMSs reveals a possible difference in the still uncovered formation process.

Further, Abt in 1983 suggested that by selecting random pairs from a population of objects, assuming that they follow the Salpeter IMF, their mass ratio distribution would match that for long period binary systems, or in other words there are more systems with long period that have small *q* than large *q*. However this statement was disputed by both Duquennoy & Mayor (1991) and

Halbwachs (1987), because they believed Abt (1983) have not provided any/enough evidence to support his theory, and they suggested the binary period is actually independent of the *q* distribution. To defend his pervious statement in 1983, in 1987 Abt claimed that there is a pattern where binary systems with higher *q* tend to have in general a shorter period. More in depth studies are necessary in order to fully support Abt's new statement.

Moreover, the mass ratio between the components has an important role in determining the binary fraction, and at $q \sim 1$ is where the distribution peaks for all of the very low mass binaries discovered so far. The mass ratio distribution of very low mass binaries (spectral type > M6) known to date is presented in Figure 1.4 (taken from Burgasser et al. 2007). The systems with age below 10 Myr are represented by shaded bins, with the number of binaries in each bin labelled.

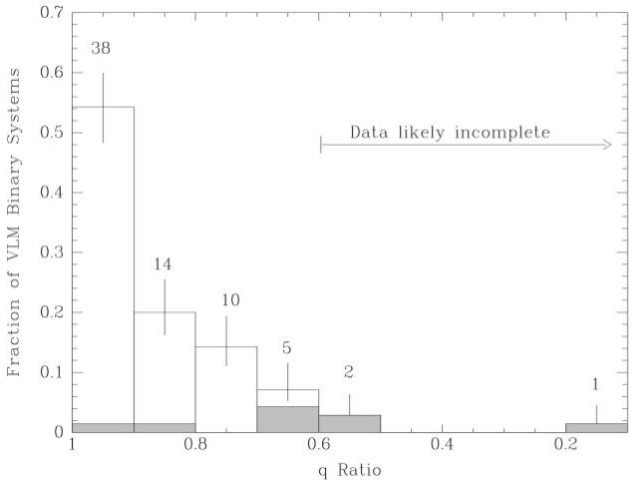

Figure 1.4: Mass ratio distribution of very low mass binaries (spectral type > M6) known to date (taken from Burgasser et al. 2007). The systems with age below 10 Myr are represented by shaded bins, with the number of binaries in each bin labelled.

It is important to bear in mind that there might be a bias in the selection of the observed mass ratios, leading to a less accurate separation distribution. Especially when the secondary is much less massive than the primary, then the possibility of measuring the radial velocity variation on the primary will be decreased. The option of direct imaging might also become unavailable as these objects are very likely too dim to carry out this technique. Such biases however are unlikely to affect the mass ratio peak at ~ 1, as the majority of the late spectroscopic and imaging surveys are capable of detecting very low mass binary systems with $q \gtrsim 0.5$. Furthermore, over half of the confirmed very low mass binaries have *q* > 0.9 which is a drop-off that is visible at the highest mass ratios. This bias could instead and more likely lead to underestimating the number of systems with low mass ratio.

1.4.1.4 Binary mass function

Mass as mentioned in the previous section is a very important parameter in determining the evolution of the stellar objects, and the binary mass function helps constraining the components mass in binary systems. The following two relations are used to work out the mass of the secondary object in a binary system:

$$f_1(\mathrm{M}_2) = \frac{\mathrm{M}_2^3\, sin^3\, i}{(\mathrm{M}_1 + \mathrm{M}_2)^2} = \frac{P(v_1 \sin i)^3}{2\pi G}, \quad (1.1)$$

and

$$f_2(\mathrm{M}_1) = \frac{\mathrm{M}_1^3\, sin^3\, i}{(\mathrm{M}_1 + \mathrm{M}_2)^2} = \frac{P(v_2 \sin i)^3}{2\pi G}. \quad (1.2)$$

For f_1 and f_2 being the mass functions for star 1 and star 2. These two relations are derived equating the centripetal force and the gravitational force for both of the components. Note that this is done under the assumption of a circular orbit, also with the aid of Newtonian relations. The measurable quantities are P, which is the orbital period (with the gravitational constant G), $(v_1\ Sin\ i)$ and $(v_2\ Sin\ i)$ which are the projected radial velocity amplitudes of the two components (where i is the orbital inclination of the binary). $\mathrm{M}_1$and M_2 are the quantities that attract the most interest in this equation and they are locate in the middle expression beside $Sin\ i$.

With the two masses directly related to observable quantities by the mass function, the radial velocity amplitudes of both components can be measured from the double-lined spectroscopic binary spectrum. Both $\mathrm{M}_1^3\ sin^3\ i$ and $\mathrm{M}_2^3\ sin^3\ i$ then can be deduced using these relations. However, the inclination is not a quantity that can be obtained easily for the majority of systems, but is necessary if one wants to determine the masses of both components. Thankfully it is more feasible for certain types of binary systems, such as visual binaries and eclipsing binaries, where $i \simeq 90^{\circ}$. Note that the mass function can directly constrain the mass of the secondary if the mass of one of the objects is significantly smaller than the other (i.e. $\mathrm{M}_1 \ll \mathrm{M}_2$). Equation 1.1 in this case simplifies to $f_1(\mathrm{M}_2) \simeq \mathrm{M}_2\ sin^3\ i$. This method is indeed one of the most robust ways to work out the masses of stellar objects as well as black holes. Further, the radii of both stars can be obtained from eclipsing binaries, and in fact these systems are the most common sources for which accurate radii and masses of stellar objects are obtained from. Moreover, if these binaries happen to have known distances too then their luminosities can also be obtained.

1.4.1.5 Binary fraction/multiplicity

The binary fraction/multiplicity is one of the fundamental properties of binaries, offering clues to understand the formation mechanism. It provides extra constraints for testing the existing formation models. Unfortunately, the presence of unresolved binary/multiple systems induces an extra complication in obtaining, in particular for the sub-stellar population, a precise luminosity function. Furthermore, observing faint and close binaries has proven to be a challenge, leading to a poorly constrained binary fraction for BDs and LMSs. Nonetheless, researchers still succeeded in coming up with various methods to work out this vital observable. A brief summary of the present knowledge of the sub-stellar binary fraction is in the following paragraphs.

The percentage of solar-type stars in the main-sequence that have one or more companions is approximately 70% (Abt 1983; Duquennoy & Mayor 1991). Based on other surveys (that however are less complete) other spectral classes seem to have a similar percentage (Abt 1983). However, the binary fraction for M dwarfs, specifically for the ones that are in close binaries, seems to be lower compared to main-sequence binaries (Marcy & Benitz 1989). In addition, for spectroscopic binaries, their frequency is comparable to that of Population I stars (very old stars). This was deduced via a survey of thick-disk and halo stars (Torres 1991). Young binary stars (i.e. younger than 10^5 yrs) are spotted among pre-main-sequence stellar objects, indicating that most binaries are formed during the collapse of the proto-star, or in the stellar formation period. For pre-main-sequence stars,

although the studies of them are limited (Mathieu, Walter, & Myers 1989; Simon et al. 1991), the binary frequency is not showing a significant difference from stars on the main-sequence.

In order to gain additional knowledge regarding the formation environment of LMSs, as well as the history of evolution of their associated planets and disks, and frequency, it is essential to characterise the frequency of binary and multiple stars among M dwarfs. One of the multiplicity studies regarding M dwarf binaries was conducted by Ward-Duong et al. in 2014. The sample of multiple systems that was targeted by the group, to compare with the multiplicity of more massive stellar objects, have a restricted separation limit within the range 30-10,000 AU. Their result is shown in Figure 1.5 (left panel) where from top to bottom are the binary fraction for field A-type stars (represented by the blue solid circle, De Rosa et al. 2014), the yellow solid circle indicates solar-type stars (Raghavan et al. 2010) and the M dwarfs targeted in that study are represented as a red solid circle. In addition, the up side down solid pink triangle in this figure represents the upper limit on the binary fraction for BD primaries (Allen et al., 2007). The figure shows a pattern of decreasing multiplicity as a function of decreasing primary mass, meaning there are more binaries that are A-type (more massive in this case) than the rest of the other type of stars/BDs (less massive in this case). In the right panel of Figure 1.5, the separation distribution for the M dwarfs in the survey of Ward-Duong et al. (2014), inside the restricted range of separations mentioned above, is fit with both limiting cases of the true distribution, i.e. a restricted log-normal (solid line) and a free (dashed line) fit. The distribution was also corrected for incompleteness. The figure shows a high frequency at smaller separations, meaning the separation between M dwarfs are smaller than the other more massive primaries (Ward-Duong et al. 2014).

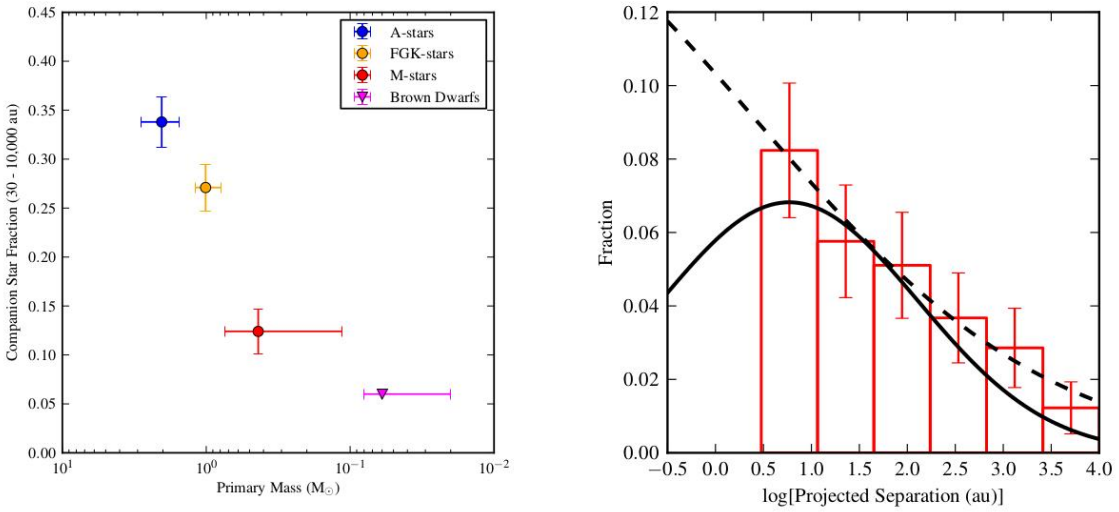

Figure 1.5: (left) The binary fraction measured within 30-10,000 AU (the restricted separation range). (right) The binary separation distribution of the M dwarfs from the survey of Ward-Duong et al. (2014) within the mentioned restricted separation range of 30-10,000 AU (Figure 2 from Ward-Duong et al. 2014).

Other multiplicity studies have been conducted via the combination of high resolution spectroscopy surveys (e.g. Basri & Reiners 2006; Joergens 2006, 2008), with peak sensitivity to tightly bound systems, and high resolution imaging (e.g. Ahmic et al. 2007; Delorme et al. 2012b) which have a higher sensitivity at the typical distances of observed BDs ($\gtrsim$ 2-3 AU). Although biased towards typical BD separations, the binary fraction that was suggested by the magnitude-limited high-resolution surveys is 7-15% (9^{+11}_{-4}%, Burgasser et al. 2003c; $7.6^{+5.9}_{-1.7}$%, Bouy et al. 2003; 13-15%, Martín et al. 2000).

On the other hand, using high-resolution spectroscopy for a sample of late-M dwarfs, an estimation of $6^{+7}_{-2}\%$ was made by Reid et al. (2002b). Then from a sample of 25 late-M and early L dwarfs, Guenther & Wuchterl (2003) have estimated the binary fraction to be $12^{+10}_{-4}\%$. The latest estimation was derived by Joergens (2008) by monitoring the radial velocity of LMSs and BDs in Chamaeleon I. At separations < 3 AU is $10^{+18}_{-8}\%$ and $7^{+5}_{-3}\%$ at separations ≤ 0.3 AU. Joergens (2008) claims that where the separations are < 1 AU then there will be a decline in the binary fraction. This claim is supported by the estimation made by Maxted et al. (2008) where at separations < 0.28 AU, the binary fraction in σ and λ Orionis is estimated to be < 7.5%. The previous results are in disagreement with Kurosawa et al. (2006), who found that at separations < 0.1 AU, the binary fraction in Upper Scorpius is estimated to be $24^{+16}_{-13}\%$.

In addition, Maxted & Jeffries (2005) derived a much higher ratio of tight binaries, after taking into account every likely source of biases and incompleteness in the surveys that were available at the time. They concluded that at separation < 2.6 AU, the binary fraction for very LMSs and BDs is 17 – 30 %. Assuming at separation > 2.6 AU the binary fraction is 15 %, then the total binary fraction would be 32 – 45%. This incidentally supports the binary fraction in the Praesepe and Pleiades clusters of $50^{+11}_{-10}\%$ that were derived by Pinfield et al. (2003).

Wide very low mass binaries seem to be rare in contrast with tightly bound very low mass binaries. There appear to be a decline in binary fraction with separation, from an upper limit of 8% in α Perseus at separation > 11 AU (Martín et al., 2003) to another upper limit of 5% in IC 348 at separation > 15 AU (Luhman et al. 2005), down to an upper limit of 2% in Trapezium at separation >150 AU (Lucas et al. 2005). Note that it is the high resolution imaging that could bias these results (causing some of the very wide systems to be excluded) due to a typical field of view of 10 – 20 arcseconds (i.e. systems at 30 pc with separation $\gtrsim$ 150 AU or systems in young nearby clusters with an even larger separation $\gtrsim$ 200 – 1000 AU).

1.4.2 Formation

All of the binary properties that have been discussed above (from observational data and detailed numerical simulations), play an extremely important role in assisting to answer the long standing question: what is/are the dominant formation mechanism/s for stars, BDs and planetary objects? Extremely young binary systems have been identified (Wotten 1989; Sasseloy & Rucinski 1990) yet there have not been any direct observation during the formation of a binary system so far. Up-to-date observational studies show that it is likely for most binaries/multiple systems to be formed during the proto-stellar collapse (i.e. the very early stage of formation of a stellar object, which can be divided into two phases; first is the isothermal phase, when the object is optically thin; then the adiabatic phase, when it is optically thick). Though various ideas have been suggested to try to explain the origin of binary systems, however, it is fundamental to be able to explain the observed properties of multiple systems in order to determine their dominant formation mechanism.

Although the fully explained physics was missing, Laplace in 1796 was the first person who proposed a formation mechanism for binary systems (see Tassoul 1978). His theory was that separate stellar nuclei form during star formation and somehow come into orbiting each other later. It could be assumed though that it is via fragmentation that the separate nuclei form (Bodenheimer 1992). Then in 1876, Stoney came up with the idea of capture (see Aitken 1935). This might happen when two independently formed unbound stars are slowed down by losing some of their initial angular momentum (i.e. via a dissipative process), and then end up sharing a common orbit (e.g. WD0837+185AB, Casewell et al. 2012). Another possible formation scenario for binary systems that was put forward by Kelvin and Tait in 1883 (see Tassoul 1978) and has the full support of Jeans

(1929) is fission. This mechanism might occur while the hydrostatic equilibrium applies, when an object undergoing a rapid rotation might become dynamically unstable and breaks up into fragments.

In 1953, Hoyle suggested an idea that is based on the principle of increasing density of the isothermal collapsing cloud, extending the originally large scale dependent dynamical instability, to continuously being unstable even when the cloud is reduced in size. This increases the chances for the cloud to fragment as the time frame of given ideal conditions increases. What allows the spreading out of individual fragments after they form, hence stopping the overall collapse of the cloud, as it is not just one large cloud anymore but fragments (though the fragments will continue to collapse separately) is rotation, which is an additional fundamental cause discovered in later works. In other words, during the hydro-dynamical collapse phase, the process of a rotating proto-star being broken up into fragments is known as fragmentation.

Hierarchical fragmentation can be either triggered by rotation (Bodenheimer 1978) or by cloud-cloud collisions (Pringle 1989). However, the results of Lattanzio & Henriksen (1988) numerical simulations of isothermal cloud-cloud collisions show no binaries formed in their parameter range. In addition, close binaries can be the consequence of wide binaries evolution (Pringle 1989). Wide binaries in general are in highly elliptical orbits, and when the binary systems are young, they are likely to have a disc around them. When these discs undergo hydrodynamic interaction at the periastron, the system could lose angular momentum via the friction between the interacting discs, then the original wide orbit could get closer with each disk interaction. When the discs eventually disappear, the system might have lost enough original separation to become a close binary. “Normal” fragmentation on the other hand is to allow the clouds to evolve further (i.e. first undergo gravitational collapse after dense cores have been developed) before the spontaneous fragmentation takes place.

Under ideal conditions, the disc that forms around young stars can become gravitationally unstable, hence lead to possible fragmentation, according to Adams, Ruden, & Shu (1989). A brief discussion of the four types of formation scenarios (fragmentation, disk fragmentation, fission and capture) that are thought to form binary/multiple systems is in the following sub-sections.

1.4.2.1 Fragmentation

During the isothermal phase, the collapse of rotating proto-stars is modelled by theorists, and the outcome suggests a very high likelihood of these proto-stars to fragment into multiple systems due to instability. Systems produced via this process are likely to end up with periods that exceed a few hundred years. Hence this scenario is challenged by the existence of close binaries, because it is known to be very unlikely for the fragmentation to take place while the gas is experiencing high pressure (optically thick and high density), which is the case in the later phase of star formation (when the original cloud has become a lot smaller). In the early stage of star formation the initial cloud can mainly fragment to form wide binaries as the density of the cloud is low and still large in size. Though, it is not impossible for a few of the multiple systems formed by fragmentation to be in relatively shorter periods either. According to Boss (1986), systems with orbital separations to approximately 1 AU can be formed by fragmentation, if they form in the central regions of the clasping cloud while in the adiabatic phase.

Beside this formation mechanism, there are also other formation theories that cannot explain close binaries such as tidal capture, fission of rapidly rotating stars and three-body capture. Other formation scenarios including hierarchical fragmentation, orbital interactions and disk-induced captures in fragmented multiple systems, orbital decay of long-period systems and gravitational

instabilities in disks are under investigation at this time. On the contrary, if the collapsing cloud has low angular momentum, and that low angular momentum is removed after disk formation, or the escape from multiple systems, it could be one of the routes for single stars formation.

One of the more up-to-date numerical calculations regarding hierarchical fragmentation was done by Boss (1991b). In general, the theory of hierarchical fragmentation is that a ring structure would form at a point when the rotational effects come to be significant during the collapse of the formation cloud. Then the fragmentation begins with having the ring first fragment into two parts, then a bit further on the time line, each fragment again splits into two. Though, to be consider a true hierarchical fragmentation, the first fragments of the ring will have to undergo the exact same path as the original collapse cloud (collapsing to the point that rotational effects become essential so that a ring structure is formed), e.g. similar to cellular splitting activity. Moreover, the sub-fragmentation can only occur when each fragment reaches the angular momentum of the original cloud. This requires a further substantial collapse in order for them to regain the 90 to 95% of angular momentum lost after the first fragmentation takes place. This fundamental information regarding the collapse however was not included in the calculations of Boss. Since the resulting sub-fragments do not appear to be sharing an orbit, and also having a sub-orbit which is too small to be view on the numerical grid used, this calculation does not represent true hierarchical fragmentation.

1.4.2.2 Disk fragmentation

A disk like structure will form if a proto-star with a relatively slow initial angular momentum collapses through the adiabatic phase without fragmenting. Gravitational instabilities can cause possible fragmentation in Keplerian disks in equilibrium around a central star (Adams, Ruden, & Shu 1989; Shu et al. 1990). Though the conditions have not yet been recognised, but the formation of a binary system could be possible as a consequence of such instability.

1.4.2.3 Fission

In general, a uniform-density star can gain angular momentum either when it is contracting during the proto-stellar collapse (early phase of star formation) or contracting during the disk accretion (later phase of star formation). The growth rate of the rotational energy surpasses the growth rate of the gravitational energy, and when the rotational energy eventually exceeds the gravitational energy, the star then becomes unstable and breaks up into smaller fragments. Fission yields mostly close binaries due to the limited amount of spin that a star can carry.

However, Tassoul (1978) have pointed out a few major issues that this formation scenario could encounter, such as the slow rotation observed in T Tauri stars (TTS, variable pre-main sequence stars). Dynamical instability therefore is unlikely to take place due to the insufficient angular momentum. Hence fission seems to be favourable only during core accretion. Another problematic issue to this formation theory is that the binary ratio of the resulting systems is not ~ 1:10, which is expected according to observations. The star may also never reach the point where it will become unstable (required initial condition), and this is the third major problem with this formation mechanism. For proto-stellar objects to form very near-by binaries, their angular momentum has to be very small, which then results in the majority of their own mass to collapse onto the central core rather than onto the surrounding disk. According to Ruzmaikina (1981 a, b), the core may not be prone to become unstable (when the rotational energy becomes larger than the gravitational energy) as the effects of convection or magnetism are likely to transport substantial amount of angular momentum within the core out into the disk and lead to the formation of a single star. However, even if the proto-stars manage to reach the point where the rotational energy becomes

greater than the gravitational energy, according to various independent 3-dimensional numerical hydrodynamical calculations of Durisen et al. (1986), the angular momentum can be transferred out from the central core by spiral waves, preventing the instability from happening. For more information see Bodenheimer (1992).

1.4.2.4 Capture

The last formation mechanism is capture, i.e. when two stars that formed independently are captured into an orbit. It may occur under one of the following three situations. The first one is when the excess of energy is removed by the presence of a third body, i.e. when three individual stars are close by initially, then due to dynamical interactions between them one of the body is 'ejected' removing some of the excess energy, and the two remaining objects then form a binary. The second situation is when two single stellar objects pass by each other very closely by chance, and friction is caused by the tidal dissipation between them, slowing them down sufficiently so that dynamical interactions can take place and form a system. The last situation is when, under the presence of a dissipative medium (i.e. residual gas in a young cluster), as the young stars are still close to each other before being separated by their increasing radial velocity, the presence of residual gas could impose friction between them and they could randomly pair up as an outcome.

The first two situations are not supported by observations, as the slow capture rates expected in young dense clusters or in the galactic disk are not able to explain the observed binary frequency (e.g. Hills 1976; Boss 1988; Hills & Day 1976). On the other hand, the third situation is more favourable where the young stellar objects are in the presence of the residual gas that is around them in the form of circumstellar disks. The capture rate that is induced by disks in high stellar-density environments (i.e. Orion Trapezium cluster) is 0.4 captures per star per 10^6 yr, which is considered to be significant (Larson 1990). Though another factor that could affect this process was pointed out by Clarke & Pringle (1991a). Depending on the velocity of the encounter, disks around stars may be removed by high-velocity encounters, whereas capture is much more likely to occur during low-velocity encounters. The capture rate according to Clarke & Pringle (1991a) is 0.04 captures per star per 10^6 yr, an order of magnitude lower than Larson's (1990). The capture rate is however $\approx 0.05 - 0.1$ captures per star per 10^6 yr according to the results of numerical calculations by Heller (1991), which sits in between of Larson's (1990) and Clarke & Pringle (1991a) results.

The separation between the components depends on the type of capture. Systems produce by the three-body capture are often far apart, and close binaries are often produced by the two-body tidal capture, while the separations between the paired up stellar objects produced by the disk capture are comparable to the outer radius of the disk. The various sizes of orbits produced by these three types of capture cannot explain the smooth period distribution observed. Though, some other observations can be explained by the predictions of the capture theory, such as a wide range of mass ratios (no relation in mass between the two components) and eccentricities. In addition, the components are non-coeval (differences in age observed so far are up to 10^6 yr) and the spin of the angular momentum of one of the component can be not aligned with the orbit, as observed in some systems.

Normally the probability for this mechanism to take place is relatively low, but in different circumstances capture can have a slightly larger effect (i.e. fragmentation of a collapsed molecular cloud core, see Miyama, Hayashi & Narita 1984; Monaghan & Lattanzio 1991). For example in a very high stellar-density environment (i.e. more so than the Orion Trapezium cluster) the typical separation between fragments is small (i.e. ~ 0.01 parsec). Gravitational interactions therefore take place between the fragments, and single stars and binaries may be produced by the three-body

capture process, also by the disk-induced and tidal capture (the latter in close orbits). This type of systems was studied with the aid of N-body simulations of multiple systems (see e.g. Anosova 1989). Furthermore, for the three-body 'systems' with disk dissipation (co-orbiting initially and highly unstable), numerical studies were made by Clark & Pringle (1991b). Their results show high sensitivity with changes to the initial conditions, and also a possible wide range of eccentricities and orbital parameters.

1.4.3 BDs in multiple systems

The first L and T dwarfs, GD 165 and GL 229B respectively, were both discovered accompanying a more massive primary (i.e. WD-L dwarf and M dwarf-T dwarfs). In order to increase the number of identified nearby bright stellar objects that couple to brown dwarfs, various methods have been used and a lot of interesting new multiple systems hence have been discovered.

With the facilities of the Hubble Space Telescope (HST) high-resolution red and IR imaging being available, one of the methods is to look for low-mass companions to M dwarfs, either in open clusters (e.g. MartÍn et al. 2000; Patience et al. 2002) or in the field (Reid & Gizis 1997). Alternatively, these types of high-mass-low-mass systems can also be identified by applying the X-matching method (in this case by X-matching a good selection of UCDs, e.g. DA with catalogues of stellar objects e.g. HMC or GJC to establish binarity via common proper motion) which is a standard procedure nowadays to search for multiple systems (Luyten, 1979). Note that van Biesbroeck in 1961 was the first person to apply this technique in an attempt to look for faint companions to 650 nearby stellar objects. The search for UCDs as companions to nearby stars hence becomes more conceivable now with the availability of NIR all sky surveys.

The mass of BDs is fundamental in obtaining insights on the properties of these objects. However, the sub-stellar nature of these UCDs prevents the use of the luminosity-mass relation to determine their mass. The age of these ultra-cool objects is also impossible to determine if they are isolated. This is where benchmark systems become extremely useful, especially in the study of the nature, formation and evolution of UCDs. This sort of systems in general consist of main-sequence star/s and UCD/s, and note that the preferable benchmark systems are those with wide separation (i.e. > 100 AU). This is because if the faint UCD is too close to the parent star then the glare of the primary will make it impossible to observe the low-mass object. In addition, the nature and the properties of the BD could also be altered by the exchange in mass within the system (e.g. when the star evolves and becomes a red giant) if the components are too close. These cannot be considered benchmark systems anymore.

Young benchmark UCDs (≤ 1 Gyr) can be found as members of moving groups and clusters (e.g. Casewell et al. 2007, Lodieu et al. 2011, Gagne' et al. 2014, Malo et al. 2014). By sharing kinematic properties, the UCDs have a known metallicity and a decent constrained age as part of the cluster. Note that the formation and properties of these very young sub-stellar objects can be derived and studied within those nursery environments, such as the Orion nebula cluster. In addition, given that these benchmark systems are very young (~ 1Myr), hence they are much brighter, and so they can be observed out to much greater distance than that of field UCDs.

Unfortunately, for field UCDs, the age, metallicity, and other physical properties are a challenge to obtain, one of the major complications being the mass-age degeneracy (i.e. the fact that they significantly fade and cool over time). UCDs as member of binary systems however provide the best source of benchmark companions (e.g. Pinfield et al. 2006). This is because the primary-secondary relation apply in this case and as the stellar companions are well characterised, and given they were formed from the same molecular cloud, it is quite safe to assume both objects have identical age

and composition (i.e. metallicity). Note that several methods can be used to calculate the age of the main-sequence primary. Such methods include comparison to theoretical models with their location on the HR diagram, age-metallicity relations, space or rotational velocity (i.e. kinematical) age, Lithium test and coronal or chromospheric activity (CaIIHK, Hα, X-ray). Note that for eclipsing benchmark systems, their mass (from Kepler's law) and radius (from the light curve) can be calculated from the dynamical interaction of the system. However, depending on the type of primary stellar object, a precise measurement of the age could be a challenge (e.g. variable stars).

Note that the later phases of stellar evolution show age calibrators that are more reliable than the main-sequence phase, where the uncertainty on the age can be large. For example the subgiant stage is relatively well constrained, and also very short in comparison to the lifetime on the main-sequence. Furthermore, there are also benchmark systems that consist of a UCD companion to a white dwarf (WD, e.g. Rodriguez et al. 2011, Casewell et al. 2012). Such systems include DA WDs-L dwarf (e.g. Zuckerman & Becklin 1992; Kirkpatrick et al. 1999; Steele et al. 2009), DA WD-mid-T dwarf (Day-Jones et al. 2011, Casewell et al. 2012) and DQ WD-possible Y dwarf (Burleigh et al. 2009; Luhman et al. 2011). The cooling age of the WD can be measured with precision as the WD stage is well understood. With hydrogen in their atmosphere as well as being very hot (i.e. > 12, 000 K), the hydrogen lines are strong and can be easily observed and measured in WD spectra. Then by fitting the spectrum with an appropriate atmospheric model, a decent estimation of the T_{eff} and the mass of a WD can be obtained. Appling the relation between the WD and the progenitor, the mass of the progenitor can then be obtained (Catalan et al. 2008). Using the main-sequence mass-T_{eff} relation, the T_{eff} of the progenitor can be derived. Then from evolution models of the main-sequence, the initial T_{eff} of the WD is obtained, from this the cooling age (by knowing how much the WD has cooled down, calculating the time it takes to reach the current T_{eff}) of the WD can be derived. Using evolution models of the main-sequence again to get the total time that took the progenitor from being born to first becoming a WD, combining it with the cooling age that was previously acquired, one can determine the age of the WD.

The X-matching technique was used by e.g. Gizis et al. (2001), Kirkpatrick et al. (2001) and Wilson et al. (2001) in the early days to currently by e.g. Burningham et al. (2009), Faherty et al. (2010), Day-Jones et al. (2011), Pinfield et al. (2012) and Gomes et al. (2013). Various discoveries and interesting results have been produced by this method. Note that the latest works have employed more modern surveys (e.g. UKIDSS and WISE) along with the less contemporary 2MASS. In addition, these wide benchmark systems also provide extra constraints to test important models and theories (e.g. evolutionary models, Mohanty et al. 2004a,b; Dupuy et al. 2009, and atmospheric models, Leggett et al. 2008; Burningham et al. 2009; Pinfield et al. 2012).

1.4.3.1 Population properties

It is relatively common for wide main-sequence binaries to have separation >1000 AU. From a sample consisting of three L dwarf companions to main-sequence stars, an L dwarf companion fraction of 1.5% have been deduced by Gizis et al. (2001). A total UCDs companion fraction of 18±14% was also then calculated. Note that this is under the assumption of α=1, which substituted into the companion mass function leads to the fraction of UCDs detected as L dwarfs being 8% (Gizis et al. 2001). Using a larger sample consisting of 14 common proper motion companions to stars (out to a limiting magnitude of J=16.1) from the Hipparcos catalogue, Pinfield et al. (2006) deduced a larger L dwarf companion fraction of $2.7^{+0.7}_{-0.5}$% and a larger UCD companion fraction of 34^{+9}_{-6}% (under the same assumptions as Gizis et al. 2001). This result implies that a sufficient amount of wide companion UCDs to main-sequence stellar objects are available for studying.

A mass-age plot of benchmark UCDs is shown in Figure 1.6 (taken from Figure 6.3 of Day-Jones's PhD Thesis, 2010). The distance-magnitude limit can clearly be observed, corresponding coarsely to a detection limit of J~19. This is represented by the black dotted line, corresponding to a distance limit of 50pc, reflecting the sensitivity of the surveys used to discover these UCDs. Being extremely faint, the expectation of detecting old, very low-mass UCDs using these surveys is very low. More, due to the fact that for young UCDs there are more age indicators (e.g. activity, rotation, and Lithium detection) hence their age can be more easily constrained. So in comparison there are many more young benchmark UCDs than old benchmark UCDs. Note that most of the benchmarks in the younger region have known metallicity as they are members of moving groups or clusters. In addition, the figure also show that the numbers of benchmarks UCDs decreases beyond the age of 2 Gyr.

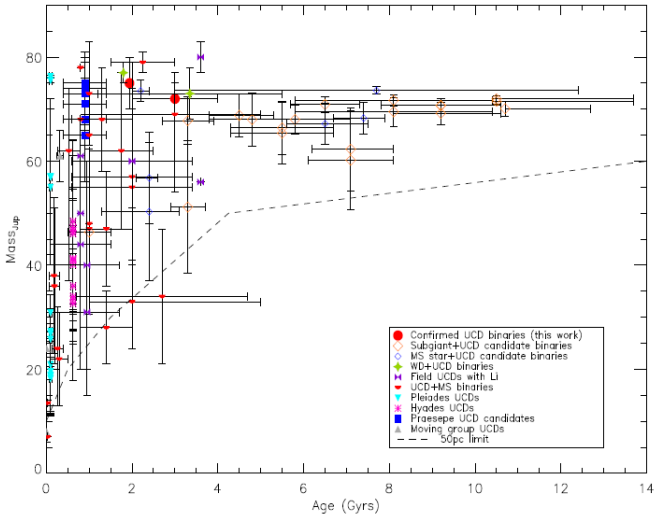

Figure 1.6: Taken from Figure 6.3 of Day-Jones's PhD Thesis (2010). A mass-age plot showing the distributions of the benchmark systems from the literature.

The importance on benchmark UCDs is shown further in Figure 1.7, taken from Figure 10 in Burningham et al. (2013). The two plots show a comparison between the observed colours of a number of benchmarks and the model grid from Saumon et al. (2012) in the top part of the plot and the model grid from Morley et al. (2012) in the bottom part of the plot. Each benchmark is linked to a box indicating the colour predicted by the models. It can be seen that the model predictions are wrong by almost 0.5 magnitudes in many cases, showing that the models need improvements.

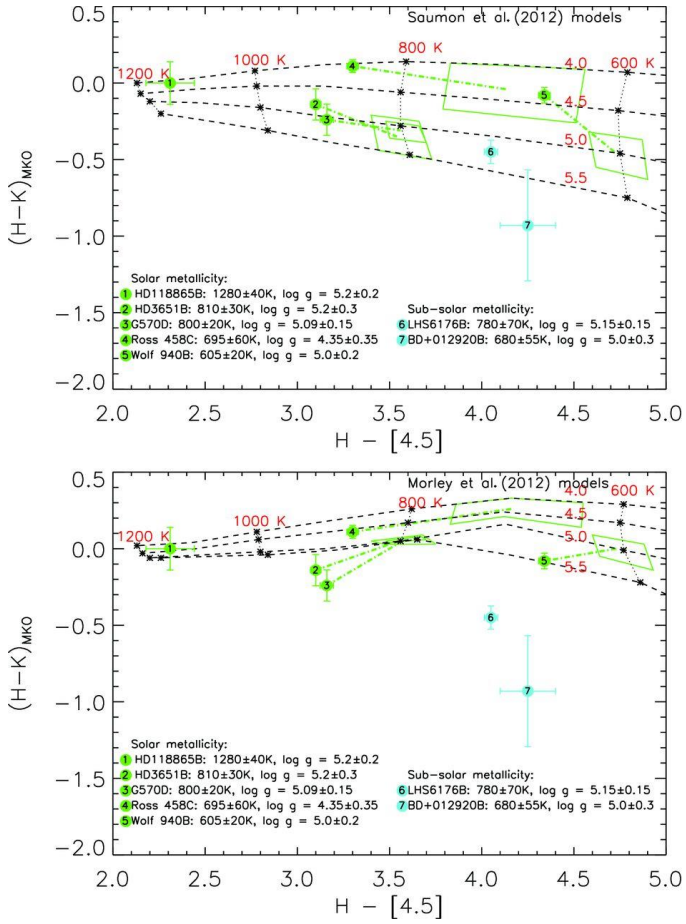

Figure 1.7: Taken from Figure 10 from Burningham et al. (2013). A colour-colour plot of the benchmark systems from the literature. Model colour tracks for Saumon et al. (2012) and Morley et al. (2012) are shown for comparison. Each benchmark is link to a box indicating the colour predicted by the model.

1.4.4 Dynamical interaction of multiple systems

In general, celestial objects interact with each other gravitationally (for basic interaction physics, see e.g. Fregeau et al. 2004; Malmberg et al. 2007 for interactions in clusters, and for interactions in disks see e.g. Moeckel & Veras 2012). Discussing in details the properties and evolution of the numerous types of interacting binary systems is beyond the scope of this thesis. In the following sections I will therefore focus on the disintegrating systems, since these are the target of my work.

1.4.4.1 Disintegrating systems

In a particular case, when a binary system is interacting with a close by object, or with another binary/multiple system, over time the binding energy within the components of the binary are gradually reduced, causing the system to eventually become unbound. Note that binaries that have a large cross-section (i.e. wide binaries) are more likely to interact with other stellar or sub-stellar objects. Normally, such interactions are relatively weak, nevertheless, there are some more severe interactions between binaries and single stars/binaries that can lead to a relatively more violent break-up of the systems. Disintegrating systems are thought to be common (Li et al. 2009), but the average time for disintegration is short, approximately 1 Myr (Szebehely 1972) therefore disintegrating systems are very difficult to identify.

To search for disintegrating multiple systems, I will first have to look for binary/multiple systems whose components have a wide separation between each other. This is because the widely separated systems will naturally have a greater possibility of disintegrating in comparison to much tighter systems. In principle, a system with weaker bonds within the components is easier to be disrupted by chance dynamical interactions (with other by pass stellar or sub-stellar objects/systems) than systems with stronger bonds. In theory, this could be the cause of some of the disintegrating multiple systems seen in the HMC (Li et al. 2009).

I will be looking into those binary/higher order systems and use their proper motion to see if they are disintegrating systems. Then I will look for their ejected components. Although I will not be using the Marchal's test (Li et al. 2009) for this purpose, but it will make a good comparison to my method, and so I briefly describe it in the following section.

1.4.4.2 The Marchal's test

The field of disintegrating triple/multiple systems has not been widely explored, however, Marchal in 1990 has developed an analytical test to look for escaped objects from a general N-body system. Later, Li et al. in 2009 attempted to adapt the Marchal's test to real triple stars.

Objects or structures that are most frequently observed are believed to either have a long life span or to be reasonably stable. In particular, real triple stars seem to be found at a higher rate in hierarchical configuration rather than in random structures. This suggests that systems not in hierarchical configuration are likely to be unstable. Though, systems that are in hierarchical configuration are not necessarily stable either. When applying the Marchal's test (1990), it is fundamental to identify a substantial amount of real disintegrating systems. Note that there are a few things one need to bear in mind regarding triple systems. First, according to extensive simulations on systems with hierarchical configuration, $\sim$95% have had an ejection in their life-time (e.g. Anosova 1990). Second, some triple systems can form via binary-binary encounters, where one of the components of the original binary systems gets ejected during the encounter of the two systems (Saslaw et al. 1974). This is deduced by the dynamical evolution of stellar clusters (e.g. Aarseth 2003b, 2004) and numerical experiments on binary-binary encounters (Mikkola 1983). The last point is that, since the hierarchical configuration is in general a more stable structure for triple systems, newly formed triple systems (e.g. via binary-binary encounter) re-arrange into hierarchical configuration shortly after formation (Li et al. 2009). Overall this information implies that numerous triple systems that are in hierarchical configuration are likely to reach a disintegration phase shortly or are currently disintegrating. Note that there are types of triple system this method cannot be applied to. For some types of triple systems (e.g. "binary-third body system"), their period can be too long, exceeding the time duration spanned by available observations, leading to unreliable orbital solutions (Lattanzi et al. 2004).

This test only requires a one-dimensional projected motion state of the system at any given instant. The Marchal's test is a relatively well developed tool for the purpose of identifying real, disintegrating small stellar systems, for which the full motion state is usually unavailable. To test out visual triple stars, Li et al. (2009) have designed an algorithm for practicality to make good use of the two-dimensional kinematic data. They then applied this algorithm to 24 Hipparcos triple systems with their disintegration probability and the estimated mass of their components already obtained. The Monte Carlo method was used to deal with the errors from observations. A reliable set of probabilities for a real triple star disintegrating system was eventually calculated. Ten out of 24 of their triple systems were believed will have an unavoidable escape event, i.e. those systems will disintegrate eventually.

Ultimately, the main difference between my method and Li et al.'s (2009) method is that they use the dynamics of the system, i.e. they need to know the mass of the objects in the system, their orbit and their velocity, and those things are hard to measure. On the other hand, my method relies solely on proper motion, distance and separation, which are easier quantities to measure and obtain.

Note that such interactions might also release low-mass objects previously bound to one of the components of the system. Such low-mass objects might include LMSs, BDs, or ESPs.

1.5 Motivation

The motivation to work on this topic is mainly because of the interest in studying the orbital population of giant planets, BDs and very low-mass stars. However, it is proven to be difficult as these low-mass objects at visible wavelengths are relatively faint compared to their parent stars. The difficulty to detect such faint light sources, plus the glare of their primary stars, tend to "wash out" these objects, making studying them a challenge. Blocking the light from the parent star to reduce the glare and leave the bound population detectable is a major technical obstacle. Being able to identify systems where the orbital population has been ejected dynamically would avoid such problem.

The aim of this project is to look for evidence of disintegrating multiple systems with cool nearby components in order to collect a set of possible candidate systems for further studies. Since there is a number of UCDs in DA that might be examples, I started my work using the DA, HMC and GJC where these candidate systems can be found. I will use the measured proper motions from DA, HMC and GJC to test if those multiple systems are disintegrating systems, and then look for their ejected components.

Chapter 2

2. Analysis methods and candidate samples

In this section I describe the analysis tools I used, and the astronomical catalogues and archive/database facilities I searched to implement my project. Useful background and context is presented, and relevant capabilities are summarised. I describe my approach for determining distances, and consider how the sensitivity and content of each catalogue will bias my selection of candidate disintegrating multiples (in terms of distance range and uncertainty, as well as spectral type constituents).

I then explain my X-matching approach, and look at the resulting distribution of associated candidates. Furthermore I explain how I confirm disintegrating multiple candidates from their relative direction of motion. The results of my analysis are then presented in a table.

2.1 Tools and Catalogues

In order to identify ejected populations from disintegrating multiple systems I needed to identify a set of possible disintegrating multiple system candidates. To begin, first I had to collect all the available data from catalogues. The three primary catalogues I have used are Dwarf Archives (hereafter DA), the Hipparcos Main Catalogue (HMC, Perryman et al. 1997; van Leeuwen 2007) and the Gliese–Jahreiß Catalog (GJC, Gliese & Jahreiß 1979; Stauffer et al. 2010). I have decided to use the HMC and GJC all sky surveys for the stars and low-mass stars that could be associated with the cool objects from DA. The background and reasons for these choices are in the following sections.

To access and analyze the data from the above catalogues, I have used a few essential tools. I have listed them below along with a brief description of their uses.

2.1.1 Dwarf Archives

The Dwarf Archives (DA) is a compendium of 1281 spectroscopically confirmed M, L, T, and Y dwarfs from various sources in the literature. In this thesis I used the version updated on the 29-05-2013. It contains some M dwarfs, but mainly includes L and T dwarfs (as well as the small number of new Y dwarfs). These objects are taken from the published literature, and were mainly discovered using a number of major surveys carried out over the last ∼15 years. The largest number of L and T dwarfs in DA was found in the 2MASS (Skrutskie et al.2006), the SDSS (York et al. 2000), the UKIDSS (Lawrence et al. 2007) and the WISE (Wright et al. 2010). This catalogue provides co-ordinates, spectral types, photometry in the *J*, *H* and *K* band (mainly from 2MASS and UKIDSS), parallaxes and proper motions, along with additional information on binarity, variability, and peculiarity.

2.1.2 Hipparcos Main Catalog

Hipparcos stands for HIgh Precision PARallax COllecting Satellite (HMC, Perryman et al. 1997; van Leeuwen 2007) and it was the first space experiment devoted to precision astrometry. It was launched in 1989 and operated until 1993. There are 118218 entries of main-sequence stars from spectral type O to M in the Hipparcos Main Catalog (HMC). It is known to have very reliable parallaxes (trigonometric parallaxes provide direct distance measurements) and proper motions of stars down to a precision of ∼0.001 arcsec, and it is complete out to ∼20pc. It has limiting magnitudes of $V \sim 7.3$ to 7.9 (depending on spectral type) in uncrowded fields. The information provided by HMC that we used mostly in this work are co-ordinates, parallaxes, proper motions, spectral types, and B and V band photometry. Note that the Tycho catalogue also came from the Hipparcos mission, providing lower precision astrometry and photometry for stars down to fainter magnitudes (∼2.5 million stars down to V∼11), but I do not use the Tycho catalogue in my work.

2.1.3 Gliese–Jahreiß Catalog

The Gliese–Jahreiß Catalog (GJC, Gliese & Jahreiß 1979) consists of 3803 entries of main-sequence stars within the completeness limit of 25 pc. In this Thesis I have used the updated version from Stauffer et al. 2010. GJC provides co-ordinates, parallaxes with average precision up to 14%, proper motions, and *B* and *V* band photometry. From spectral type O to M, the spectral type distribution in this catalog is shown in Figure 2.1. With no O type stars at all and with only 4 out of 3803, B type stars are less than 1%. There is an obvious pattern of increase in number as the mass of the main-sequence star decrease. For A type stars the percentage is 4 %, for F type stars is 7 % then for type G, K and M stars is 13%, 20 % and 29% respectively. Note that the remaining 27% of the objects are not main-sequence stars. The spectral type distribution of GJC is dictated by the relative numbers in the local volume. There are many more low-mass stars than there are high mass stars due to the rising stellar mass function (Chabrier 2003). Note that GJC is not complete since it only includes objects with parallax measurements, and in any event not all stars within 25pc have been published. For a recent example of newly published parallaxes (not included in GJC) see Winters et al. (2015).

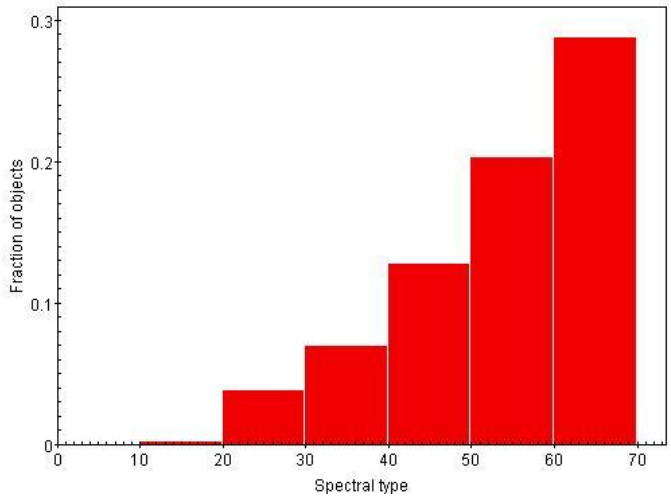

Figure 2.1: From spectral type O to M (0-9 O type, 10-19 B type, 20-29 A type, 30-39 F type, 40-49 G type, 50-59 K type and 60-69 M type), the spectral type distribution of GJC.

2.1.4 The WFCAM Science Archive (WSA) and the Vista Science Archive (VSA)

The Wide Field Camera (WFCAM) Science Archive (WSA, Hambly et al. 2008) and the Vista Science Archive (VSA, Cross et al. 2012) are the web archives for the WFCAM instrument on the UK infrared Telescope (UKIRT) and the VIRCAM instrument on the Visible and Infrared Survey Telescope for Astronomy (VISTA) telescope.

The data of the WSA were collected by WFCAM on UKIRT. WFCAM has a pixel scale of 0.4 arcsec/pixel and can cover the range of wavelengths between 0.83-2.37 μm by using the *Z*, *Y*, *J*, *H*, *K* and H_2 filters. The data were released as part of the UKIDSS (Lawrence et al. 2007), which is a modern NIR sky survey (successor to the 2MASS, see section 2.1.9; Skrutskie et al. 2006). UKIDSS consists of 5 public surveys (all described in Lawrence et al. 2007): Large Area Survey (LAS), Galactic Plane Survey (GPS), Galactic Clusters Survey (GCS), Deep Extragalactic Survey (DXS) and Ultra Deep Survey (UDS). In fact, extending to both high and low Galactic latitudes, UKIDSS had surveyed 7500 square degrees of the northern sky with an effective volume 12 times larger and a depth of three magnitudes deeper than the previous 2MASS.

With limiting magnitudes for the *Y*, *J*, *H* and *K* band reaching 20.5, 20.0, 18.8 and 18.4 respectively, in the Northern hemisphere, the LAS (the largest public survey of UKIDSS) imaged an area of 4000 square degrees at high Galactic latitudes. To obtain the proper motion for the surveyed objects, a second scan of the whole area was necessary and filter *J* was employed to do the job. The *Z* filter at 0.84-0.93 μm and the *Y* filter at 0.97-1.07 μm were used to survey for possible nearby low-mass dwarfs and cool Y dwarfs. UKIDSS also targeted the detection of known objects (i.e. high proper motion cool stars that could be both Population II BDs and cool white dwarfs). Note that the filters of UKIDSS are less sensitive than the SDSS's (York et al. 2000) and so they get better reading without the interference of atmospheric conditions. The combination of photometry data of both SDSS and UKIDSS offers a wide and unobstructed atlas in all directions of the Galactic plane. The area that LAS scanned is a subsection of the SDSS (1907.6 square degrees of SDSS equatorial block, 1907.6 square degrees of SDSS northern block which overlap a bit, and 212.5 square degrees of the southern equatorial stripe, see Stoughton et al. 2002 for more details).

Covering 1800 square degrees, the GPS surveyed half of the Galactic plane with the passbands *J*, *H* and *K*, with limiting magnitudes of 20.0, 19.1 and 19.0 respectively. Note that over the duration of a few years, in order to measure proper motions and identify variability, the depth of the K band was built up in three passes. Furthermore, the narrow H_2 band (2.12 μm) in the survey was used to scan 300 square degrees of the Taurus-Auriga-Perseus (T-A-P) star formation complex.

Using *Z*, *Y*, *J*, *H* and K filters with respective limiting magnitudes of 20.4, 20.3, 19.7, 18.8 and 18.7, GCS surveyed 1400 square degrees of the sky. This survey was programmed to image 10 open star clusters and star formation associations. Due to the need of measuring proper motion, the K band was used to pass over the same survey area a second time. In an attempt to test the universality of the IMF, the GCS was used to measure the sub-stellar mass function all the way down to a mass limit of $25\mathrm{M}_J$.

The DXS scanned a combination of 4 fields at high Galactic latitudes, (XMM-LSS, Lockman Hole, Elais N1 and VIMOS 4) each covering 8.75 square degrees, adding up to a total area of 35 square degrees. Note that out of the 3 filters used in this survey, only *J* and *K* image the whole 35 square degrees whereas *H* only survey 5 square degrees out of the total scan area. The limiting magnitudes of the *J*, *H* and *K* band are 22.5, 22.0 and 21.0 respectively.

The 0.77 square degrees covered by the UDS were actually the same field as the Subaru/XMM--Newton Deep Survey. The UDS used the *J*, *H* and *K* filters down to a depth of 25.0, 24.0 and 23.0.

Note that 2 out of 5 of the public surveys cover only a small area of the sky (35 square degrees to *K*=21 and 0.77 square degrees to *K*=23), but they were designed to enrich our understanding of deep extra-Galactic sources (i.e. galaxy clusters and elliptical galaxies at redshifts 1<z<2, high-redshift dusty starburst galaxies, and the highest-redshift quasars at z=7).

The data of the VSA were collected by the Visible and Infrared Camera (VIRCAM) on VISTA (Emerson et al. 2004). VISTA is a wide field survey telescope with a 4 meter primary mirror. The operations of the public survey began in April 2010. Feeding a 0.34"/pixel camera, the infrared field of view of this telescope is 1.65 degrees in diameter. VISTA is so sensitive that to follow up any selected object, an up-to-date 8 meters class telescope is necessary. The rapid deep infrared imaging surveys use wavelengths mainly from 0.85 to 2.3 μm (passbands of *Z*, *Y*, *J*, *H* and K_s) to have the southern sky covered. Moreover, the *J* and *H* filters aim to be 3 magnitudes deeper than 2MASS, a depth achieved by repeating observations of each field for at least 4 years.

In an attempt to accomplish different scientific goals, each survey was programmed to use a certain set of filters with specific detection limits to observe a particular solid angle of sky. For the first 5 years, there are 6 surveys (VISTA Variables in the Via Lactea (VVV), VISTA Hemisphere Survey (VHS), VISTA Kilo-Degree Infrared Galaxy Survey (VIKING), Ultra VISTA, VISTA Magellanic Cloud Survey (VMC), and VISTA Deep Extragalactic Observations (VIDEO)) that took up the majority of the observing time.

562 square degrees of the central part of our galaxy (galactic bulge and adjacent section of the disk, containing 33 globular and 355 open clusters) are the main target of the VVV survey. The filters used for this purpose are the *Z*, *Y*, *J*, *H* and K_s with limiting magnitudes of 21.9, 21.2, 20.2 18.2 18.1 respectively. The multi-epoch setting of the VVV allows the detection of a vast amount of variable objects. For each patch of the sky covered, more than 100 observations will take place at various times, cautiously interspersed. The survey should produce a catalogue consisting of approximately a billion point sources and about a tenth of them should be variable objects.

By scanning approximately 20 000 square degrees of the sky (excluding the areas already covered by VVV and VIKING in the *J* and K_s near-infrared bands, the whole area of the southern hemisphere), the VHS is the largest of VISTA's surveys. The limiting magnitudes of the filters used in this survey (*Y*, *J*, *H* and K_s) are 21.2, 21.2, 20.6 and 20.0 respectively. The resulting data in comparison to the former Deep Near-Infrared Survey of the southern sky (DENIS, Epchtein et al. 1999) and 2MASS will be 4 magnitudes deeper, or in other words forty times deeper.

Imaging 1500 square degrees (see VLT Survey Telescope of the Kilo-Degree Survey (VST- KIDS) e.g. http://kids.strw.leigenuniv.nl/), with limiting magnitudes of 23.1, 22.3, 22.1, 21.5 and 21.2 respectively, the VIKING survey is geared with the *Z*, *Y*, *J*, *H* and K_s filters. When combined with KIDS, the total of 9-passbands allow the measurement of highly accurate photometric redshifts (since the estimate of the distance of galaxies depends on their colour, especially the ones that are very far away). Compared to the Large Area Survey (LAS) of UKIDSS, the limiting magnitudes of VIKING are deeper by 1.4 magnitudes, and by 2 magnitudes if compared to SDSS.

Ultra VISTA covers only 1.5 square degrees of the southern sky (the Cosmological Evolution Survey (COSMOS) equatorial field) and by observing the same area repeatedly, aims to study the build-up of stellar mass during the peak epoch of star formation activity, star formation that is dust-obscured, and the first galaxies. It is the narrowest and deepest survey of VISTA. To achieve this desire, the *Y*, *J*, *H* and K_s filters, with limit magnitudes of 26.7, 26.6, 26.1 and 25.6 respectively, are used along with one narrow-passband filter with limit magnitude of 26.

The data collected by the VMC are suitable for studying the resolved stellar population, the star formation history of the system, and also to trace its three-dimensional structure. The main goal is to survey the 184 square degrees of the Magellanic System (our nearby neighboring galaxies) i.e. the Large Magellanic Cloud and the Small Magellanic cloud, and also their environment i.e. the Bridge and the Magellanic Stream. VMC uses the *Y*, *J* and K_s filters that have limiting magnitude of 21.9, 21.4, 20.3 respectively.

By using the *Z*, *Y*, *J*, H and K_s filters with limiting magnitudes of 25.7, 24.6, 24.5, 24.0 and 23.5 respectively, VIDEO is a survey that aims to extend the knowledge in extragalactic astrophysics. The program images 3 areas of sky (4.5 square degrees of the XMM-Newton Large-Scale Structure Survey, 3 square degrees of a field of the European Large-Area ISO Survey, and 4.5 square degrees of the Extended Chandra Deep Field South – for more information see Jarvis 2012) that make up the total scanning area of 12 square degrees. In general, VIDEO is an intermediate survey between Ultra-VISTA (very deep but narrow) and VIKING (relatively shallow but wide).

2.1.5 Two Micron All Sky Survey (2MASS)

Two Micron All Sky Survey (2MASS, Skrutskie et al. 2006) operated from 1997 to 2001. Its instruments were two 1.3m telescopes at Mt. Hopkins and CTIO in Chile, each equipped with a 3 channel camera using 256x256 arrays of HgCdTe detectors. It mapped the entire sky in three photometric bands: *J*, *H*, and *K* with limiting magnitudes of 15.8, 15.1, and 14.3 respectively.

2.1.6 Sloan Digital Sky Survey (SDSS)

Sloan digital Sky Survey (SDSS, York et al.2000) has been in service since 2000 to present, using a 2.5 meter telescope at Apache Point Observatory in New Mexico. It has a 120 megapixel camera which images 1.5 square degrees of sky at each pointing. The passbands that are used in SDSS are *u*, *g*, *r*, *i* and *z* to a depth of 22.0, 22.2, 22.2, 21.3, and 20.5 magnitudes respectively. The *z* band is a very good tool for detecting M dwarfs and younger objects, because they are bluer and appear brighter in the z band compared to colder brown dwarfs.

2.1.7 Wide-field Infrared Survey Explorer (WISE)

More recently, the Wide-field Infrared Survey Explorer (WISE, Wright et al. 2010), since its launch on 2009, have mapped 99% of the sky with angular resolutions of 6.”1, 6.”4, 6.”5 and 12.”0 at wavelengths of 3.4, 4.6, 12 and 22 μm. The limiting magnitudes are 15.3, 14.4, 10.1, and 6.7 respectively. It is a 40cm telescope feeding arrays with a total of 4 million pixels. WISE’s W2 band centred at 4.6 μm is a very powerful tool for tracking down cool brown dwarfs, especially Y dwarfs.

2.1.8 SuperCOSMOS Sky Survey (SSS)

The web server of the SuperCOSMOS Sky Survey (SSS) was first set up in Jun 1999 providing an on-line access for the users to extract digitized data up to 15 arc minutes across in three wavebands, i.e. blue, red (two epochs) and near infra-red, for the whole sky. It was the first time that proper motions, colours and variability information were available in digitized format. SSS has a smaller pixel size (10 micron, i.e. 0.7 arcsec) compare to both the old DSS-1 25 micron (i.e. 1.75 arcsec) and the new DSS-II 15 micron (i.e. 1.05 arcsec). Moreover, it allows accessing the images associated with the catalogue simultaneously. These images were obtain from SuperCOSMOS scans of photographic

plates from various different sky surveys conducted with the Palomar Schmidt telescope, the UK Schmidt telescope (UKST), and the ESO Schmidt telescope.

2.1.9 Catalogues selection

Since ejected objects from multiple systems are expected to be very rare, to maximize the chance of finding them, I had to search within a very large set of objects. The reason why I used HMC and GJC in this project is because they contain bright nearby stars that would constitute ideal benchmark systems. They also provide a good range of spectral types from O to M, and distance. I needed accurate parallax distances for at least the stellar components (hence HMC and GJC as the most comprehensive samples currently available). Then I relaxed this requirement for ultra-cool components so that I increased the number of possible associations (thus DA). Overall I have thus managed the distance uncertainties (to avoid loads of false associations), but not limited the UCD numbers too much (to maximise the chance of finding systems).

2.2 Distance measurements

2.2.1 Distances for DA

I started off working with DA; for each UCD, this catalogue provides right ascension (α), declination (δ), J magnitude (Jmag), H magnitude (Hmag), K magnitude (Kmag), parallax (π), proper motion (μ), position angle (θ) and spectral type (spt), both in optical (opt) and infrared (ir) along with their associated uncertainties.

2.2.1.1 Obtaining photometric distance

Many of the objects in DA do not have a measured parallax. To resolve this problem, I first obtained the absolute *J* magnitude (M_J) using the absolute magnitude-spectral type relation from Dupuy & Liu (2012). The polynomial fit for MKO and 2MASS magnitudes are shown in Figure 2.2 (Figure 25 of Dupuy & Liu 2012). I used the MKO and 2MASS photometric systems for my work, and was thus able to make use of the analysis presented by these authors. Figure 2.2 shows NIR absolute magnitude as a function of spectral type (for all ultra-cool field dwarfs with parallaxes, but not including known young or planetary mass object and sub-dwarfs). The polynomial fits to the data are represented by the thick solid lines and the inverted polynomial fits are represented by dashed grey lines. Especially for the *K* and $K_s$band, the spectral types as a function of magnitude are sufficiently monotonic. The objects were plotted in various colours for various ranges of spectral type (brown, red, purple and blue for spectral ranges of M6 - L2, L2.5 - L9, L9.5 - T4 and ≥ T4.5 respectively). The root mean square (rms) of the fit is given at the bottom of each panel and for the inverted polynomial fits the rms values are shown on the right of the plots. I then calculated the distance modulus (DM) using *J* from the catalogue data (*J*-M_J = DM). I could then use it to calculate the photometric distance by rearranging DM = 5logD - 5 to obtain D.

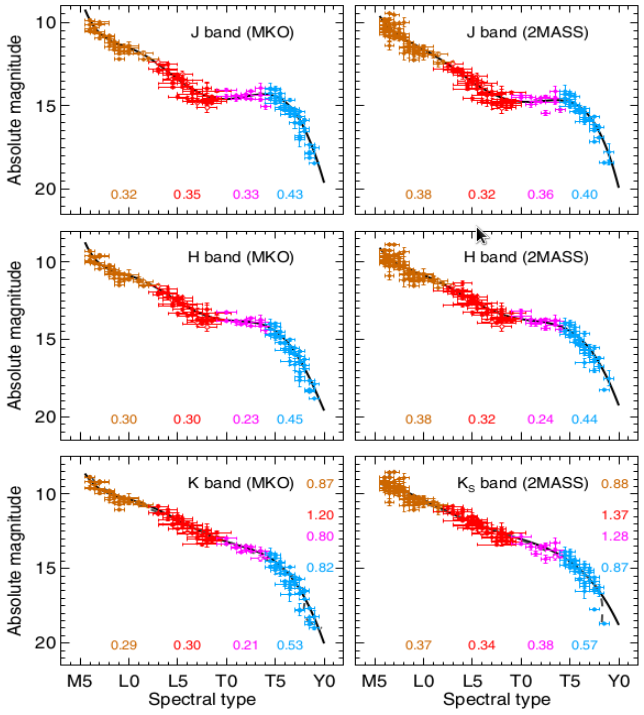

Figure 2.2: The polynomial fit for MKO and 2MASS (Figure 25 of Dupuy & Liu 2012).The figure shows NIR absolute magnitudes as a function of spectral type (for all ultra-cool field dwarfs with parallaxes but not including known young or planetary mass object and sub-dwarfs).

2.2.1.2 Calculation of photometric distance

Given the lack of parallax measurements for UCDs in DA, the use of absolute magnitude-spectral type relations became fundamental in obtaining the photometric distance for my target UCDs. The spectral type for most of the objects in DA is provided either in optical and/or in NIR. Late M and L dwarfs can be detected in both optical and NIR bands and I have selected the optical spectral types over the NIR types when both are available. There is no ideal option here, hence my choice to follow general conventions. I note that optical and NIR spectral types differ most severely for unresolved UCD binary systems, because the earlier (hotter) component dominates the optical flux and the later (cooler) component contributes more substantially in the NIR. However, I excluded objects that are known or suspected to be unresolved binaries. One more reason to pick optical spectral types over the NIR ones is that using NIR spectral types for all objects would result in polynomial relations different by 0.01-0.02 magnitudes for MKO bands and 0.03-0.06 magnitudes for 2MASS bands. On the other hand, T dwarfs can only be detected and are much more luminous in NIR bands due to the decline in T_{eff}. Note I have excluded all the objects with peculiarity in their spectral types because they would affect the accuracy of the calculated absolute magnitude from the polynomial equation further (Dupuy & Liu 2012).

An accurate determination of the distance is always crucial in minimising uncertainty in any astrophysical study. Hence many factors that can affect the outcome of the photometric distance in this case needed to be look in to, and to be corrected. I discussed above my choice in terms of spectral type. The next important step was to apply the appropriate polynomial, depending on the photometric system in which the apparent magnitudes of the UCDs were measured. DA photometry is a mixture of different systems (mostly the MKO and the 2MASS system) and I needed to

determine which system was appropriate for each object and convert as required. All 2MASS UCDs were apparent from their discovery name. I also employed the Leggett L and T dwarf archive (Leggett et al. 2010) to identify (and confirm) measurements made on the MKO system.

Next, to identify objects that were measured in the 2MASS system, I have uploaded all objects without measured MKO photometry onto Gator, NASA/IPAC Infared Science Archive (IRSA) to X-match with the 2MASS catalogue objects. I then uploaded the leftover DA objects that were not matched to both of the previous X-matched archives to the WSA, to X-match with UKIDSS to identify objects that were also measured in the MKO system. There were then only a few leftover from this last X-matching, and based on the high likelihood I assumed they were likely to be measured in the MKO system.

After determining the photometric system for each object, I calculated distance moduli and distances using either 2MASS or MKO photometry, employing the polynomial equations from Dupuy & Liu (2012). An alternative approach would have been to convert the 2MASS magnitudes into MKO magnitudes, using for example the conversion published by Stephens & Leggett (2004). However this would have introduced another systematic error into my calculation, hence I have rejected this possible solution. Since Gator and WSA only required the co-ordinates of the objects in degrees, I have then X-matched those objects, along with their associated rms, with the original reduced data using TOPCAT, to combine them back into one table.

Although a vast number of parallaxes are missing in DA, of course measured distances are more accurate than those I have calculated using photometry and spectroscopy (i.e. the polynomial fits from Dupuy & Liu 2012). Hence I have obtained the minimum distance (Dmin) and maximum distance (Dmax) to each UCD in two different ways, depending on whether the parallax and its error were given by the catalogue or not. Note that instead of using the available measured parallaxes from DA, I used the more up-to-date inventory complied by Dupuy & Liu (2012), containing all UCDs with direct distance measurements, providing position, parallax and proper motion (i.e. the astrometry of the object), and both MKO and 2MASS photometry (either from published measurements or synthesized from any spectra available) for each object. Other photometry is also included if available, i.e. Spitzer/IRAC (all channels), WISE (flags of data quality and upper limits included) and SDSS (from DR7 onward). Additional information is also provided, i.e. spectral types determined from both optical and NIR bands, flags for unusual properties (e.g. being a member of a young moving group, have low metallicity or low gravity, etc.), information on the high-angular resolution imaging, and information on the companion/s if the object is part of a multiple system. Note that the data table presented by Dupuy & Liu (2012) is constantly updated whenever new parallaxes become available.

The first way to calculate Dmin and Dmax is to use the distance-parallax equation for objects that have the parallax error (σ_π) provided. Since the parallax is measured in milliarcseconds (mas), I have multiplied both (1) and (2) by 1000 to convert it back to arcseconds (as). Then dividing by the parallax plus its error gives the Dmin and dividing by the parallax minus its error gives the Dmax as shown below:

$$\mathrm{D_{min}} = \frac{1000}{\pi + \sigma_\pi} \qquad (1)$$

$$\mathrm{D_{max}} = \frac{1000}{\pi - \sigma_\pi} \qquad (2)$$

For objects that do not come with measured parallax, to calculate Dmin and Dmax, I had to first work out the error on the distance of the UCD ($\Delta \mathrm{D}_{UCD}$). I considered two solutions to determine the

$\Delta \mathrm{D}_{UCD}$. The first way is to apply the propagation of uncertainty to work out the $\Delta \mathrm{D}_{UCD}$ by using the distance modulus equations. However, I ended up using the magnitude-flux and distance-flux relations to work out the percentage error for the distance since it is less time consuming.

The change in magnitudes (Δm) can be converted to a variation in brightness (flux):

$$\frac{f_2}{f_1} \approx 2.5^{\Delta m} \quad (3)$$

I first used the magnitude-flux relation where M_J is the magnitude measured in the *J* band.

$$M_J \sim 2.5 \log(f) \quad (4)$$

Rearranging for f:

$$f = 10^{\frac{M_J}{2.5}} \quad (5)$$

Then I used the distance-flux relation (inverse square law):

$$f \propto \frac{1}{d^2} \quad (6)$$

Rearranging for d:

$$d \propto \sqrt{\frac{1}{f}} \quad (7)$$

Substituting (5) into (7):

$$d \propto \sqrt{\frac{1}{10^{\frac{M_J}{2.5}}}} \quad (8)$$

Given the percentage error with respect to M_J is:

$$\Delta d\%(M_J) = d - 1 \quad (9)$$

However, I have to take into account that M_J has two types of error, M_J(spt) with respect to the spectral type and M_J(rms) with respect to the rms from the Dupuy & Liu (2012) equation.

Moreover, $\Delta d\%(J)$ which is the percentage error of *J* (where the error of Jmag, σ_{Jmag}, is provided by DA) is calculated by:

$$\Delta d\%(J) = \frac{\sigma_{\mathrm{Jmag}}}{\mathrm{Jmag}} \times 100 \quad (10)$$

The final formula I used to calculate the percentage error propagation:

$$\Delta D(\%)\ or\ Derror = \sqrt{\Delta d\%(J)^2 + \Delta d\%(M_J(\mathrm{spt}))^2 + \Delta d\%(M_J(\mathrm{rms}))^2} \quad (11)$$

The steps described in equations (3) to (11) are equivalent to rearranging the distance modulus equation and determining the distance uncertainty from that. Note that the error for $M_J(\mathrm{spt}) = \pm 0.5$, this is because I assumed the uncertainty of the spectral type to be half a spectral type. Further, the error for $M_J(\mathrm{rms}) = \pm 0.4$ since the error for $M_J(\mathrm{rms})$ is between 0.39 and 0.40 depending on the system used (Dupuy & Liu 2012). Given that the difference is very small, and to be more conservative, I picked the larger value of the two to be the standard rms error for this particular calculation.

The candidate associated object (UCD in this case) must have a distance larger than the Dmin of the star and smaller than the Dmax of the star to be considered a companion. After I have calculated the error on the distance of the star (ΔD_{star}) and have deduced ΔD_{UCD}, I then used them to work out Dmin and Dmax (note that the 50 kAU constraint was not included in this calculation as it is negligible in comparison to ΔD_{star} or ΔD_{UCD} which are around 10 times larger or more):

$$D_{\min} = D_{star} - \Delta D_{star} - \Delta D_{UCD} \quad (12)$$

$$D_{\max} = D_{star} + \Delta D_{star} + \Delta D_{UCD} \quad (13)$$

I have in Figure 2.3 plotted the distribution of objects in relation to their distance. Objects with measured parallaxes are plotted in black, while objects without are plotted in red. The parallax distances were taken straight from DA, but for the remaining objects I needed to estimate the distance using the available spectroscopy and photometry. The figure shows that there are very few UCDs with distance below 10pc due to the small volume of space this represents. For greater distance the number increases as the space volume goes up, but then peaks and decreases. The parallax sample (black line) falls beyond ~15pc because only brighter UCDs (of any spectral sub-type) are targeted for parallax observations. The non-parallax sample peaks at ~20pc and falls at greater distance for two reasons; (i) spectroscopic follow up of UCD candidates is preferentially done for brighter candidates, and (ii) the photometric limits and uncertainties of the main UCD surveys lead to distance cut-offs and higher contaminations levels in selected samples. The sample is most numerous out to ~50pc, before falling off rapidly between 50 and 100pc.

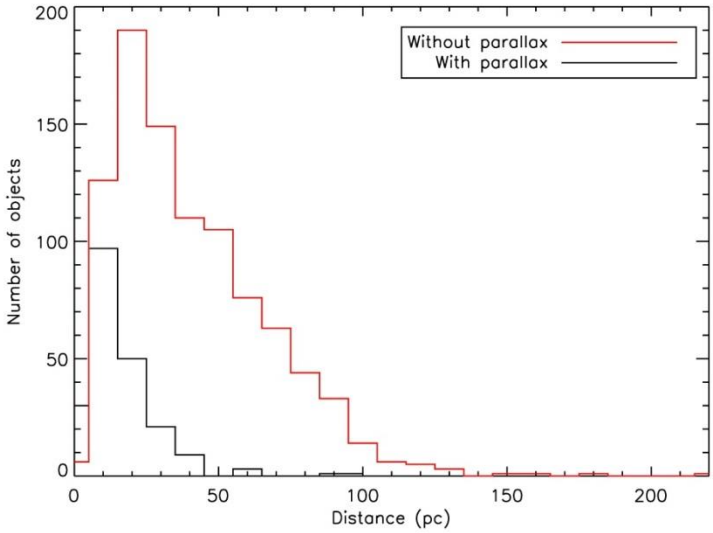

Figure 2.3: Number of UCDs versus distance in parsec. There is a higher population of objects at a closer distance than at a much further distance. Objects with measured parallax are plotted in black, while objects without are plotted in red. The population without parallaxes extends further than the one with parallaxes, due to the challenge of measuring parallaxes at large distances.

2.2.2 Distances for HMC

The HMC parameters that I used in my analysis are right ascension (α), declination (δ) at the J2000 epoch, apparent magnitude (Vmag), parallax (π), proper motion in the right ascension direction (μ_α), proper motion in the declination direction (μ_δ), colour (*B-V*), spectral type (spt), and their associated

uncertainties. I took parallax measurements and associated errors to determine distance limits as before. In order to select only good quality measurements, I have imposed a limit on the uncertainty of the HMC parallaxes of 10% or better, because Hipparcos parallaxes are only good quality if their uncertainty is 10% or better. As a result, the catalogue was downsized by a factor of ~6 with only 20871 objects left.

I have in Figure 2.4 plotted a distance histogram to see the distribution of objects in relation to their distance. The black histogram shows all of Hipparcos targets, while the red one shows only objects with uncertainties within 10%. The figure shows the number of objects increases until around 100-150 pc, because the volume sampled increases. After that as the distance increases, the number of stars decreases due to reduced photometric sensitivity and incompleteness. However, the number of objects with good parallaxes only increases up to 60 pc, and only extends to 200 pc. For distances above 60pc the frequency of good quality Hipparcos parallaxes decreases due to the typical lack of bright stars and the limiting magnitude of Hipparcos (van Leeuwen 2007). Note that the plot only shows the distribution out to 500 pc, but Hipparcos contains objects with reported distances out to 100 kpc. The distances near 100kpc are very inaccurate, and dominated by uncertainty. Note that there is a good match between the most populated distance range of the photometric distance sample from DA (≤50pc) and the <10% sample from HMC (≤60pc).

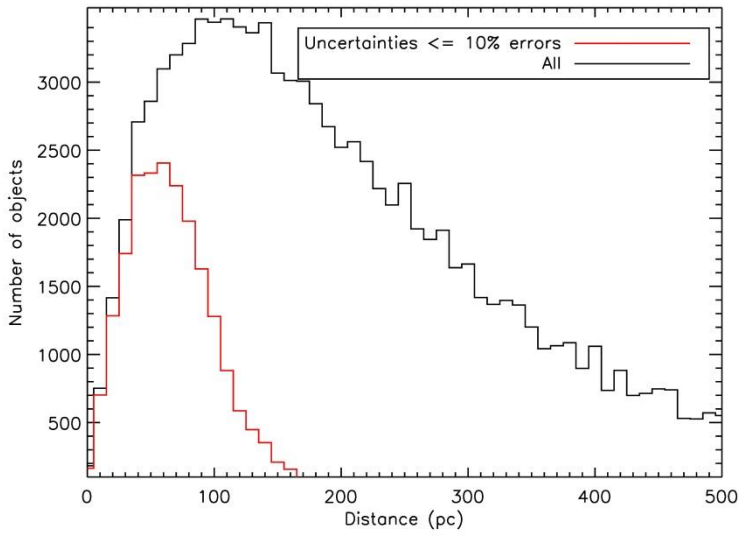

Figure 2.4: Number of stellar objects versus distance in parsec. The entire sample is plotted in black, while objects with uncertainties ≤ 10% are plotted in red. There is a higher population of objects at intermediate distance than at a much further distance. This is because of the limiting magnitude of Hipparcos. Objects with good quality parallax (i.e. uncertainties ≤ 10%) only extend out to 200 pc.

I have in Figure 2.5 plotted a colour magnitude diagram with the HMC data to see the distribution of types of objects. The entire sample is plotted in black, while objects with uncertainties ≤ 10% are plotted in red. The entire sample shows a lot of scatters on the colour-magnitude diagram, forming a cloud of points. There are objects extending out to B-V=5.6 but those measurements are probably dominated by uncertainty. The 10% sample takes the shape of the Hertzsprung-Russell (HR) diagram. The curve extending from the top left corner to the bottom right corner in the figure represents the main sequence, the shorter curve extending from the right corner to the middle of the main sequence represents the red giants. A small population of white dwarfs shows in the

bottom left corner. The majority of objects in the <10% sample are FGK main sequence stars (*B-V*<1.3), with reduced numbers of M dwarfs (*B-V*>1.3) due to their optical faintness. There are also a significant number of evolved stars in the form of sub-giants and giants. Such objects are intrinsically brighter than main sequence stars of the same temperature (and thus measurable out to greater distance), though lower space density (since the giant phase happens on a much shorter time-scale than the main sequence phase) acts to reduce their number in the HMC sample. Only a small number of white dwarfs and sub-dwarfs (below the main sequence) are in the <10% sample due to their intrinsic faintness and lower space density. Thus the HMC provides good coverage of potential disintegrating multiple components with FGK types out to ~60pc, with a somewhat reduced sensitivity to M dwarfs and evolved giants, and very low white dwarf and sub-dwarf numbers.

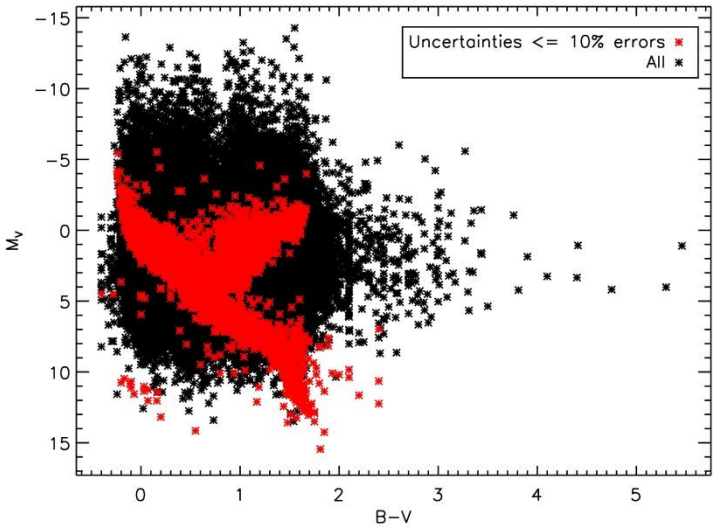

Figure 2.5: Colour magnitude diagram with the data from the HMC. The entire sample is plotted in black, while objects with uncertainties ≤ 10% are plotted in red. The 10% sample takes the shape of the HR diagram. The longest curve extending from top left to bottom right is the main sequence. Red giants are represented by the shorter curve from the top right to the mid main sequence. A small population of white dwarfs is at the bottom left of the figure.

Since HMC also provides parallaxes measured in mas, hence to calculate Dmin and Dmax I used equation (1) and (2) as above.

2.2.3 Distances for GJC

The GJC parameters that I used in my analysis are right ascension (α), declination (δ), proper motion (μ), spectral type (spt), apparent magnitude (Vmag), colour (*B-V*), parallax (π), absolute apparent magnitude (M_V) with their associated errors.

I have in Figure 2.6 plotted a distance histogram to see the distribution of objects in relation to their distance. The figure shows that there are very low numbers closer than 10pc, while the majority of the objects are between 10 and 20 pc, and as the distance increases, fewer objects are found. The distribution is flat (the number of objects is roughly constant) in the 10-25pc range, which shows the incompleteness - I would expect more stars at greater distance, due to an increased volume (i.e. the histogram should have an uphill climb). Note that Gliese is just a catalogue, not a survey. So it was constructed as a catalogue containing objects with parallax distance of 25pc or less. Over time these measurements can change a bit as parallaxes improve. So there is a tail of Gliese stars above 25pc.

The GJC sample provides a good distance match to the peak of the DA histogram, but (due to its design) fails to cover the >25pc range.

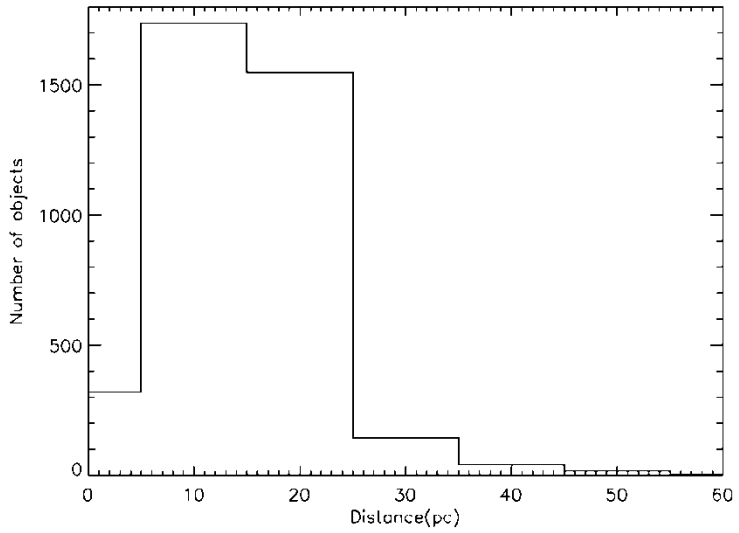

Figure 2.6: Number of stellar objects versus distance in parsec. There is a higher population of objects at closer distance than at a much further distance.

I have in Figure 2.7 plotted a colour magnitude diagram for the GJC data to see the distribution of types of objects. The curve extending from the top left corner to the bottom right corner in the figure represents the main sequence. The GJC sample is dominated by M dwarfs, making a good complement to the HMC. A small population of red giants and sub-giants is shown just above the middle of the main sequence. The shorter curve parallel to the main sequence represents white dwarfs. Although the number of white dwarf is much lower than the number of main sequence stars, there are many more white dwarfs in GJC than in the HMC, thanks to the efforts of the white dwarf community measuring parallaxes. There are also a higher percentage of sub-dwarfs presumably due to targeted follow up within the community. GJC provides good coverage of potential disintegrating multiple components with M spectral type out to 25pc, and offers a significant improvement over the HMC for white dwarfs and sub-dwarfs in this range.

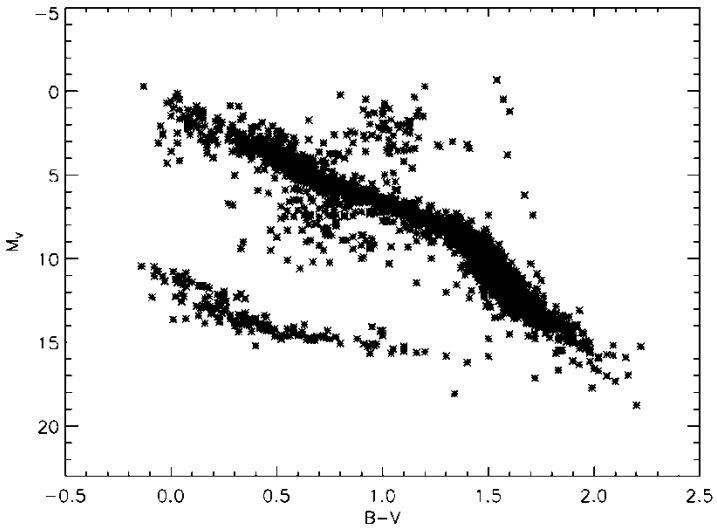

Figure 2.7: Colour magnitude diagram with the data from the GJC. The longest curve extending from top left to bottom right is the main sequence. A small population of red giants shows on top of the mid part of the main sequence. The shorter curve parallel to the main sequence is the white dwarf population.

Though, the errors in proper motion (σ_μ) are lacking in this catalogue and I needed this parameter to calculate the Gaussian error (section 2.6) later on. The proper motion quoted in GJC is taken from either the Tycho catalogue, the Hipparcos catalogue or the USNO catalogue. Stauffer et al. (2010) quote typical uncertainties of 2.5 mas/yr for the brightest stars in the catalogue. Note that this value can be underestimated for fainter stars however, since in this work I focus only on the brightest nearby stars then the real uncertainty will not be too different from the value given by Stauffer et al. (2010). From this point onward, I will therefore consider as Gaussian error on the GJC proper motion the value of 2.5 mas/yr.

2.3 UCD sample properties

I now plot various properties of the UCD sample, combing catalogue measurements with my distance determinations. This shows sensitivity biases across the sky, as well as the spectral type and magnitude distribution of DA. It indicates likely uncertainties in the photometric distances due to photometric scatter and unresolved binarity, and also highlights a small fraction of unusual UCDs in the sample (red and blue outliers).

First, from the DA catalogue, in Figure 2.8, I have plotted the right ascension (α) versus declination (δ). The plot shows the lay out of the UCDs on the sky. Objects with measured parallax are plotted in black, while objects without are plotted in red. It can be seen that the population is densest along the equator. Clearly there is a lack of UCDs in the Galactic plane region. This is because BDs are difficult to identify when there is lots of contamination from reddened objects. The distribution of objects with measured parallax is more homogeneous. There is an over-density of UCDs in the Northern hemisphere. This is due to the non-uniform coverage of the sky, i.e. the Northern hemisphere has been more thoroughly mapped by survey such as UKIDSS and SDSS. The ongoing VISTA survey will compensate in the Southern hemisphere. The over-density of UCDs near the celestial equator is due to follow-up of 2MASS and SDSS early data releases (e.g. Cruz et al. 2007; Chiu et al. 2006).

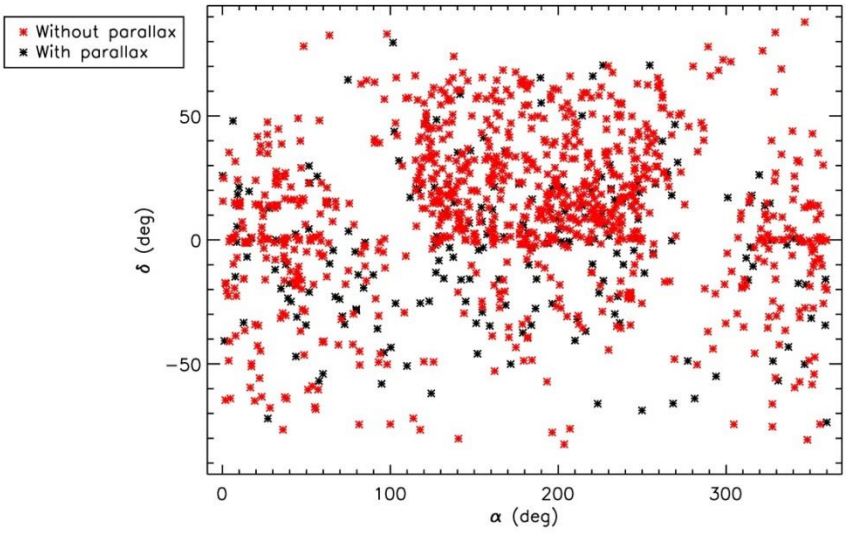

Figure 2.8: The right ascension (α) versus declination (δ) plot from the DA data shows the distribution of UCDs on the sky. Objects with measured parallax are plotted in black, while objects without are plotted in red. The population of UCDs is densest along the equator.

Next I have plotted a series of colour magnitude diagrams and Figure 2.9 below is one where *J-K* versus *J* magnitude is plotted. The objects plotted in black are the ones with parallax and the objects plotted in red are the ones without. Although this plot shows apparent magnitude against colour, the approximate division between L and T dwarfs is still clear from the colours, with the more numerous L dwarfs redder than *J-K*=1 and the less numerous T dwarfs much bluer than this. There are a small number of brighter T dwarfs in the upper left corner of the plot whose parallax measurements show that they are very nearby, and in general it can be seen that there is a preference to measure parallaxes for the brightest examples at any spectral type. In between the L and T dwarfs there are the L/T transition objects, whose relative rarity (and difficulty to identify in the NIR) means that there are very few nearby examples and those with parallax lie at *J*∼16 (see above section 1.2.3 to 1.2.6 for more information).

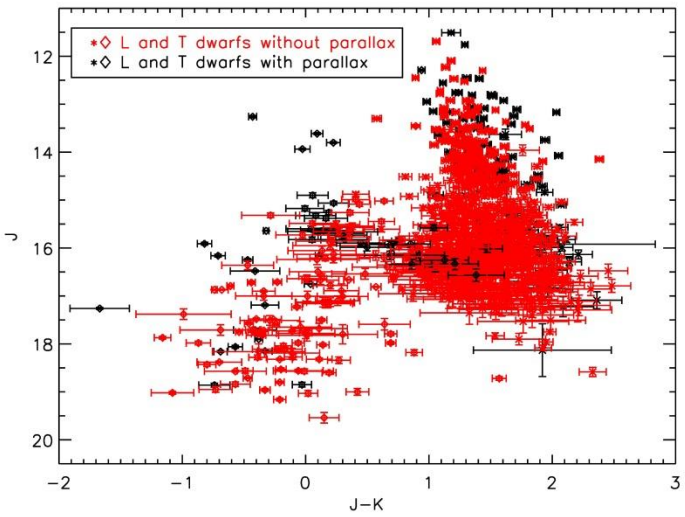

Figure 2.9: The colour of the UCDs versus the brightness of the UCDs. Objects plotted in black are the ones with measured parallax and objects plotted in red are ones without. Star symbols indicate L dwarfs and open diamonds indicate T dwarfs. The brighter objects are M and L dwarfs, with *J* between 15 and 16 there is the L/T transition, T dwarfs are the faintest and bluest objects.

I show in Figure 2.10 the absolute *J* magnitude against the *J-K* colour. Objects with measured parallax are plotted in black as usual, while objects without are plotted in red. It can be seen that objects with photometric distance form horizontal lines (one for each spectral type), due to the quantised nature of spectral types and the polynomial relations used to determine their absolute magnitude, while those with parallax are more evenly distributed. Objects with photometric distance also show a larger scatter.

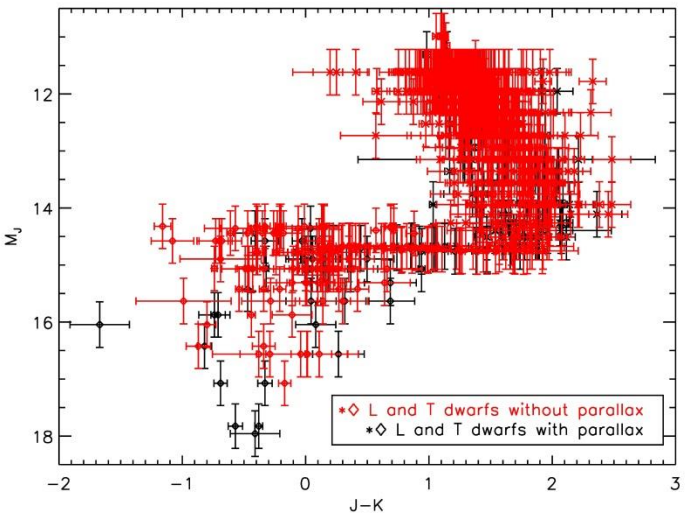

Figure 2.10: The colour of the UCDs versus the absolute *J* magnitude of the UCDs. Objects with measured parallax are plotted in black, while objects without are plotted in red. Star symbols indicate L dwarfs and open diamonds indicate T dwarfs. Objects without measured parallax show a larger scatter in colour with spectral type.

In Figure 2.11 I show M_K as a function of *J-K*. As usual black symbols indicate objects with measured parallax while red symbols indicate objects without. In comparison to Figure 2.10 the population shows a larger scatter because of the presence of colour outliers – e.g. red and blue L and T dwarfs (e.g. Folkes et al. 2007; Faherty et al. 2009; Schmidt et al. 2010; Mace et al. 2013; Marocco et al. 2014). Only a small fraction of objects are outliers and can be seen easily because they lie outside of the main sequence containing the majority of UCDs. Colour outliers are due to the sensitivity of the *J-K* colour to metallicity and surface gravity. The same effect is seen in the population of objects with measured parallaxes. The main difference between this figure and Figure 2.10 is the slope of the sequence between the reddest L dwarfs and the mid T dwarfs. This is due to objects getting fainter in *K* in this range. Conversely L/T transition objects remain about the same brightness in *J*, and even get slightly brighter for the early T dwarfs.

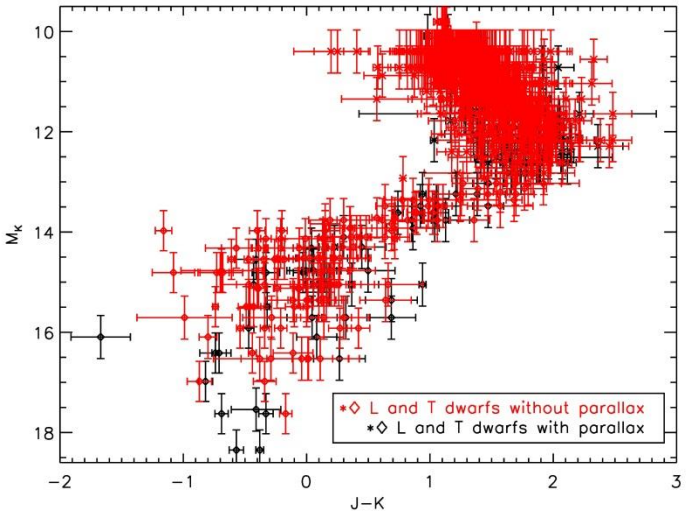

Figure 2.11: The colour of the UCDs versus the absolute *K* magnitude of the UCDs. Objects with measured parallax are plotted in black, while objects without are plotted in red. Star symbols indicate L dwarfs and open diamonds indicate T dwarfs. Objects without measured parallax show a larger scatter in colour with spectral type.

I have plotted in Figure 2.12 the absolute magnitude in J band (M_J) as a function of spectral type and have obtained the same L/T transition trend (see above sections of 1.2.4 and 1.2.5) as Figure 8 in Knapp et al. (2004). The objects in black are the ones with measured parallax and the objects in red are the ones without. Objects in red follow exactly the polynomial from Dupuy & Liu (2012). It can be seen that in the L/T transition the slope of the two polynomials (i.e. the MKO and the 2MASS one) is significantly different. This could be due to the greater sensitivity of the UKIDSS filters to the settling of dust. Objects with measured parallax show a larger scatter. In particular unresolved binaries and young objects are over luminous and so sit above the polynomial. The unresolved binary sequence (along with any young objects not fully contracted) is very clear in this plot, lying ~0.75 magnitudes above the single star sequence, defined by the red objects. This means that any unresolved binary without parallax measurements would have its absolute *J* magnitude over

estimated, introducing a systematic error into the distance measurements. Note that the brightening of the L/T transition only occurs in the J-band.

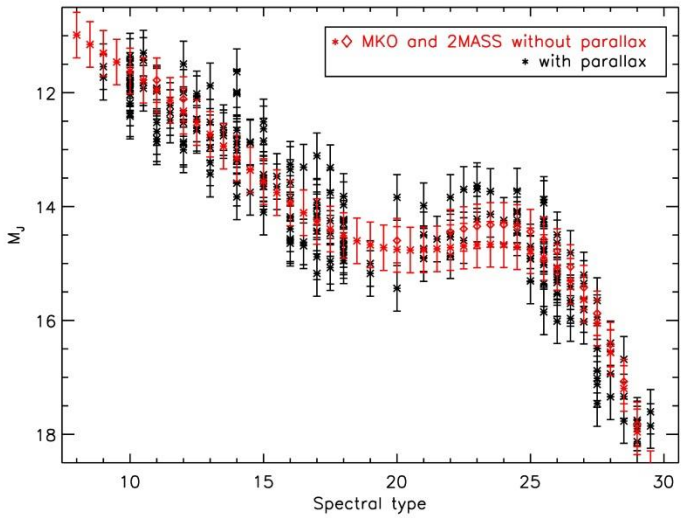

Figure 2.12: Spectral type versus M_J. This plot shows the transition pattern between L dwarfs and T dwarfs in the J band. The objects plotted in black are the ones with measured parallax and the objects plotted in red are the ones without. Objects in red follow the Dupuy & Liu (2012) polynomial, while objects in black show a larger scatter due to the presence of young objects and unresolved binaries. Star symbols indicate objects following the MKO polynomial and open diamonds indicate objects following the 2MASS polynomial.

I have also plotted in Figure 2.13 the absolute magnitude in *K* band (M_K) as a function of spectral type as Figure 9 in Knapp et al. (2004). Similarly to the previous plot, objects with measured parallax are plotted in black, while objects without parallax are plotted in red. This figure show the same L/T transition pattern as in *J* band but flatter, this is because the L/T transition pattern is mostly dependent on the dust clouds and in comparison the *K* band is less sensitive to the dust than the *J* band. For the same reason, there is no difference between the two polynomials (i.e. MKO ad 2MASS). Unresolved binaries and young objects appear over-luminous.

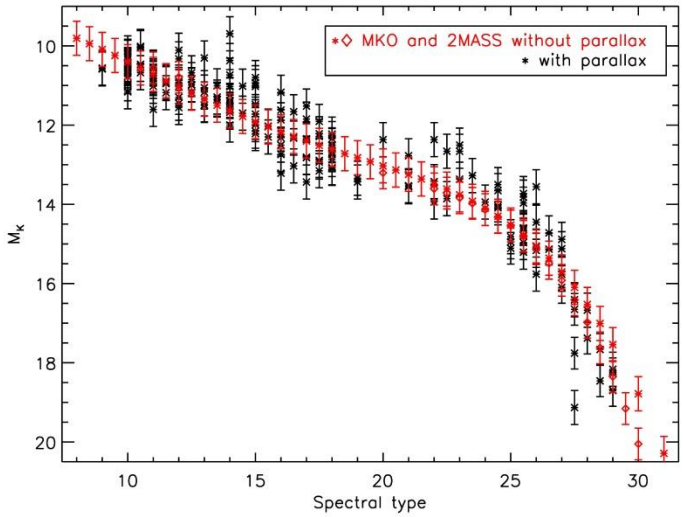

Figure 2.13: Spectral type versus M_K. This plot shows the transition pattern between L dwarfs and T dwarfs in the *K* band. Objects with measured parallax are plotted in black and objects without are plotted in red. Objects in red follow the Dupuy & Liu (2012) polynomial, while objects in black show a larger scatter due to the presence of young objects and unresolved binaries. Star symbols indicate objects following the MKO polynomial and open diamonds indicate objects following the 2MASS polynomial.

I have also plotted in Figure 2.14 the absolute magnitude in H band (M_H) versus spectral type. Objects with measured parallax are plotted in black while objects without are plotted in red. Here the pattern have gotten even flatter due to the same reason as above that the *H* band is even less sensitive to dust than the K band. For the same reason there is no difference between the two polynomials from Dupuy & Liu (2012).

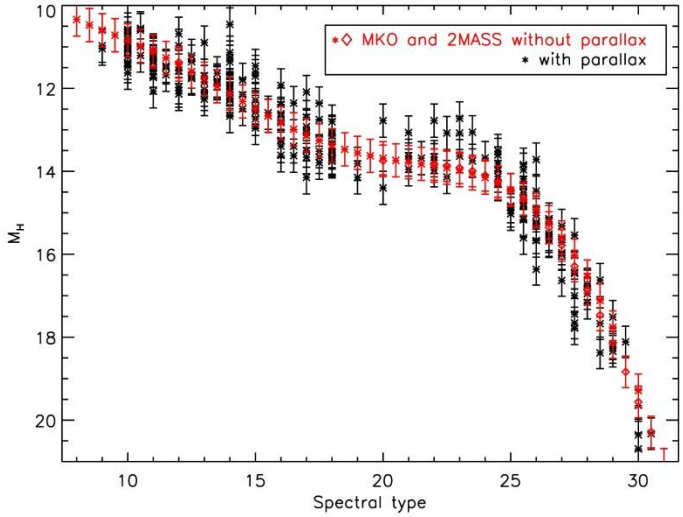

Figure 2.14: Spectral type versus M_H. This plot shows the transition pattern between L dwarfs and T dwarfs in H band. Objects with measured parallax are plotted in black while objects without are plotted in red. Star symbols indicate objects following the MKO polynomial and open diamonds indicate objects following the 2MASS polynomial.

Except for a few over luminous objects, which could be unresolved binaries (Dupuy & Liu 2012), one would assume the luminosity should decrease proportionally to the temperature as L dwarfs turn into T dwarfs. However, as mentioned above there is a brightening in luminosity at the L-T transition, before it decreases again. In general, it is mostly the dusty atmosphere of L dwarfs that causes the scattering of light, hence the redness of the spectrum. Whereas the much less dusty atmosphere of T dwarfs (with minimal scattering) causes the spectrum to be blue. Being cloudless leads also to the brightening of T dwarfs in the *J* band. There are also fewer objects in the L-T transition and this is because of the narrow range of effective temperature T_{eff} ≈ 1100-1400K (e.g., Kirkpatrick et al. 2000; Golimowski et al. 2004b; Vrba et al. 2004) covered by the transition.

Besides the descending T_{eff} (and the consequent formation and following removal of condensate clouds from the photosphere) it is also the change of dominant carbon-bearing molecule (from CO to CH_4) that causes the *J* brightening. There is a variety of one-dimensional models trying to reproduce the general changes of colours, spectra and magnitudes from late L dwarfs to mid T dwarfs, based on different prescriptions for the clouds (Marley et al. 2002; Tsuji 2002; Burrows et al. 2006). However there are difficulties in modelling clouds (e.g., Helling et al. 2008), and we still lack a robust physical theory (e.g. Helling & Casewell 2014; Marley & Robinson 2015). Hence none of the models up to date can accurately reproduce the entire colour-magnitude trend of L and T dwarfs (Saumon & Marley 2008; Allard et al. 2011).

2.4 Identifying initial candidate associations

2.4.1 Separation constraint

The aim of this work is to identify a set of possible multiple disintegrating systems within the 3 selected catalogues, for further study.

Disintegrating systems may have much in common observationally with gravitationally bound wide binary systems. However, they can differ in two key aspects. Firstly, consider that gravitationally bound multiple systems have their orbital velocities limited by Newton's law, and their relative velocities are expected to be much less than the systematic velocity. Observationally they are thus generally common proper motion systems. Disintegrating multiples are not limited in this way, and should have higher relative velocities if they are unbound systems. This means that they do not have to be common proper motion systems. Secondly, disintegrating multiples may be observed after the components have moved apart to some degree, and I would thus expect their separation range to extend to greater separations than those seen for bound systems. I address the proper motions of my candidate systems in a later chapter, but employed a separation constraint as part of my initial candidate selection.

Given the furthest separations known for wide stellar binary systems are approximately 200 kAU (e.g. Caballero 2010; Caballero et al. 2006), the stars would be so loosely bound together that gravitational interaction with other nearby objects could disrupt the system. Hence for the first constraint, I decided to apply a more conservative angular/separation limit. The objects had to be within maximum 10 arcmins and 50 kAU of each other, because I wanted a separation range that was wider than for typical multiple systems, and at the same time I wanted to limit the number of random matches. This way I identified candidate associations that include (i) disintegrating multiples that are gravitationally unbound, (ii) wide binary/multiple systems that are gravitationally bound,

and (iii) false groupings that are neither of these (i.e. contamination, or line-of-sight systems). Most known multiple systems containing a UCD have separations out to ~10 kAU, and a few are as wide as ~25 kAU (see references by Burgasser et al. 2005; Zhang et al. 2010; Faherty et al. 2010). So by going out to 50 kAU I was looking out to separations about twice as large as the widest multiples.

But I also needed to limit the separation range somewhat because one starts getting lots of contamination (chance alignments) at very wide separation. False line-of-sight associations are considered further in the section describing my candidate sample. At this point I chose an upper limit of 50 kAU as a reasonable mean of searching for unbound multiples with wider separation than is typically seen for known wide binaries.

Then I needed to avoid selecting just any two objects that appear to be very close together in the sky due to line of sight alignment, but with the other "component" being actually much further away. The second constrains is therefore based on the error of the measured distance, to have both objects within the same Dmin to Dmax distance range. This way the 'pair' would be confirmed to be a possible candidate association. Also while one object is within the 'range' of the other object then the angular distance between them is so small (small angle approximation) that they can be considered as sharing common distance.

2.4.2 Spatial/Distance associations

Candidate associations were defined so that the Dmin-Dmax range of one object overlaps with the Dmin-Dmax range of the other, potentially placing the two objects at a common distance (to within the observational constraints). In addition it was required that their physical separation be <50 kAU (equating to an angular separation limit at the average distance of the pair).

My complete X-matching procedure followed a 3 stage process. Initially I began with DA and searched for associated objects in DA itself and the HMC and GJC. I then carried out a similar analysis but starting with the HMC, and finally the GJC. In this way I was able to find disintegrating multiple candidates with any combination of constituents from the three catalogues. This procedure thus required me to identify and remove associations that were selected multiple times. This was done by scanning through the resulting pairs to pick out those that share the same spectral type and with their coordinates marginally close to each other (i.e. < 0.1 arcsec). I have then blinked through their images from SSS and SIMBAD to identify those duplicates and rejected them from the X-matching results.

Note that I did not set a maximum number of associated objects because I do not want to exclude any possible multiple associations to ensure a decent sample size. The only limitation is that all of the objects in the association had to be within an overall separation of 50 kAU. I have X-matched DA with HMC, DA with GJC, HMC with HMC, GJC with GJC and HMC with GJC. The results of the X-matching are described in the following paragraphs.

The results of the X-matching are summarized in Table 2.1. In Figure 2.15 I have plotted the separation distribution for the systems resulting from the X-matching between DA and HMC. It can be seen that the majority of the systems have separations within 1.5 arcminutes and only a few of them extend all the way out to 9 arcminutes. Since almost all of DA is closer than 100pc (see Figure 2.3) I would not expect to get many separations close to 50 kAU because this will be beyond 10 arcminutes. In Figure 2.16, I show a colour-colour plot for the UCD components of the DA-HMC systems. Objects with parallax are plotted in black, while objects without are plotted in red. The majority of the objects are on the top right corner of the plot, meaning that they are L dwarfs. A few of them extend towards the opposite corner, which is the location of T dwarfs. The sequence is

linear with only a couple of outliers lying below it. Figure 2.17 shows a colour-absolute magnitude diagram. The L-T sequence is visible from the top of the plot to the bottom left corner. The main feature is that the majority of the objects are L dwarfs, which are more numerous than T dwarfs in DA, and are intrinsically brighter so detectable in association with stars out to a greater distance. It can also be noted that the majority with measured parallaxes are late L dwarfs and T dwarfs. This is because parallax campaigns have focused mostly on the coldest objects (e.g. Smart et al. 2010, Marocco et al. 2010, Dupuy & Liu 2012). In Figure 2.18 I plotted a colour-absolute magnitude diagram for the stars and the BDs in the DA-HMC systems. BDs are plotted in black and the stars are plotted in red. I can see that the stars are main-sequence stars and the BDs cover the entire L-T range. Figure 2.19 shows absolute J magnitude against separation for the DA-HMC systems. The reason the 2 widest associations are L dwarfs is because wide associations are rare, so I expect them to come from amongst the most common type of UCD in DA, that are detectable as associations to stars out to larger distance.

Table 2.1: This table shows the number of candidate systems with multiples components from the DA-HMC X-match.

Number of components	Number of candidate systems
2	21
3	3

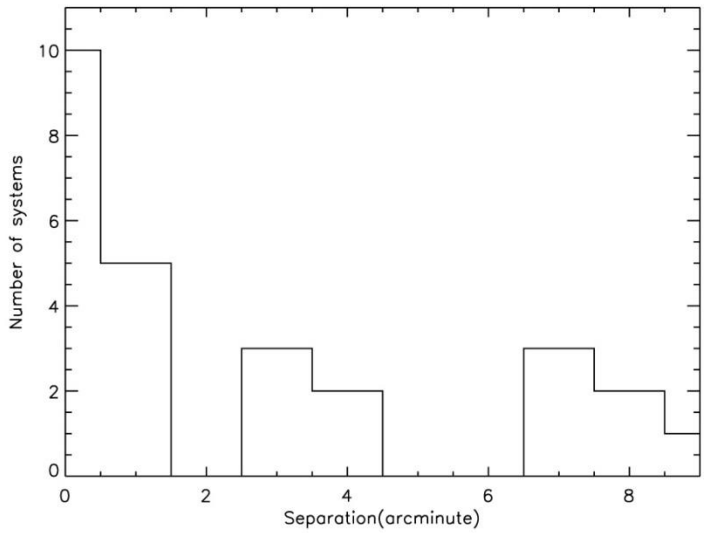

Figure 2.15: Separation histogram from the X-match between DA and HMC. The majority of the systems have separation within 1.5 arcminutes. Only few of them extend to 9 arcminutes.

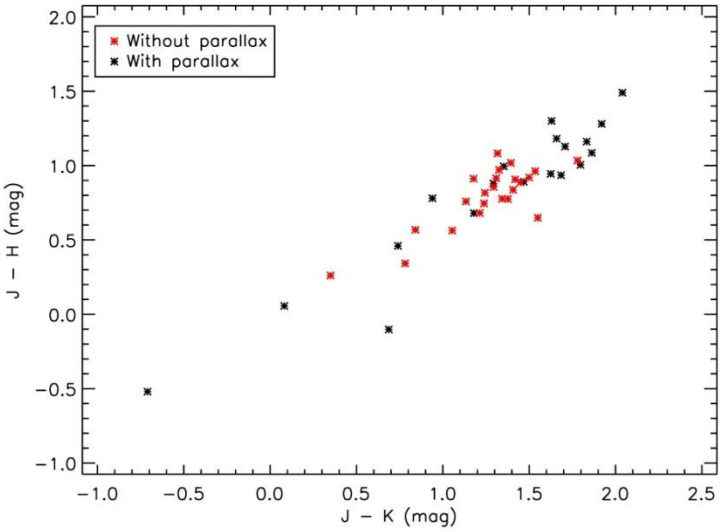

Figure 2.16: Colour-colour diagram for the UCD components of the DA-HMC X-matching data. Objects with parallax are plotted in black while objects without parallax are plotted in red. The L-T sequence extends from the top right corner to the bottom left corner.

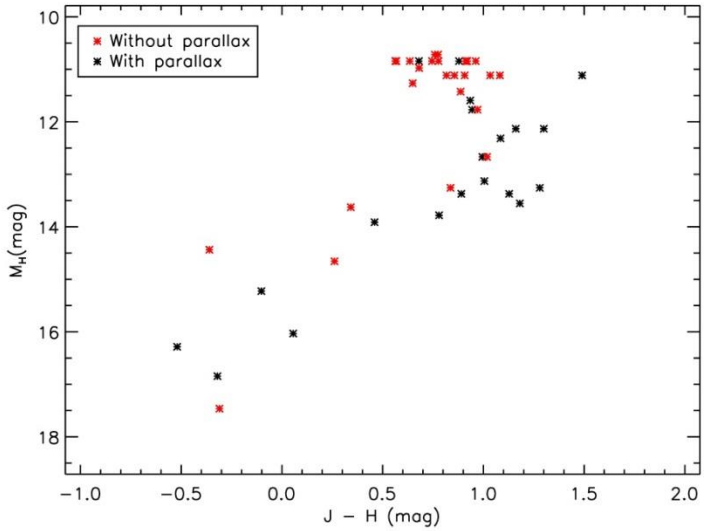

Figure 2.17: Colour magnitude diagram with the DA-HMC X-matching data. Objects with parallax are plotted in black while object without parallax are plotted in red. The L-T sequence extends from the top to the bottom left corner of the plot. The majority of the systems are L dwarfs.

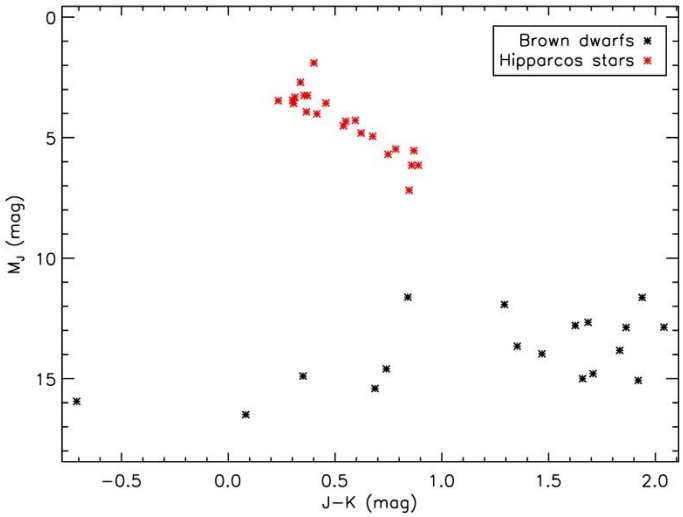

Figure 2.18: Colour magnitude diagram with the DA-HMC X-matching data. BDs are plotted in black while Hipparcos stars are plotted in red. The primaries are main-sequence stars while the BDs cover the entire L-T range.

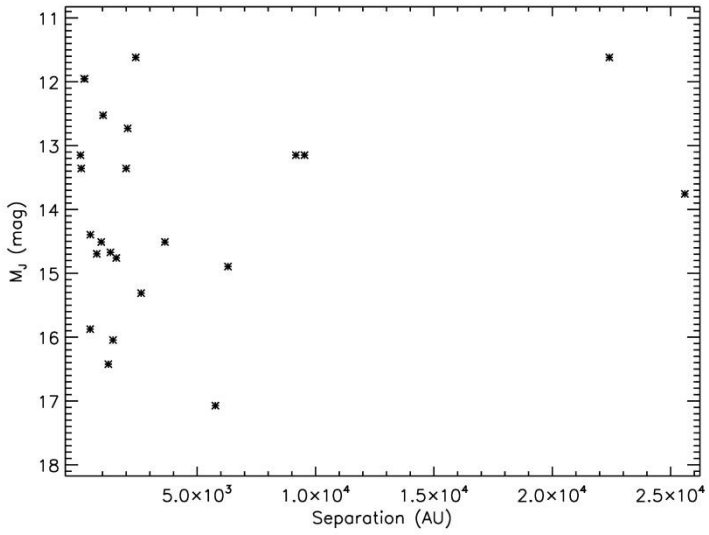

Figure 2.19: Absolute J magnitude against separation for the DA-HMC systems. Wide associations are rare and the 2 widest associations are L dwarfs, which are the most common type of UCD in DA.

The results of the X-matching are summarized in Table 2.2. In Figure 2.20 I have plotted the separation distribution for the systems resulting from the X-matching between DA and GJC. In a similar way as the DA-HMC systems, it can be seen that the majority of the systems have separation within 1.5 arcminutes and only a few of them extend all the way out to 9 arcminutes. In Figure 2.21, I show a colour-colour plot for the DA-GJC systems. Objects with parallax are plotted in black, while objects without are plotted in red. The majority of the objects are on the top right corner of the plot, meaning that they are L dwarfs. A few of them extend towards the opposite corner, which is the

location of T dwarfs. The sequence is linear with only 1 outlier lying below it. Figure 2.22 shows a colour-absolute magnitude diagram. The L-T sequence is visible from the top of the plot to the bottom left corner. The objects are evenly distributed across the full spectral type range. It can also be noted that the majority with measured parallaxes are late L dwarfs and T dwarfs. In Figure 2.23 I plotted a colour-absolute magnitude diagram for the stars and the BDs in the DA-GJC systems. BDs are plotted in black and stars are plotted in red. I can see that the stars are main-sequence stars with a couple of white dwarfs and the BDs cover the entire L-T range. Figure 2.24 shows absolute J magnitude against separation for the DA-GJC systems. Only the L dwarfs can be found at large separations. This is for the same reason explained above.

Table 2.2: This table shows the number of candidate systems with multiples components from the DA-GJC X-matching.

Number of components	Number of candidate systems
2	14
3	5

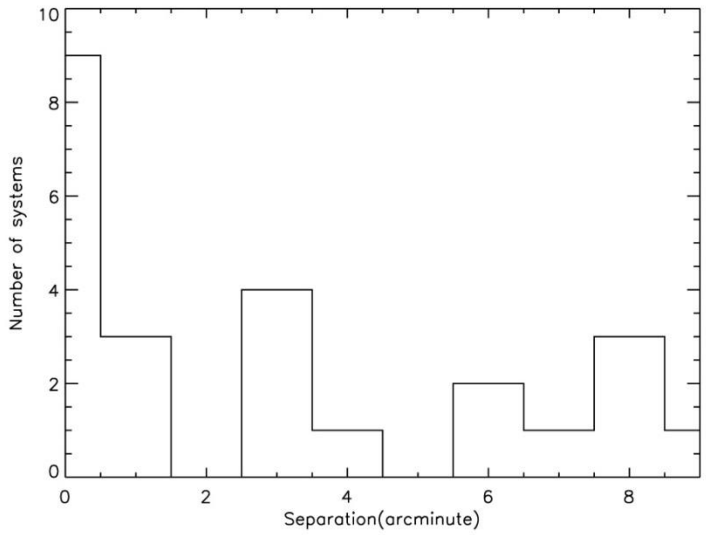

Figure 2.20: Separation histogram from the results of the X-match between DA and GJC. The majority of the systems have separation within 1.5 arcminutes.

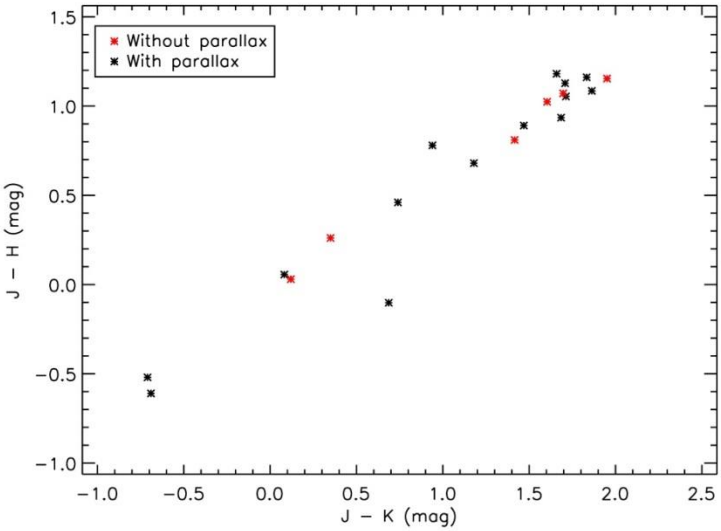

Figure 2.21: Colour-colour diagram with the DA-GJC X-matching data. Objects with parallax are plotted in black while objects without parallax are plotted in red. The L-T sequence extends from the top right corner to the bottom left corner.

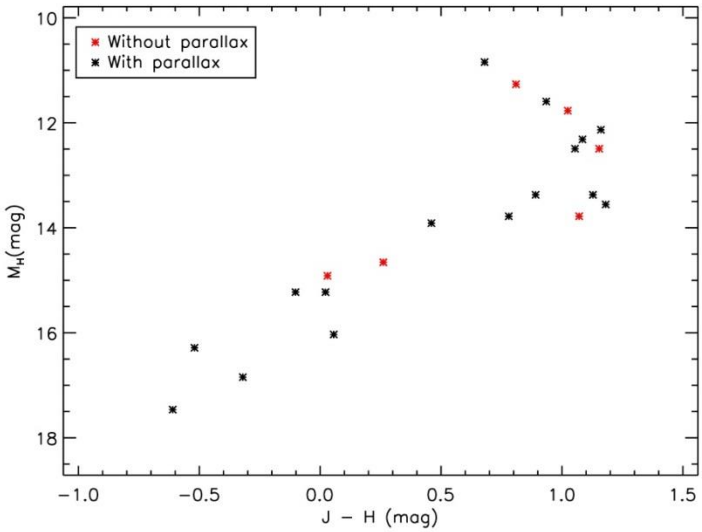

Figure 2.22: Colour magnitude diagram with the DA-GJC X-matching data. Objects with parallax are plotted in black while objects without parallax are plotted in red. The L-T sequence extends from the top to the bottom left corner of the plot. The systems are quite evenly distributed in the spectral sequence.

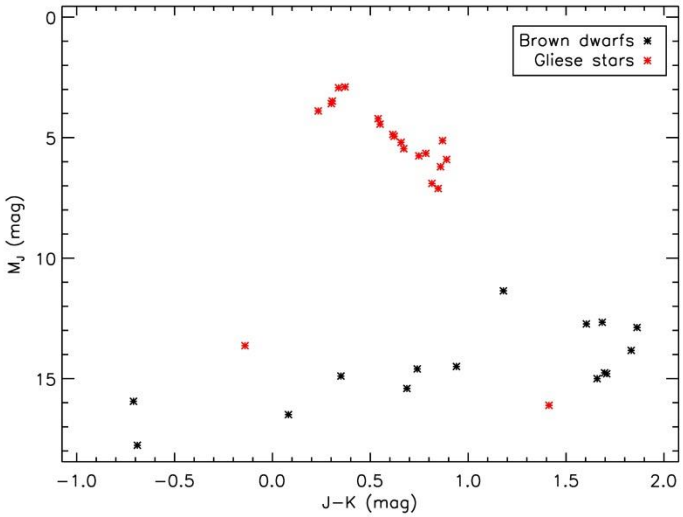

Figure 2.23: Colour magnitude diagram with the DA-GJC X-matching data. BDs are plotted in black while Gliese stars are plotted in red. The majority of the primaries are main-sequence stars but there are a couple of faint white dwarfs as well. BDs cover the entire L-T range.

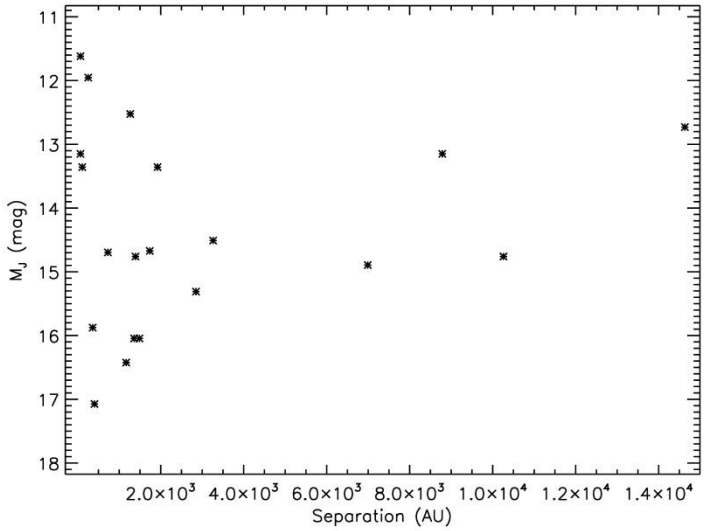

Figure 2.24: Absolute J magnitude against separation for the DA-GJC systems. Only L dwarfs are found at large separations.

The results of the X-matching are summarized in Table 2.3. In Figure 2.25 I have plotted the separation distribution for the systems resulting from the X-matching between Hipparcos stars. Systems within 50pc are plotted in black while systems outside this limit are plotted in red. The majority of the nearby systems have separation less than 500 AU, while the more distant systems extend out to larger separations, up to 3200 AU. In comparison there are more systems with large separations than in the DA-HMC and DA-GJC X-matches. Figure 2.26 presents a colour-magnitude diagram. The main sequence can be seen extending across the plot from the top left to the bottom

right corner. Red giants and sub-giants are on the top right corner, while white dwarfs are on the bottom left corner. The components of groups of 2 are plotted in black, the components of groups of 3 are plotted in red, and the components of groups of 5 are plotted in green. Most of the objects in groups of 3 and 5 are high mass early spectral type objects.

Table 2.3: This table shows the number of candidate systems with multiple components from the HMC-HMC X-match.

Number of components	Number of candidate systems
2	144
3	3
4	0
5	1

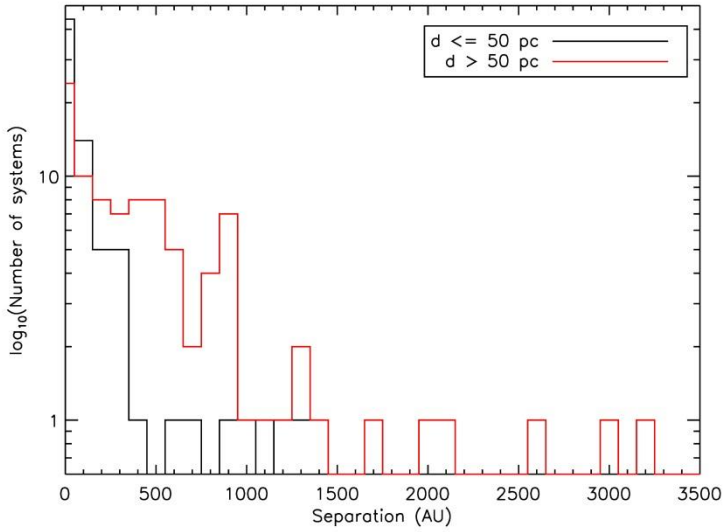

Figure 2.25: Separation histogram for the HMC-HMC X-match. Systems within 50pc are plotted in black while systems outside this limit are plotted in red. The sample in general contains systems with a wide range of separations and peak between 0 and 100 AU and decreases towards the maximum separation of 3200 AU.

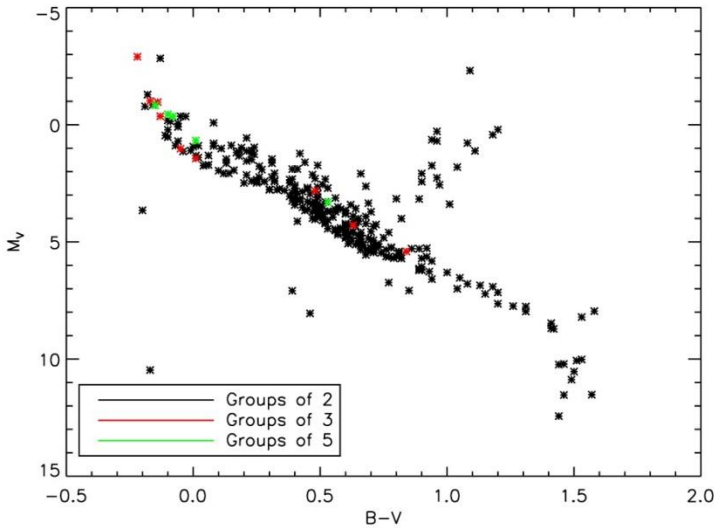

Figure 2.26: Colour magnitude diagram with the HMC-HMC X-matching data. Objects in groups of 2 are plotted in black while objects in groups of 3 are plotted in red and objects in groups of 5 are plotted in green. The figure shows the main sequence and the red giants, the longest curve extending from top left to bottom right and on top of the mid part of the main sequence, respectively. The population of LMSs is a lot sparser in comparison to the population of higher mass stars in the main sequence. Most of the objects in groups of 3 and 5 stars are high mass early spectral type objects. No white dwarfs or giants are found in multiple systems.

The results of the X-matching are summarized in Table 2.4. In Figure 2.27 I have plotted the separation distribution for the systems resulting from the X-matching between Gliese stars. Systems within 25pc are plotted in black while systems outside this limit are plotted in red. The vast majority of the systems have separations within 100 AU, and then the number of objects sharply drops by a factor of 5 for larger separations, then it slowly declines towards maximum separations of 250 AU. There are very few more distant objects and their distribution looks almost identical to the distribution of nearby objects. Figure 2.28 presents a colour-magnitude diagram. The main sequence can be seen extending across the plot from the top left to the bottom right corner. Red giants and sub-giants are on the top right corner, while white dwarfs are on the bottom left corner. Compared to Figure 2.26, there are a lot more LMSs and white dwarfs. Objects in groups of 2 are plotted in black while objects in groups of 3 are plotted in red. Objects in groups of 4 are plotted in blue and objects in groups of 5 are plotted in green. Objects in high multiplicity groups are evenly distributed along the sequence. In particular there seem to be a lot of LMSs in triple systems.

Table 2.4: This table shows the number of candidate systems with multiples components from the GJC-GJC X-matching.

Number of components	Number of candidate systems
2	474
3	33
4	3
5	1

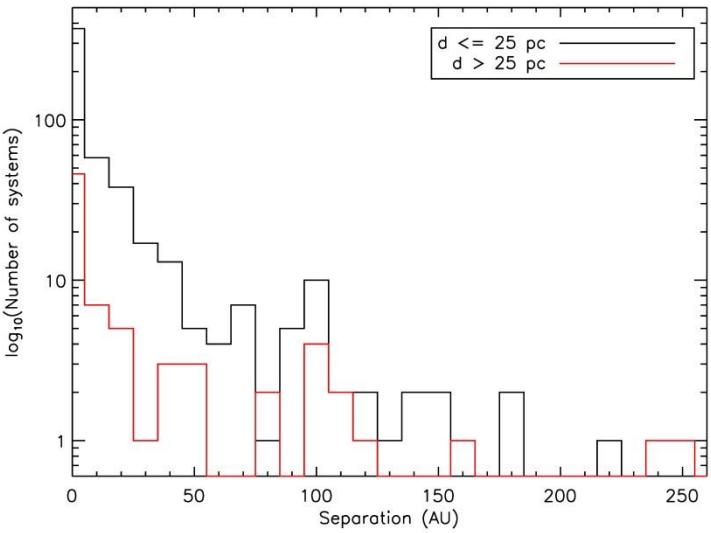

Figure 2.27: Separation histogram for the results of the GJC-GJC X-match. Systems within 25pc are plotted in black while systems outside this limit are plotted in red. The vast majority of the systems are within 100 AU.

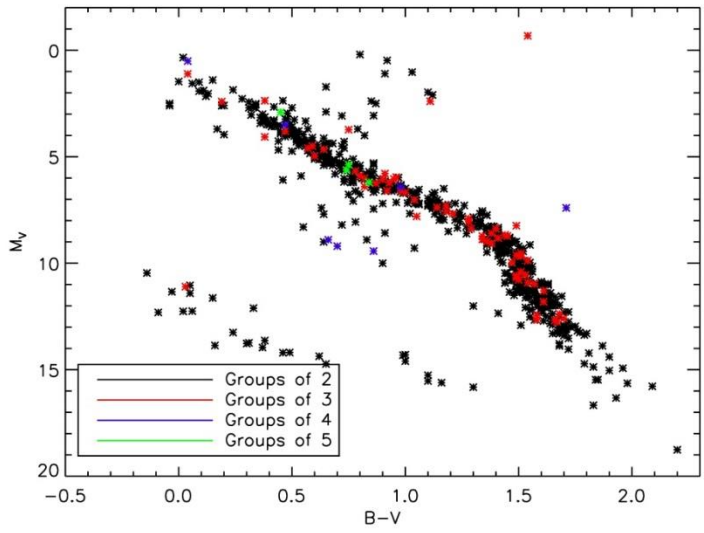

Figure 2.28: Colour magnitude diagram with the GJC-GJC X-matching data. Objects in groups of 2 are plotted in black while objects in groups of 3 are plotted in red. Objects in groups of 4 are plotted in blue and objects in groups of 5 are plotted in green. The figure shows the main sequence and the red giants, the longest curve extending from top left to bottom right and on top of the mid part of the main sequence, respectively. The population of high mass main sequence stars, red giants, and white dwarfs is smaller than the population of LMSs. The objects in high multiplicity groups are evenly distributed along the main sequence and even include red giants and white dwarfs.

The results of the X-matching are summarized in Table 2.5. In Figure 2.29 I have plotted the separation distribution for the systems resulting from the X-match between Hipparcos and Gliese stars. Systems within 25pc are plotted in black while systems outside this limit are plotted in red. The number of systems increases with separation and reaches the peak between 50 and 100 AU, then it declines towards a maximum separation of 300 AU. The distribution of more distant objects

increases as well, then reaches the maximum around 50 AU, but after that is essentially flat out to almost 200 AU. After that the number of objects drops. Figure 2.30 presents a colour-magnitude diagram. The main sequence can be seen extending across the plot from the top left to the bottom right corner. Red giants and sub-giants are on the top right corner, while white dwarfs are on the bottom left corner. Objects in groups of 2 are plotted in black while objects in groups of 3 are plotted in red. Objects in groups of 4 are plotted in blue, objects in groups of 5 are plotted in green and objects in groups of 6 are plotted in yellow. There are many objects in high multiplicity groups, and they are evenly distributed along the sequence. In particular the X-match produced associations with up to 6 components. Quite a few red giants and white dwarfs are found in multiple systems. Figure 2.26, 2.28 and 2.30 show that HMC is best for FGK stars associations, GJC is much better for M dwarfs and WDs, and when I combine them together (Figure 2.30) I get the best of both, with a wide range of objects being associated and some associations with more components in them (i.e. as many as 6 objects). This shows that the catalogues I am using are complementary, and that the way I do X-matching is effective and complete.

Table 2.5: This table shows the number of candidate systems with multiples components from the HMC-GJC X-match.

Number of components	Number of candidate systems
2	694
3	138
4	23
5	3
6	1

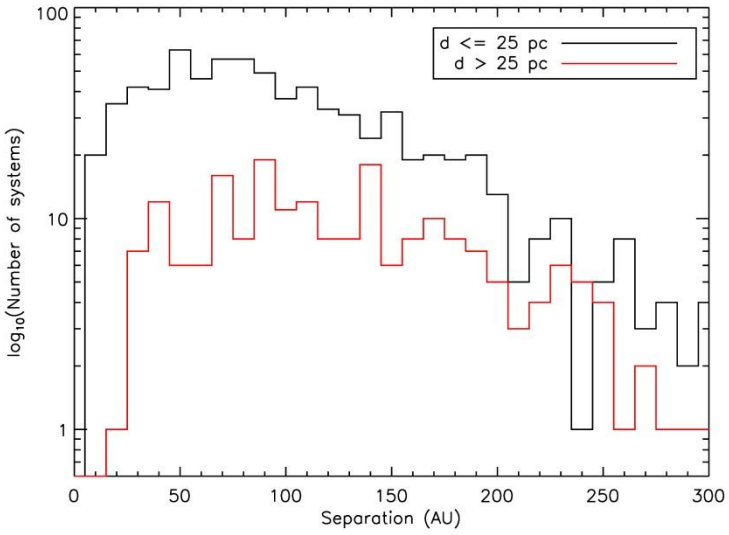

Figure 2.29: Separation histogram for the results of the HMC-GJC X-match. Systems within 25pc are plotted in black while systems outside this limit are plotted in red. The distribution of nearby objects peaks between 50 and 100 AU, while the distribution of distant objects is flat from 50 all the way to 200 AU.

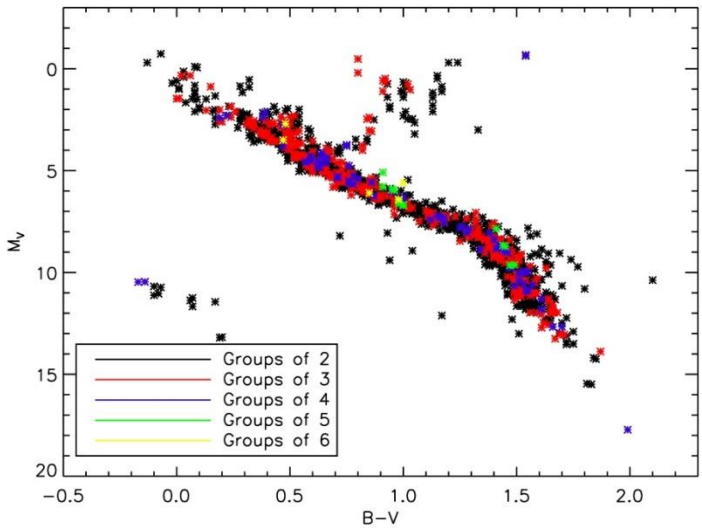

Figure 2.30: Colour magnitude diagram with the HMC-GJC X-matching data. Objects in groups of 2 are plotted in black while objects in groups of 3 are plotted in red. Objects in groups of 4 are plotted in blue, objects in groups of 5 are plotted in green and objects in groups of 6 are plotted in yellow. The figure shows the main sequence and the red giants, the longest curve extending from top left to bottom right and on top of the mid part of the main sequence, respectively. The population of high mass main sequence stars and red giants is smaller than the population of LMSs, and the population of white dwarfs is even smaller, limited to a few objects. The objects in high multiplicity groups are evenly distributed along the main sequence and even include red giants and white dwarfs.

2.5 Identifying common proper motion systems

One of the ways I used to separate gravitationally bound binary/multiple associations from unbound disintegrating multiple candidate associations is by using proper motion. Widely separated bound multiple systems should have common proper motion (CPM), while disintegrating systems can be non-CPM. To identify CPM systems I have selected only groups where the differences between the total PM of all components of the multiple system are within the combined error (Gaussian error). To identify ejected candidates, I selected only groups where the difference between the total PM of at least one component of the multiple system is larger than 3 times the combined error (Gaussian error). In general for the candidates involving DA (i.e. the DA-GJC and DA-HMC matches), not all the DA objects have PM measurements (only 35%). I carried out the CPM analysis only for DA objects that do have PM measurements.

Note that GJC does not provide errors on the PM, so I assumed an uncertainty of 2.5 mas/yr following Stauffer et al. (2010). One potential issue I encountered during my work is that in some cases I found a large discrepancy between the PM given in GJC and the PM given in SIMBAD. For consistency I have used the PM given in GJC, and assumed Tycho level uncertainties, in the work presented in the following sections. This was done to select candidate systems in a complete way. I then verified candidates at the end by checking on SIMBAD whether a more recent and more accurate PM was available.

In Figure 2.31, I have plotted the difference between the PM of the components of the associations identified X-matching DA with HMC as a function of their PM error. The PM errors are a combination of the uncertainties from both of the X-matched samples. The two dashed lines show the one sigma and 3 sigma limits. The candidates with uncertainties below 1 sigma are CPM systems. Those lying on

or above the 3 sigma line are non-CPM systems. For this X-match there is only 1 system that lies well above the 3 sigma line, and several in between the 1 and 3 sigma lines that I do not class as either CPM or non-CPM.

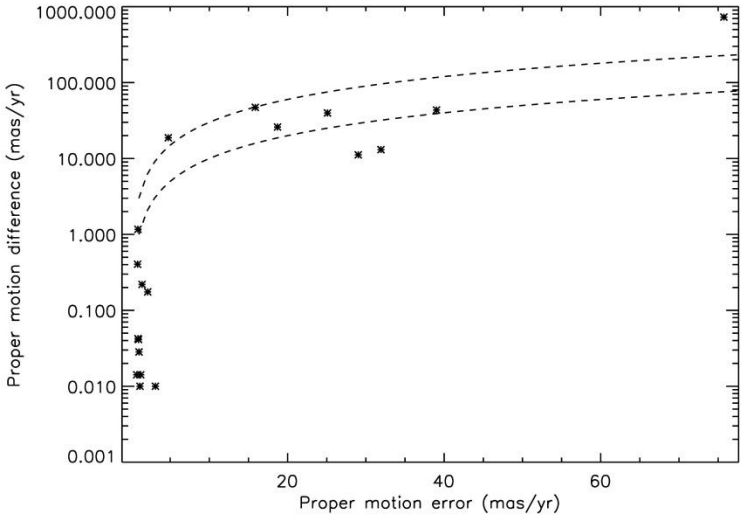

Figure 2.31: The difference between the PM of the components of the associations identifies X-matching DA with HMC as a function of their PM error. The two dashed lines show the 1 sigma and 3 sigma limits. All except two objects are within the 3 sigma limit.

In Figure 2.32 I show the separation histogram for the DA-HMC X-matching. CPM systems are plotted in black and non-CPM systems are plotted in red. CPM systems are in general more common at closer separation. This could be due in part to the dominant formation mechanism (that leads to wide binaries being rarer), as well as some selection biases that I will discuss in Chapter 3.
The non-CPM systems have larger separation, partly because some of them are simply random pairs of objects, but also because some of them are disintegrating multiple systems and so their separation is increasing.

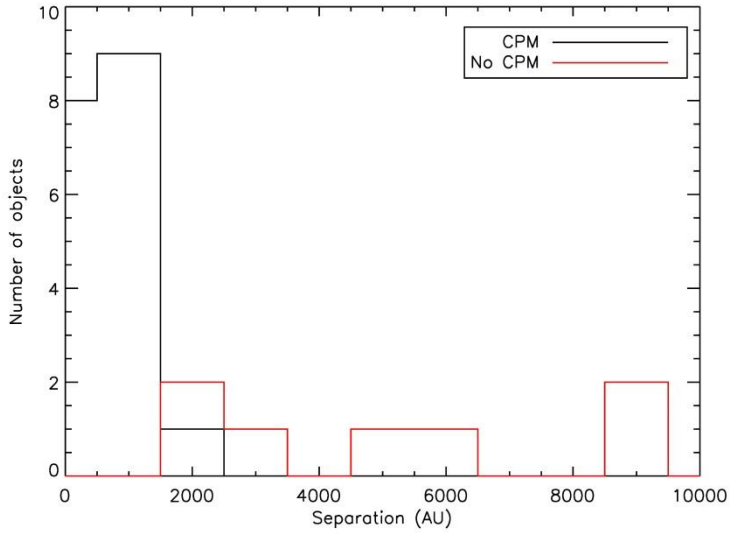

Figure 2.32: Separation histogram for the DA-HMC X-matching. CPM systems are plotted in black and non-CPM systems are plotted in red. CPM systems are common at shorter separation, non-CPM systems are more common at larger separation.

In Figure 2.33 I show the two components of the PM of the object in DA-HMC systems. UCDs are plotted in black while Hipparcos stars are plotted in red. This type of plot is very useful to identify CPM systems almost at first sight. This is because CPM objects will be next to each other in the plot. In the figure I have joined up the proper motions of associated objects with solid lines. These are visible in some cases, though in many cases the proper motions are so close together that only the red HMC object is seen because it has been over-plotted on top of the DA object.

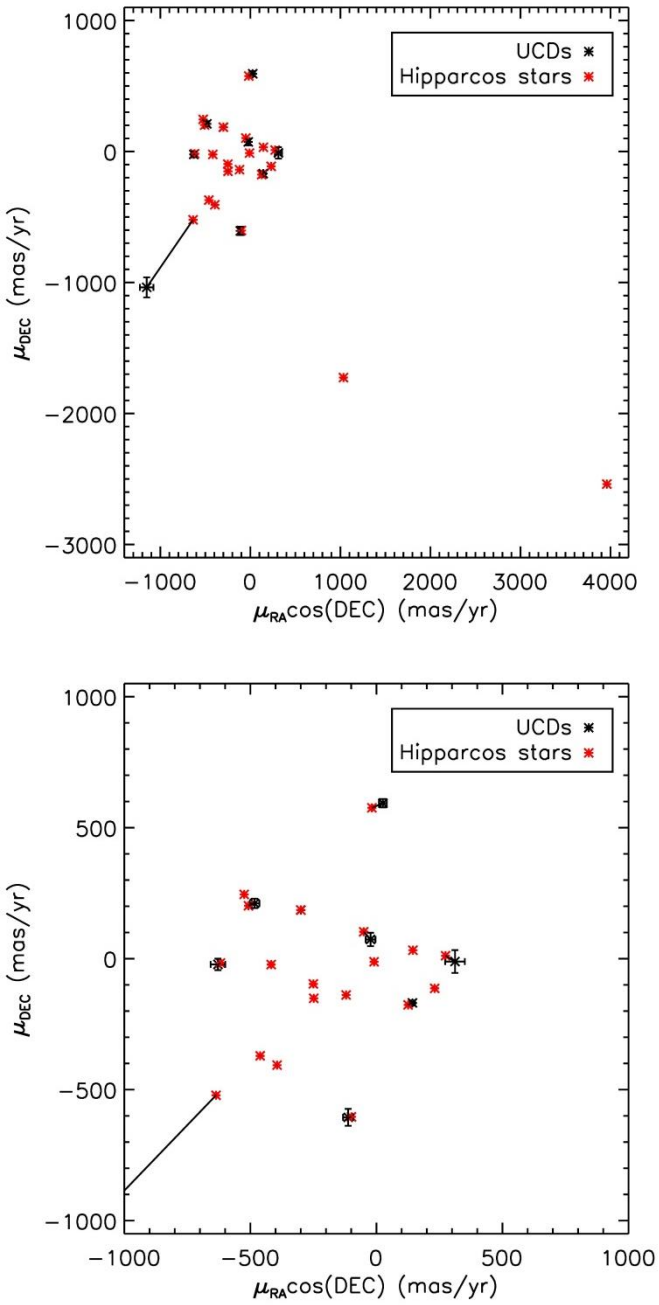

Figure 2.33: In the top plot, I show the full range of the two components of the PM of the objects in DA-HMC systems. BDs are plotted in black while Hipparcos stars are plotted in red. In the bottom plot, I show a zoom into the low PM region. CPM objects appear next to each other. The components of each system are connected with a black line. The error bars

represent the one sigma uncertainty, in many cases the error bars are not showing because the uncertainties are very small.

In Figure 2.34 I have plotted the difference in PMra on the x-axis and the difference in PMdec on the y-axis for each association. CPM systems are plotted in red and non-CPM systems are plotted in black. I can see that most of the CPM systems are concentrated around 0 while non-CPM systems are further away. There is one non-CPM system not far from 0, this is because the errors on the PM for that particular system are very small.

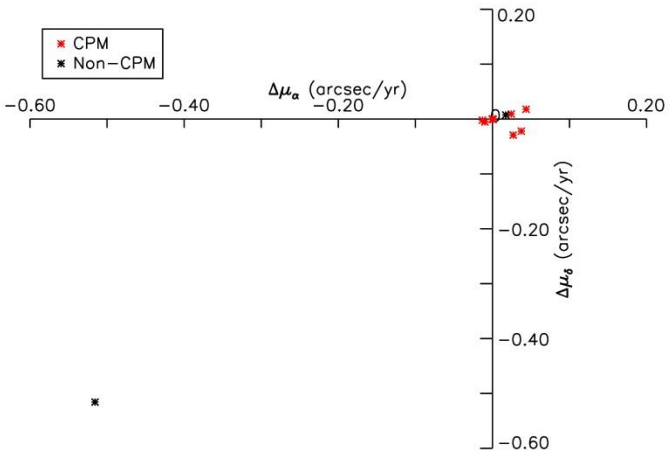

Figure 2.34: The difference in PMra on the x-axis and the difference in PMdec on the y-axis for each association. CPM systems are plotted in red and non-CPM systems are plotted in black. Non-CPM systems that are close to 0 have very small uncertainties.

In Figure 2.35, I have plotted the difference between the PM of the components of the associations identified X-matching DA with GJC, as a function of their PM error. The two dashed lines show the one sigma and 3 sigma limits. I can see that there are a lot of objects above the 3 sigma limit and these could be disintegrating associations. Only a few of them are within the 1 sigma limit.

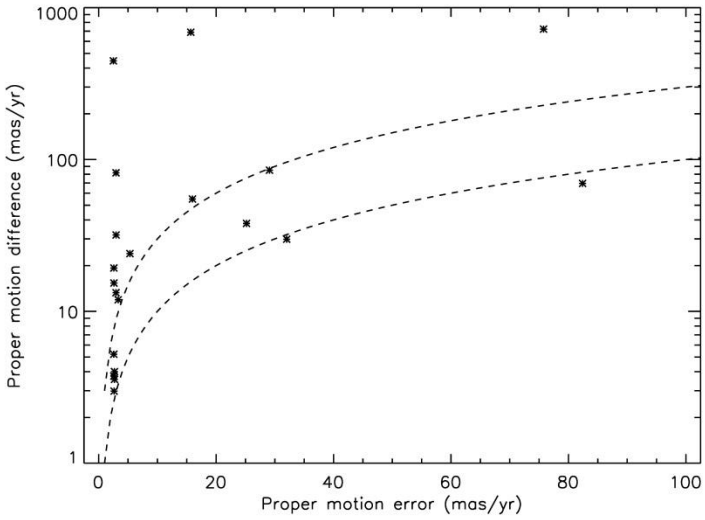

Figure 2.35: The difference between the PM of the components of the association identifies X-matching DA with GJC as a function of their PM error. The two dashed lines show the one sigma and 3 sigma limits. A lot of objects are above the 3 sigma limit hence are disintegrating candidates.

In Figure 2.36 I show the separation histogram for the DA-GJC X-matching. CPM systems are plotted in black and non-CPM systems are plotted in red. There are very few CPM systems, and they are all at very close separation. There are many candidate associations with non-CPM at close separation. This is very promising, since the chance of contamination is higher at wide separation and lower at close separation. So the numerous close separation candidates seem suggestive of a population of disintegrating systems.

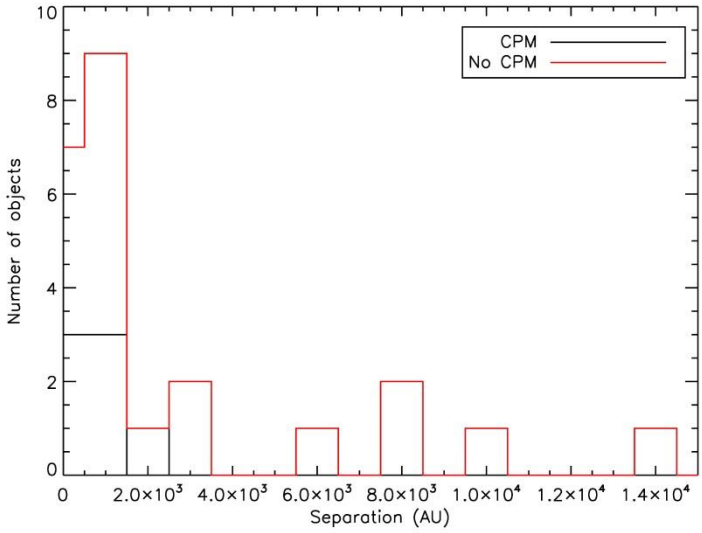

Figure 2.36: Separation histogram for the DA-GJC X-matching. CPM systems are plotted in black and non-CPM systems are plotted in red. CPM systems are common at shorter separation, and there are quite a few non-CPM systems at close separation too. This could be real disintegrating systems.

In Figure 2.37 I show the two components of the PM of the objects from the DA-GJC X-match. UCDs are plotted in black while Gliese stars are plotted in red. There are fewer CPM systems compare to the DA-HMC X-match. The majority of the systems have PM < 1000 mas/yr and there are only 5 objects with very large PM.

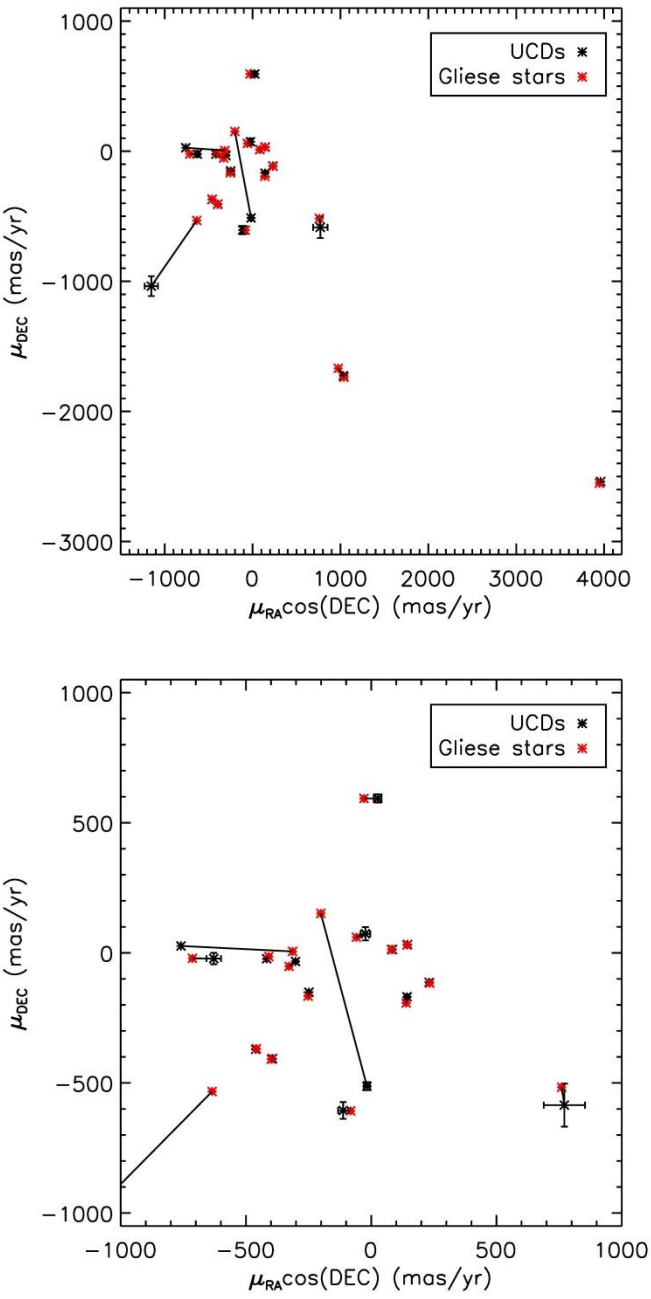

Figure 2.37: In the top plot, I show the full range of the two components of the PM of the object in DA-GJC systems. UCDs are plotted in black while Gliese stars are plotted in red. In the bottom plot, I show a zoom into the low PM region. The components of each system are connected with a black line. CPM objects appear next to each other and some of them are even superimposed. The error bars represent the one sigma uncertainties, in many cases the error bars are not showing because the uncertainties are very small.

In Figure 2.38 I have plotted the difference in PMra on the x-axis and the difference in PMdec on the y-axis for each association. CPM systems are plotted in red and non-CPM systems are plotted in

black. I can see that most of the CPM systems are concentrated around 0 while non-CPM systems are further away.

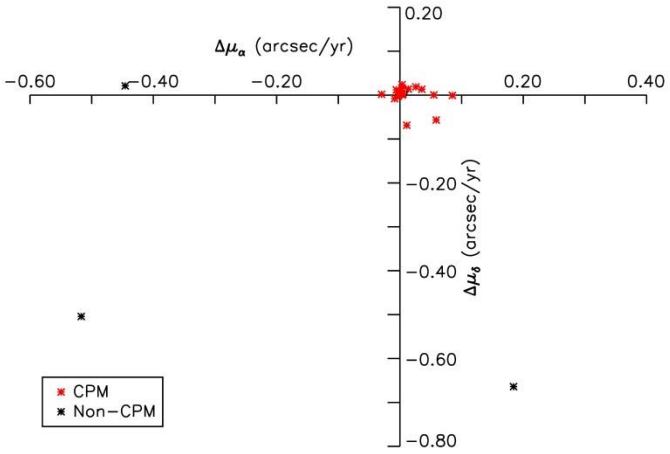

Figure 2.38: The difference in PMra on the x-axis and the difference in PMdec on the y-axis for each association. CPM systems are plotted in red and non-CPM systems are plotted in black.

In Figure 2.39, I have plotted the difference between the PM of the components of the associations identified from the X-match between HMC and HMC, as a function of their PM errors. The two dashed lines show the one sigma and 3 sigma limits. Components of candidate binaries are plotted in black, components of candidate triple systems are plotted in red while components of candidate quintuple systems are plotted in blue. I can see that there are a lot of objects above the 3 sigma limit and these are non-CPM systems that may be disintegrating multiple candidates. There are only 10 associations whose PM's are within 1 sigma.

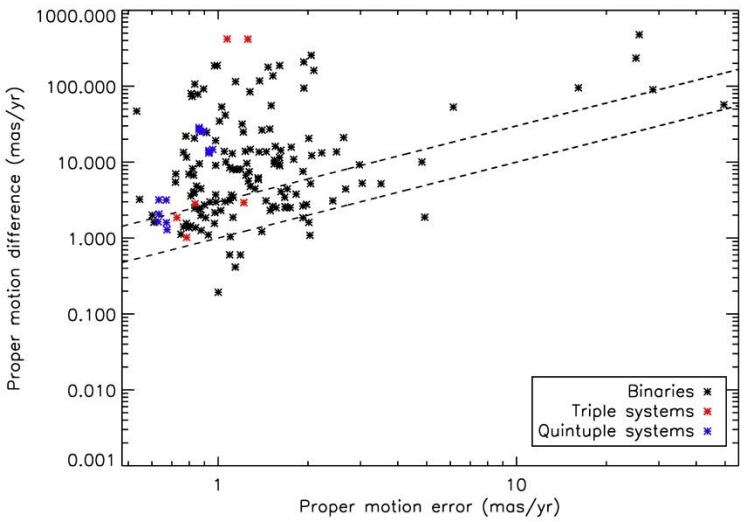

Figure 2.39: The difference between the PM of the components of the associations identifies X-matching HMC with HMC as a function of their PM error. The two dashed lines show the one sigma and 3 sigma limits. Components of candidate binaries are plotted in black, components of candidate triple systems are plotted in red while components of candidate quintuple systems are plotted in blue. A lot of objects are above the 3 sigma limit, hence are disintegrating candidates.

In Figure 2.40 I show the separation histogram for the HMC-HMC X-matching. CPM systems are plotted in black and non-CPM systems are plotted in red. There are very few CPM systems, and most of them are at close separation. The figure shows that there are a lot of non-CPM systems, and the majority of them are at close separation. As mentioned before this is very promising because they are likely to be real disintegrating multiple systems, since with such close separation they are less likely to be contaminants.

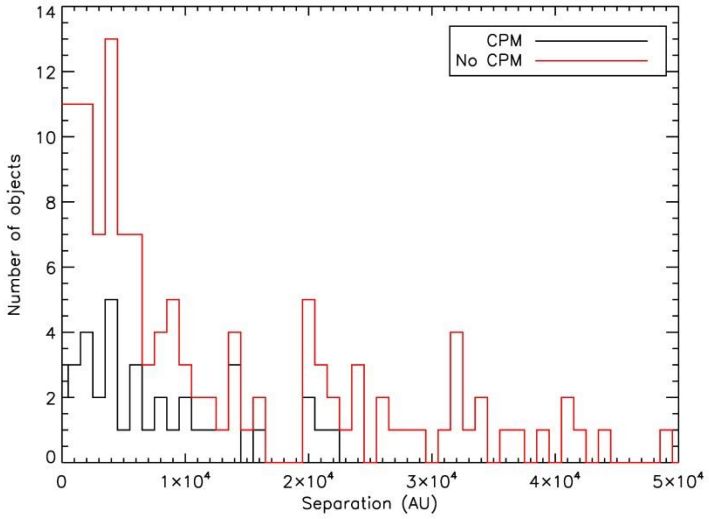

Figure 2.40: Separation histogram for the HMC-HMC X-match. CPM systems are plotted in black and non-CPM systems are plotted in red. There are a few CPM systems, especially at short separation, and there are quite a few non-CPM systems extending all the way to 50 kAU. These are likely to be real disintegrating systems.

In Figure 2.41 I show the two components of the PM of the objects in HMC-HMC systems. The two components of groups of 2 are plotted in black and red respectively, associations that come from higher level groupings (triples and quintuples) are shown in green and blue respectively. In this figure, I did not join CPM systems with a line between them because otherwise the plot would become unreadable. It is easy to identify by eye the CPM systems and I can see that 4 of them have very large PM. The majority of the systems have lower PM, normally below 1000 mas/yr. The triples and quintuples belong to this population.

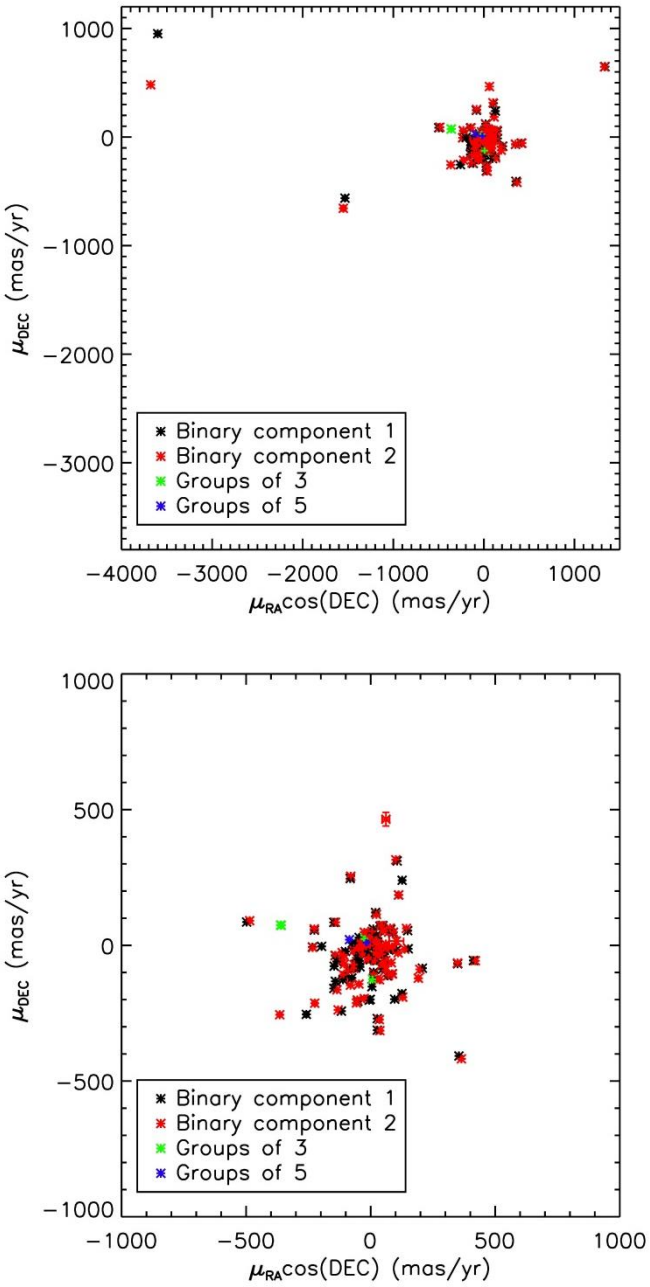

Figure 2.41: In the top plot, I show the full range of the two components of the PM of the objects in HMC-HMC systems. The two components of groups of 2 are plotted in black and red respectively, objects in groups of 3 are plotted in green and objects in groups of 5 are plotted in blue. In the bottom plot, I show a zoom into the low PM region. CPM objects appear next to each other and some of them are even superimposed. The error bars represent the one sigma uncertainties, in many cases the error bars are not showing because the uncertainties are very small.

In Figure 2.42 I have plotted the difference in PMra on the x-axis and the difference in PMdec on the y-axis for each association. CPM systems are plotted in red and non-CPM systems are plotted in black. I can see that most of the CPM systems are concentrated around 0 while non-CPM systems are further away. There are non-CPM systems not far from 0, this is because the errors on the PM for those particular systems are very small. On the other hand, there is one CPM system far from 0, this is because the errors on the PM for that particular system are very large.

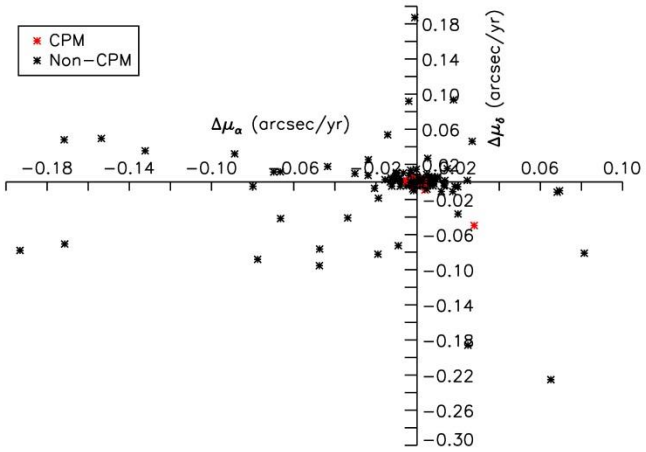

Figure 2.42: The difference in PMra on the x-axis and the difference in PMdec on the y-axis for each association. CPM systems are plotted in red and non-CPM systems are plotted in black. Non-CPM systems that are close to 0 have small uncertainties. The CPM system that is far from 0 has large uncertainties.

In Figure 2.43, I have plotted the difference between the PM of the components of the associations identified X-matching GJC with GJC as a function of their PM error. The two dashed lines show the one sigma and 3 sigma limits. Components of candidate binaries are plotted in black and components of candidate triple systems are plotted in red. The objects form a vertical line because I always assume a constant error of 2.5 mas/yr for each object, so the combined (in quadrature) uncertainty is $2.5 * \sqrt{2}$ (see above). Once again there are a lot of objects above the 3 sigma limit and these could be disintegrating associations. Only a few of them are within the 1 sigma limit.

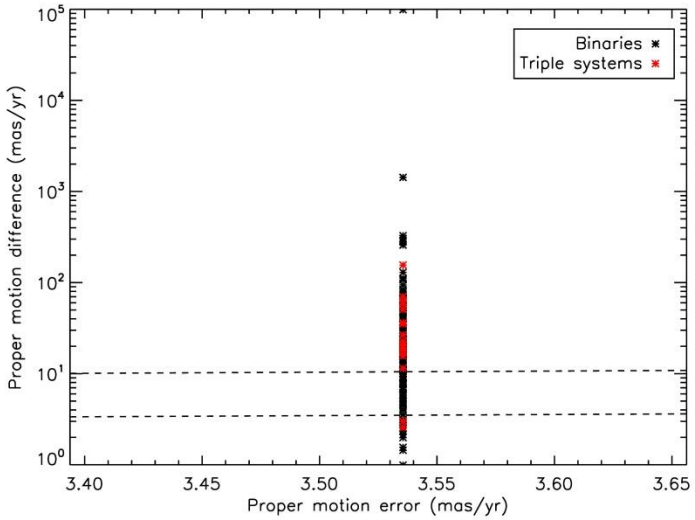

Figure 2.43: The difference between the PM of the components of the associations identified X-matching GJC with GJC as a function of their PM error. The two dashed lines show the one sigma and 3 sigma limits. Components of candidate binaries are plotted in black and components of candidate triple systems are plotted in red. A lot of objects are above the 3 sigma

limit hence are disintegrating candidates. The objects form a vertical line because of my assumption of 2.5 mas/yr PM errors.

In Figure 2.44 I show the separation histogram for the GJC-GJC X-match. CPM systems are plotted in black and non-CPM systems are plotted in red. The distribution of CPM and non-CPM systems are very similar. In both cases the majority of the systems have close separation. The fact that there are lots of non-CPM systems at close separation may be due in part to my initial assumption that all errors are 2.5 mas/yr. Some of these non-CPM systems were re-assigned as CPM systems in my final candidate checking stage. Interestingly the distribution of CPM systems has a secondary peak at 6 kAU.

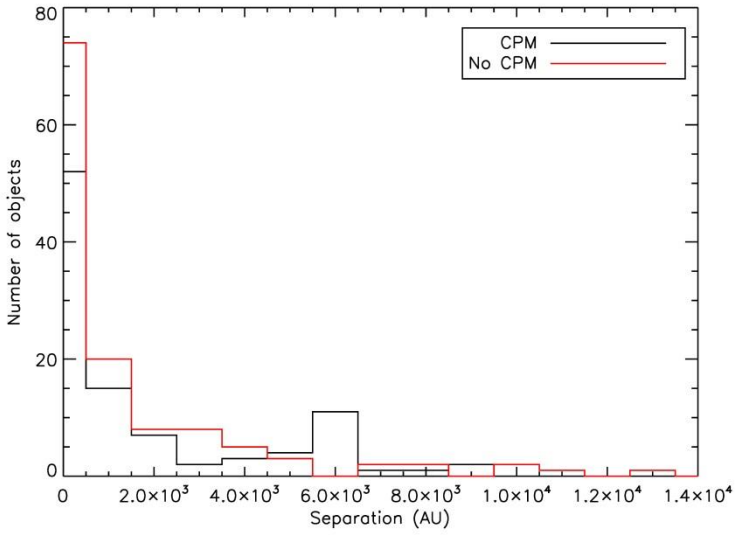

Figure 2.44: Separation histogram for the GJC-GJC X-match. CPM systems are plotted in black and non-CPM systems are plotted in red. The distribution of CPM and non-CPM systems are very similar. In both cases the majority of the systems have close separation.

In Figure 2.45 I show the two components of the PM of the object in GJC-GJC systems. The two components of groups of 2 are plotted in black and red respectively, objects in groups of 3 are plotted in green while objects in groups of 4 are plotted in light blue and objects in groups of 5 are plotted in blue. In this figure, I did not join CPM systems with a line between them because otherwise the plot would become unreadable. There is a higher number of higher PM objects than in the HMC-HMC systems. This is because the GJC contains only very nearby objects (within 25pc) and nearby objects have higher PM. The figure shows clearly a few CPM triple systems (e.g. the one at 1000, 0 or the one at -2500, -3500).

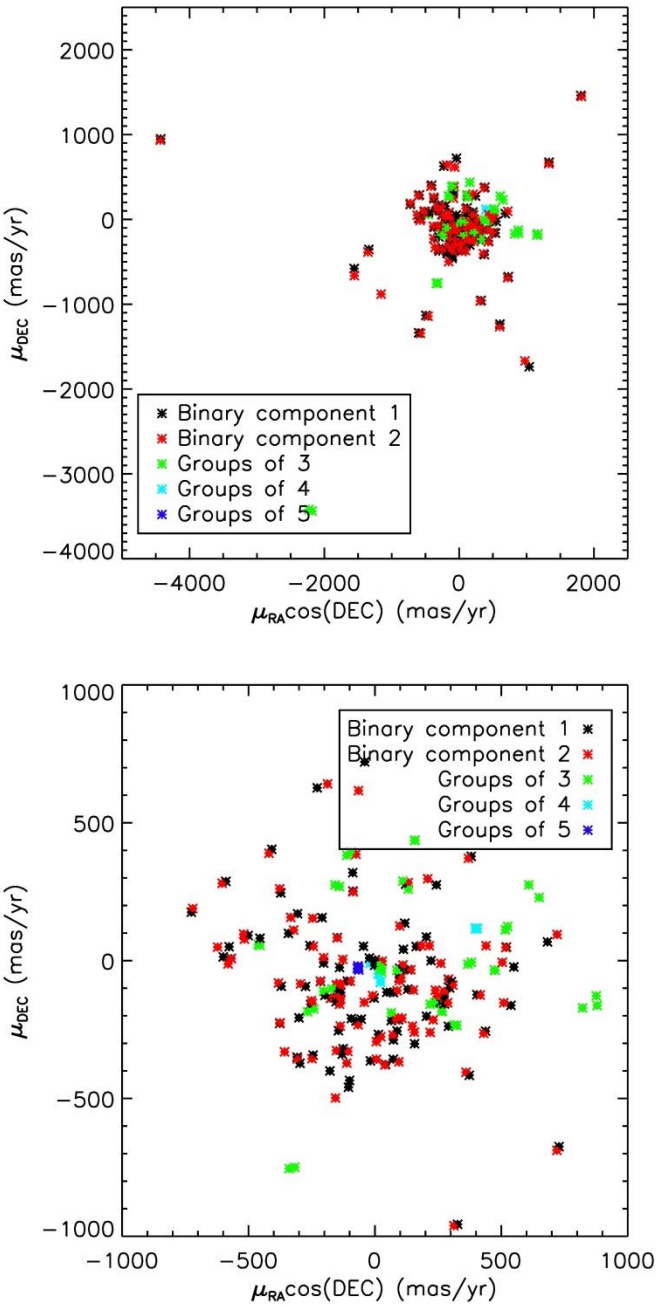

Figure 2.45: In the top plot, I show the full range of the two components of the PM of the objects in GJC-GJC systems. The two components of groups of 2 are plotted in black and red respectively, objects in groups of 3 are plotted in green while objects in groups of 4 are plotted in light blue and objects in groups of 5 are plotted in blue. In the bottom plot, I show a zoom into the low PM region. CPM objects appear next to each other and some of them are even superimposed. The error bars represent the one sigma uncertainties, in many cases the error bars are not showing because the uncertainties are very small.

In Figure 2.46 I have plotted the difference in PMra on the x-axis and the difference in PMdec on the y-axis for each association. CPM systems are plotted in red and non-CPM systems are plotted in black. I can see that most of the CPM systems are concentrated around 0 while non-CPM systems are further away. There are some non-CPM systems not far from 0, this is because the errors on the PM for those particular systems are very small.

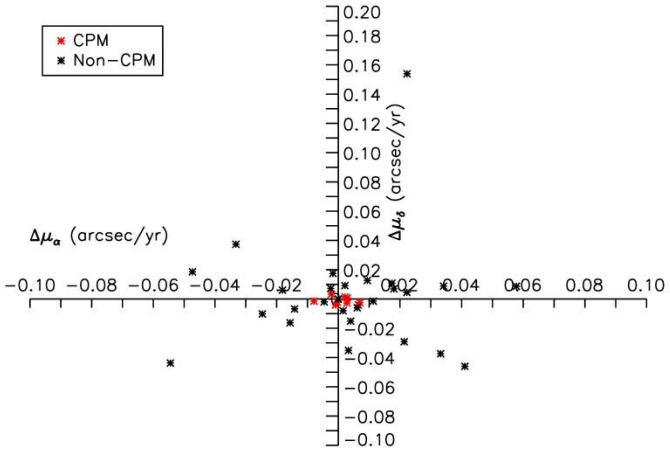

Figure 2.46: The difference in PMra on the x-axis and the difference in PMdec on the y-axis for each association. CPM systems are plotted in red and non-CPM systems are plotted in black. Non-CPM systems that are closer to 0 have very small uncertainties.

In Figure 2.47 I have plotted the difference between the PM of the components of the associations identifies X-matching HMC with GJC as a function of their PM error. The two dashed lines show the one sigma and 3 sigma limits. Components of candidate associations with 2, 3, 4, 5 and 6 components are plotted in black, red, green, blue and yellow respectively. Similar to the previous cases, the majority of objects are above the 3 sigma limit and these could be disintegrating associations. Only a few of them are within the 1 sigma limit. Once again, the non-CPM associations include objects where the PM uncertainties have been under-estimated (the 2.5 mas/yr assumption), and many of these associations were removed when the SIMBAD proper motions were examined in the final checking stage.

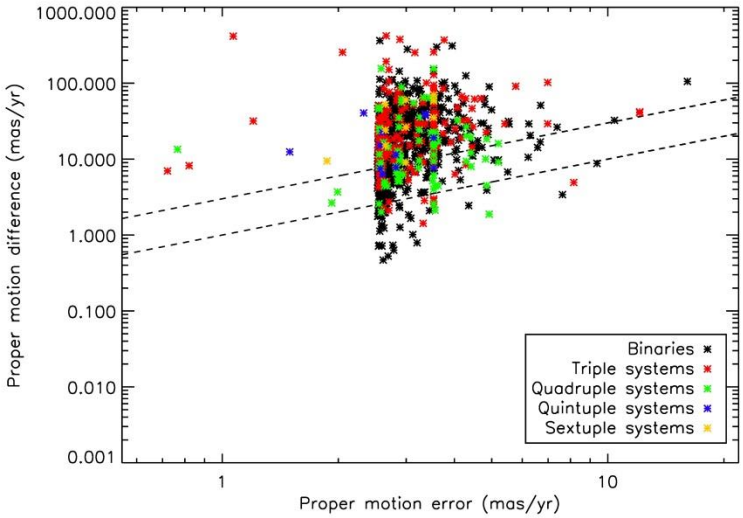

Figure 2.47: The difference between the PM of the components of the associations identifies X-matching HMC with GJC as a function of their PM error. The two dashed lines show the one sigma and 3 sigma limits. Components of candidate binaries are plotted in black, components of candidate triple systems are plotted in red, components of candidate quadruple systems are plotted in green, components of candidate quintuple systems are plotted in blue and components of candidate sextuple systems are plotted in yellow. A lot of objects are above the 3 sigma limit hence are disintegrating candidates.

In Figure 2.48 I show the separation histogram for the HMC-GJC X-match. CPM systems are plotted in black and non-CPM systems are plotted in red. The distribution of CPM and non-CPM systems are again very similar. In both cases the majority of the systems have close separation however it can be seen that the number of non-CPM systems decreases smoothly towards large separations.

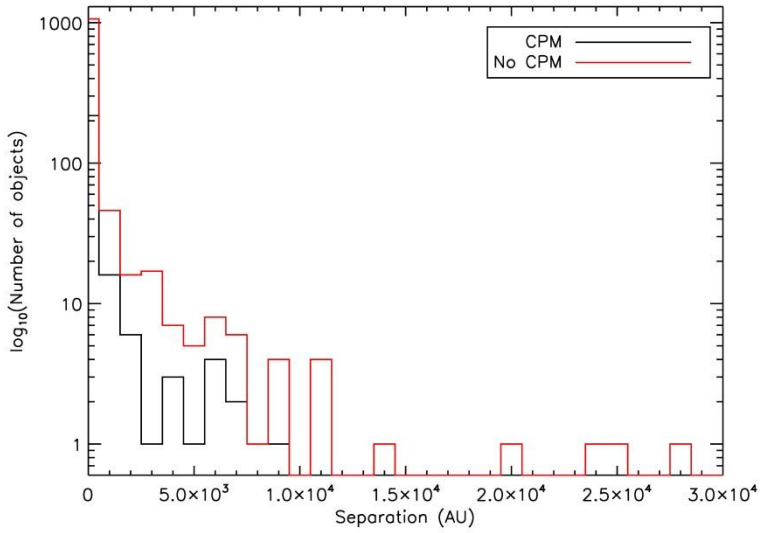

Figure 2.48: Separation histogram for the HMC-GJC X-match. CPM systems are plotted in black and non-CPM systems are plotted in red. The distribution of CPM and non-CPM systems are very similar.

In Figure 2.49 I show the two components of the PM of the object in HMC-GJC systems. The Gliese stars are plotted in black and the Hipparcos stars are plotted in red. In this figure, I did not join CPM systems with a line between them because otherwise the plot would become unreadable. There are quite a few high PM objects because, as explained before, GJC contains mostly very nearby stars. Most of the high PM objects are in CPM systems. Similarly to the pervious plot the majority of the population have low PM, i.e. between -1000 and 1000 mas/yr.

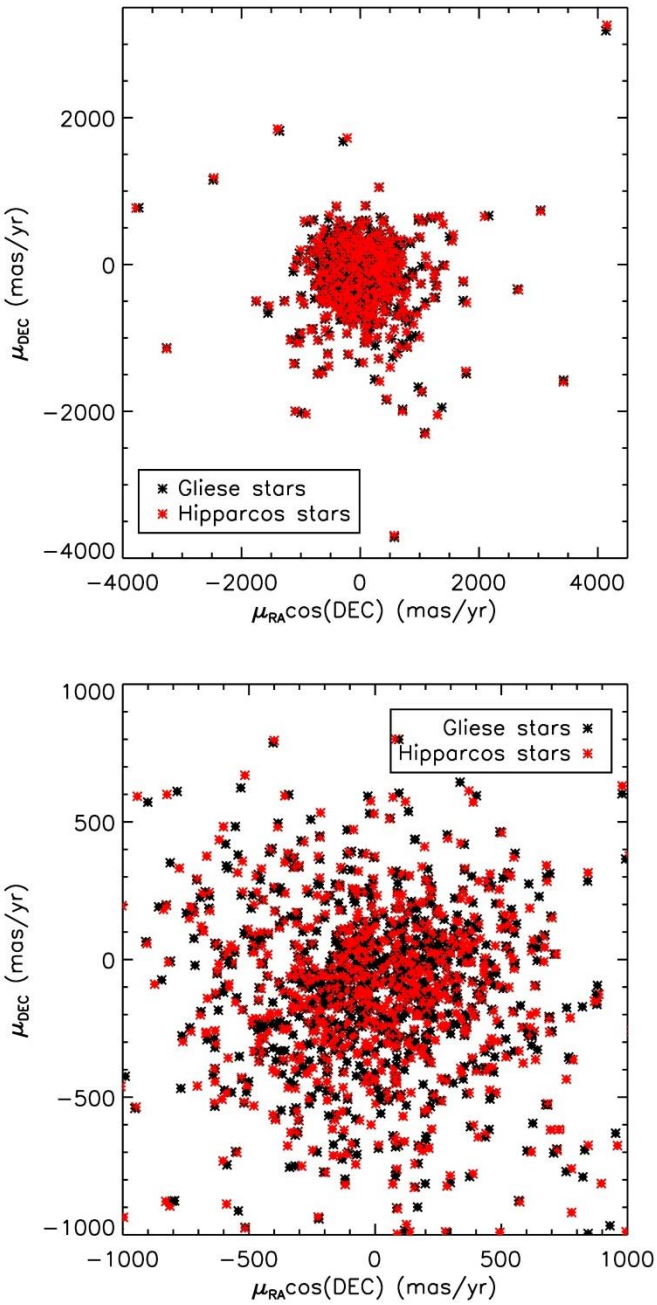

Figure 2.49: In the top plot, I show the full range of the two components of the PM of the objects in HMC-GJC systems. The Gliese stars are plotted in black and the Hipparcos stars are plotted in red. In the bottom plot, I show a zoom into the low PM region. CPM objects appear next to each other and some of them are even superimposed. The error bars represent the one sigma uncertainties, in many cases the error bars are not showing because the uncertainties are very small.

In Figure 2.50 I have plotted the difference in PMra on the x-axis and the difference in PMdec on the y-axis for each association. CPM systems are plotted in red and non-CPM systems are plotted in black. It can be seen that most of the CPM systems are concentrated around 0 while non-CPM systems are further away. There are some non-CPM systems not far from 0, this is because the errors on the PM for those particular systems are very small. Some of the non-CPM associations have their uncertainties underestimated, so were re-identified as CPM during the final checking stage.

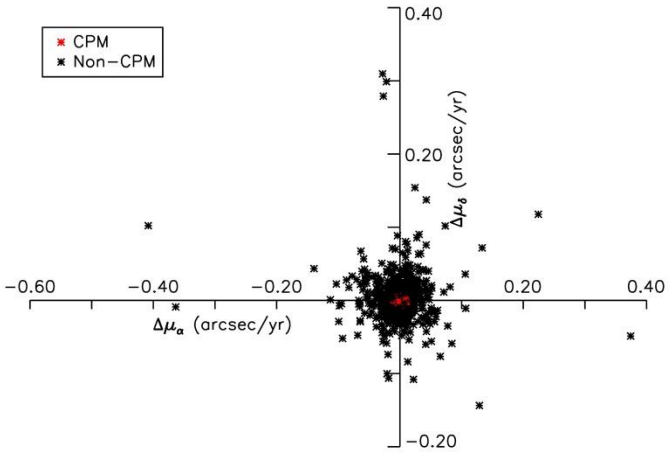

Figure 2.50: I have plotted the difference in PMra on the x-axis and the difference in PMdec on the y-axis for each association. CPM systems are plotted in red and non-CPM systems are plotted in black. Non-CPM systems that are close to 0 have very small uncertainties.

2.6 Confirming disintegrating system candidates through relative motion

As a final assessment for disintegrating multiple candidates I combined proper motions with separation measurements, and determined if associated objects are moving away from each other as I expect for disintegrating systems. The separation between associated objects was calculated as a function of time (t) using equation 14. Note that in equation 14 the time (t) can be negative and positive, reflecting the previous and future separation of the association.

$$Sep(t) = \sqrt{\left[\left(\alpha_1 + \mu_{\alpha_1} * t\right) - \left(\alpha_2 + \mu_{\alpha_2} * t\right)\right]^2 * \cos(\delta_1)^2 + \left[\left(\delta_1 + \mu_{\delta_1} * t\right) - \left(\delta_2 + \mu_{\delta_2} * t\right)\right]^2} \quad (14)$$

This equation does not account for any gravitational attraction, as it assumes straight line motion for associated objects. This is an approximation, though should be reasonable for most of my candidates because at wide separation the effects of gravity should be small. However, I expect this approximation to lead to some inaccuracies in the previous/future forecasts of the time of closest approach. Therefore I expect some level of scatter in the times of closest approach for the components of higher order systems. This is because in higher order systems the gravitational interaction between the components is more complex and the uncertainties add up causing larger scatter.

Note that I have used Monte Carlo simulations as part of the calculation of the uncertainty on $Sep(t)$. For each system, the Monte Carlo simulation generates 1000 random numbers from a Gaussian distribution centred on the PM of its components and with width equivalent to the PM error of each component. I calculated $Sep(t)$ for each of the 1000 generated PMs. The uncertainty

on $Sep(t)$ is the standard deviation of all the calculated separations, or in other words, the area covered by the 1000 possible paths.

I then selected as disintegrating candidates only associations where the epoch of closest approach between the objects was in the past, i.e. the objects were currently moving away from each other (see Figure 3.7). In Figure 2.51 I show an association where the closest approach is in the future, and therefore this association is not disintegrating. For the intermediate cases, where some objects have the closest approach in the past and some in the future, I interpreted by eye the plot and decided case by case if the system is disintegrating or not.

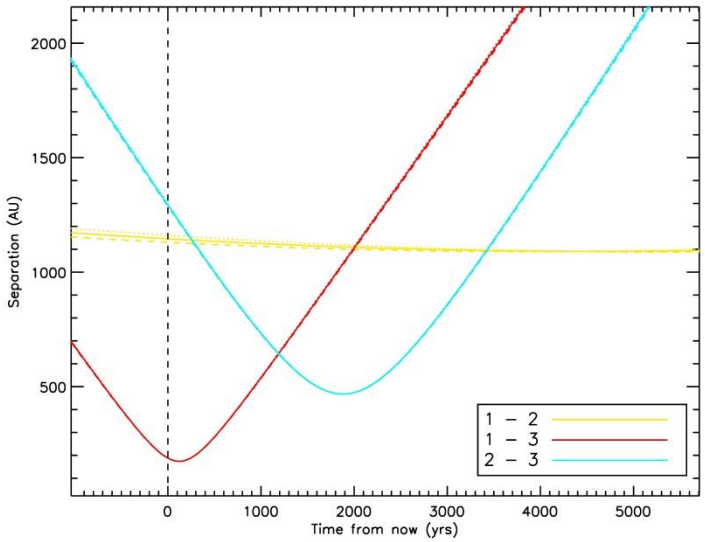

Figure 2.51: The separation between the objects in a non-CPM association as a function of time. The yellow line is the separation between object number 1 and object number 2, the red line is the separation between object number 1 and object number 3 while the blue line is the separation between object number 2 and object number 3. The objects reach minimum separation in the future so the system is not disintegrating.

2.6.1 New binaries and multiple systems identified with CPM

As part of my X-matching I have also identified several CPM systems. Most of these are already confirmed as binaries or multiples. I have used SIMBAD and the Besançon Double and Multiple Star Database to identify systems that were previously confirmed. However some of them are not reported as binaries or multiples in the literature. I discuss them in the following subsections.

2.6.1.1 Binaries

System 1

A new binary I found X-matching HMC and GJC is formed by BD+57 1274, a M0 type star (Vyssotsky 1943), and SDSS J103143.31+570644.2, a M2 star (West et al. 2011). The first object is at a distance of 17.49 ± 0.40 pc (from HMC) and second objects is at a distance of 17.54 ± 2.46 pc (from GJC).

The two components of the PM of the M0 are PMra= -66.52 ± 1.05 mas/yr and PMdec= 172.39 ± 0.78 mas/yr (PM values are from HMC), while the two components of the PM of the M2 are PMra= -

78.20 ± 2.50 mas/yr and PMdec= 205.61 ± 2.50 mas/yr (PM value are from GJC). The PM of the two stars therefore agrees at the 1 sigma level. This can be seen very well in Figure 2.52 where I show the PM of the two objects. The M2 is plotted in yellow and the M0 is plotted in red.

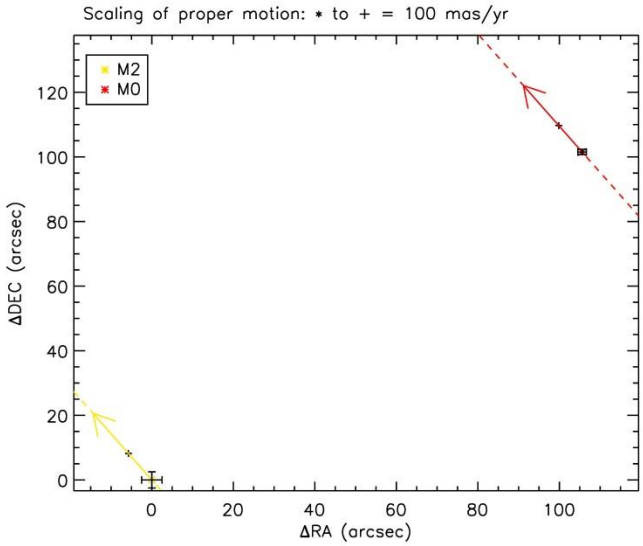

Figure 2.52: The proper motion of the stars. The M2 is plotted in yellow and the M0 is plotted in red. The figure shows that the two objects share CPM and therefore are very likely to be a genuine binary system. The errors on the two components of the PMs are plotted at the beginning of each arrow. The dashed lines are plotted to ease the comparison between the PMs directions.

2.6.1.2 Triple systems

System 1

As well as CPM binaries, I have also identified CPM triple and even higher order groups. All of them were previously confirmed except the ones that I am presenting now. The new triple system I found X-matching HMC and HMC is formed by the V* LX Com, a K1 variable of BY Dra type star (Montes et al. 2001), and BD+26 2401, a K5 spectroscopic binary (Yoss & Griffin 1997). The first object is at a distance of 37.68 ± 2.06 pc and second objects are at a distance of 39.78 ± 2.75 pc (both distances are from Hipparcos).

The two components of the PM of the K1 are PMra= -142.59 ± 1.24 mas/yr and PMdec= -37.49 ± 1.19 mas/yr, while the two components of the PM of the K5 spectroscopic binary are PMra= -141.09 ± 1.60 mas/yr and PMdec= -36.92 ± 1.42 mas/yr (both PM values are from Hipparcos). The PM of the two members of the system therefore agrees at the 1 sigma level. This can be seen very well in Figure 2.53 where I show the PM of the system. The K1 is plotted in yellow and the K5 spectroscopic binary is plotted in red.

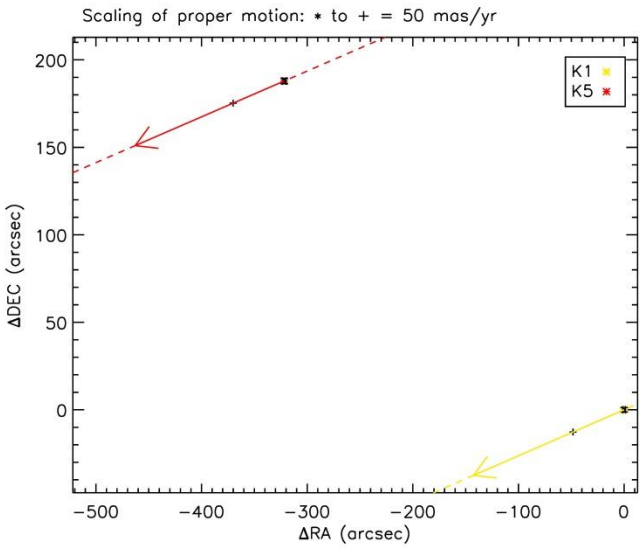

Figure 2.53: The proper motion of the stars. The K1 is plotted in yellow and the K5 is plotted in red. The figure shows that the two objects share a CPM is very likely to be a genuine binary system. The error on the two components of the PMs is plotted at the beginning of each arrow. The dashed lines are plotted to ease the comparison between the PMs direction.

System 2

The new triple system I found X-matching GJC and GJC is formed by a previously confirmed binary and a single star. The two components of the binary system are BD+10 1857, a M1 star (Joy & Abt 1974), and BD+10 1857C, a M3.5 star (Bidelman 1985). The third star is 2MASS J08425064+0934465, a M4 star (West et al. 2011). The first object is at a distance of 14.97 ± 0.51 pc, the second object is at a distance of 14.93 ± 0.87 pc and the third object is at a distance of 14.97 ± 0.51 pc (all distances are from GJC).

The two components of the PM of the M1 are PMra= 203.49 ± 2.50 mas/yr and PMdec= -641.50 ± 2.50 mas/yr, the two components of the PM of the M3.5 are PMra= 223.84 ± 2.50 mas/yr and PMdec= -616.15 ± 2.50 mas/yr, while the two components of the PM of the M4 are PMra= 203.49 ± 2.50 mas/yr and PMdec= -641.50 ± 2.50 mas/yr (all PM values are from GJC). The PM of the three stars therefore agrees at the 1 sigma level. This can be seen very well in Figure 2.54 where I show the PM of the three objects. The M1 is plotted in yellow, the M3.5 is plotted in red and the M4 is plotted in light blue. The M1 and M3.5 are superimposed in the plot as they share the same co-ordinates and PM. The M4 also shares the same PM as the other two, hence the arrows align perfectly. Note that the PM listed in SIMBAD for two of the three objects is significantly different from the one in GJC. As a consequence if I adopt the SIMBAD PM in my calculation the difference between the PM of the objects is almost 3 sigma.

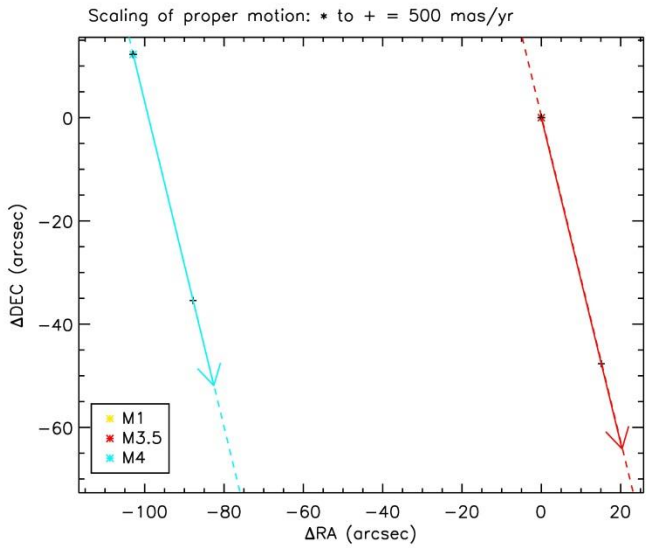

Figure 2.54: The proper motion of the stars. The M1 is plotted in yellow, the M3.5 is plotted in red and the M4 is plotted in light blue. The M1 and M3.5 are superimposed in the plot as they share the same co-ordinates and PM. The errors on the two components of the PMs are plotted at the beginning of each arrow. The dashed lines are plotted to ease the comparison between the PMs directions.

2.7 Final disintegrating multiple candidates

Table 2.6 summarizes my results. Overall I have identified 1 disintegrating quadruple candidate containing a UCD component. Additionally I have found a new binary candidate and 2 new triple candidates. Furthermore, I have also found another 3 possible disintegrating quadruple associations. Note that the total number of CPM and non-CPM systems is the result of the initial X-matches, therefore includes duplicate objects. These duplicate objects are from the GJC itself, i.e. there are repeated objects in the GJC. The robustness of the method is proven by the fact that I have been able to identify many previously confirmed binaries, multiples, benchmark systems and cluster objects. These systems have been removed and the results presented here represent new discoveries. As mentioned above all of the candidates have been inspected closely using SIMBAD and the Besancon Double and Multiple Star Database, therefore they are not affected by the duplicates.

Table 2.6: This table presents the summary of the results from all X-matches.

X-match	Number of components	CPM	System candidates	non-CPM	Disintegrating candidates
DA-HMC	2	14	0	8	0
	3	3	0	0	0
DA-HMC-HMC	-	0	0	0	0
DA-HMC-GJC	-	0	0	3	0
DA-GJC	2	2	0	12	0
	3	4	0	1	0
DA-GJC-GJC	-	0	0	3	1
DA-GJC-HMC	-	0	0	10	0
HMC-HMC	2	10	2	134	0
	3	1	1	3	0
	4	0	0	1	1
GJC-GJC	2	10	0	464	0
	3	32	1	0	0
	4	3	0	1	1
	5	1	0	0	0
HMC-GJC	2	11	1	683	0
	3	86	0	52	0
	4	0	0	23	1
	5	0	0	3	0

Note: In column 1 I show the catalogue that were X-matched, in column 2 I show the number of components of the systems identified, in column 3 I show the number of CPM associations found, in column 4 I show the number of new CPM systems found, in column 5 I show the non-CPM associations found, finally in column 6 I show the number of disintegrating candidates found. The total number of CPM and non-CPM systems represents the result from the initial X-matches, i.e. they include duplicate objects.

I will now in Chapter 3 describe in further details the various types of interesting associations that I have found.

Chapter 3

3. Discussion and individual candidate systems

3.1 Separation distribution of associations

The separation distribution is an important property of the associations that I have identified. This was discussed briefly in Chapter 2 and now I analyze it in more detail. For some of my X-matched samples there is a relatively large number of non-CPM associations at closer separation. This is likely due to 3 reasons. The first reason is that the 10 arcminute maximum angular separation cuts out very wide associations (> 50 kAU) when D < 84 pc, and only keeps very close associations at shorter distance. This will affect different samples in different ways - samples that are dominated by fairly nearby objects (like DA and GJC in particular) will be more affected.

This effect is demonstrated in Figure 3.1 to Figure 3.5, showing the separation in AU and the distance (in pc) of the associations from the various X-matches. The dashed line shows the 10 arcminute angular separation limit. The plots show that the 10 arcminutes limit does not select some wide associations at close distance, thus leading to an apparent bias favouring systems with small separation. This is visible in particular in Figure 3.1, 3.2, and 3.4.

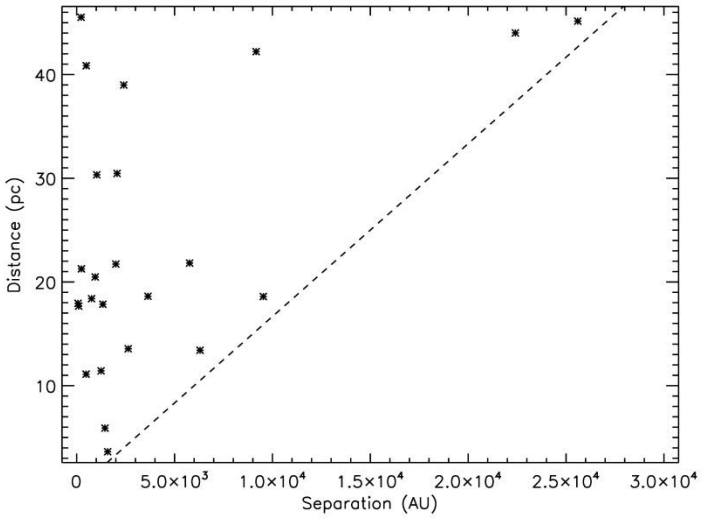

Figure 3.1: Separation in AU against the distance of the associations from the DA-HMC X-match. The dashed line shows the 10 arcminute angular separation limit. There is a wide and homogeneous range of separations.

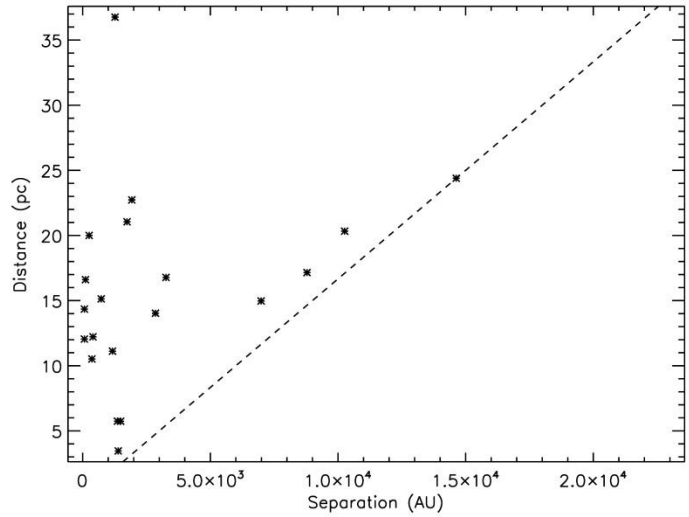

Figure 3.2: Separation in AU against the distance of the associations from the DA-GJC X-match. The dashed line shows the 10 arcminute angular separation limit. There is a wide and homogeneous range of separations.

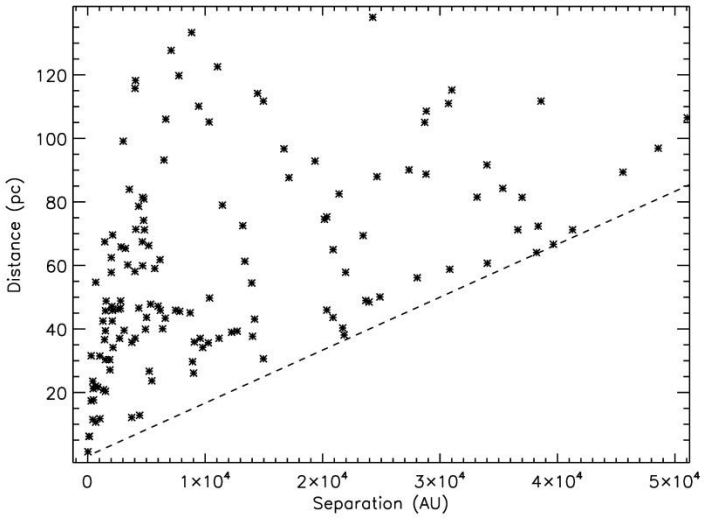

Figure 3.3: Separation in AU against the distance of the associations from the HMC-HMC X-match. The dashed line shows the 10 arcminute angular separation limit. There is a wide and homogeneous range of separations.

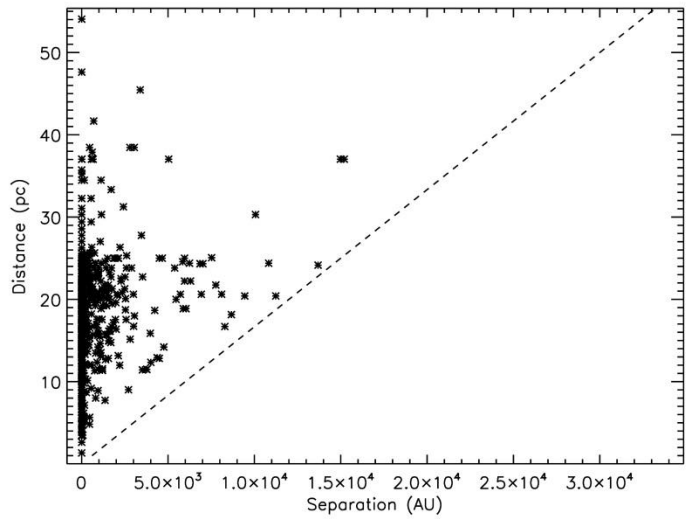

Figure 3.4: Separation in AU against the distance of the associations from the GJC-GJC X-match. The dashed line shows the 10 arcminute angular separation limit. Most of the associations have very close separations.

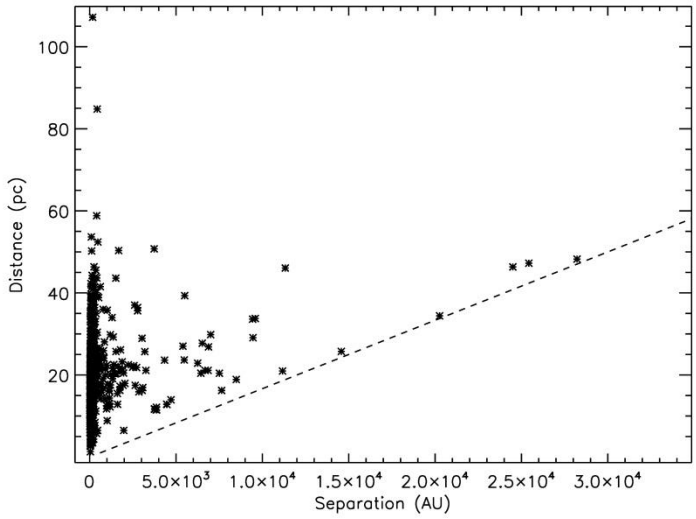

Figure 3.5: Separation in AU against the distance of the associations from the HMC-GJC X-match. The dashed line shows the 10 arcminute angular separation limit. Most of the associations have very close separations because of the GJC components.

The second reason is that there are some non-CPM systems that are fairly marginal, i.e. the difference between the PM of the components is only slightly above my 3 sigma limit. So some of these will likely be CPM binaries and multiples but with measured PMs that have scattered a bit due to measurement uncertainty. I can see that this might be the case for some objects in Figures 2.31, 2.35, 2.39, 2.43 and 2.47.

The third reason is the assumption of PM uncertainty =2.5 mas/yr for all GJC objects. Although this assumption is dealt with in my final selection of candidates, it remains as a bias in the selection of CPM and non-CPM systems. This leads to the selection of some non-CPM systems that are actually CPM multiples (which generally have closer separation).

Moreover, my separation histograms in Chapter 2 for non-CPM systems show that my results contain a significant fraction of contamination. This is due to duplicate objects, misclassified CPM objects, and line-of-sight associations with large uncertainty on their distance. These contaminants are removed in the last step of my analysis, and the final result is a small number of candidate disintegrating systems.

3.2 Individual systems

In this section I describe all of the disintegrating candidates. They were selected as having a common distance (within uncertainties), my non-CPM criteria, and the requirement that components should be moving apart from each other over time.

System 1

From the X-match between DA and GJC, this association is made of 4 stars from two binaries. For the first binary, the star is GJ 570 A, a variable of BY Dra K4 type star (Cowley et al. 1967), at a distance of 5.74 $\pm$ 0.20 pc (from GJC). The UCD is GJ 570 D, a T7.5 type BD (Burgasser et al. 2000b), at a distance of 5.84 $\pm$ 0.03 pc (the distance is from Dwarf Archive). The second multiple system is a spectroscopic binary, the components are GJ 570 B and GJ 570 C, both type M1.5 (Gray et al. 2006), at a distance of 5.74 $\pm$ 0.20 pc (from GJC).

The proper motion of the stars is shown in Figure 3.6. The Gliese star is plotted in yellow and the BD is plotted in red. I can see that the two PM align almost perfectly because the PM are very large while the difference between them is very small so it is harder to see the non-alignment. Nonetheless the difference in PM is greater than 3 sigma. I note here that the system is consider to be CPM in Burgasser et al. (2000), however my analysis identified as disintegrating and so further analysis is necessary to reach a final conclusion. For the first binary, the two components of the PM of star are PMra=1039.92 $\pm$ 2.50 mas/yr and PMdec=-1737.58 $\pm$ 2.50 mas/yr (PM values are from GJC). The two components of the PM of the UCD are PMra=1034.03 $\pm$ 1.68 mas/yr and PMdec=-1725.69 $\pm$ 1.53 mas/yr (PM values are from Dwarf Archive). For the spectroscopic binary, the two components of the PM of the system are PMra=975.25 $\pm$ 2.50 mas/yr and PMdec=-1668.94 $\pm$ 2.50 mas/yr (PM values are from Gliese).

The GJ 570 system is a much cited system that is generally assumed to be a gravitationally bound multiple system. In my analysis this system is identified as a candidate disintegrating system due to the PM of GJ 570 BC being slightly different from the PM of the other members of the system. The PM difference is not very large, and it is possible that the catalogue proper motion values for this object may be high sigma outlier values. So although I have identified this system as a candidate disintegrating system, I do so with an element of caution.

Note that the assumed linear motion of components (in equation 14) will led to a scatter in the timings of closest separation, so the fact that they don't accrue at precisely the same time for these higher order multiples is not an issue of concern.

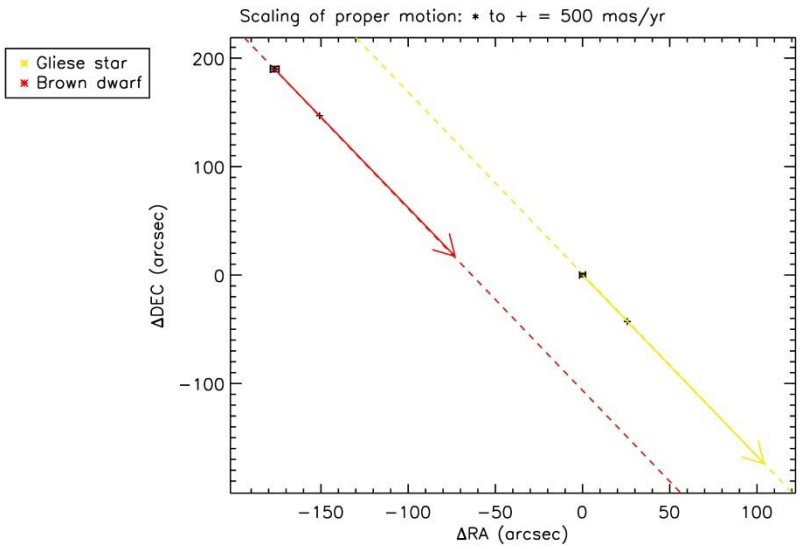

Figure 3.6: The proper motion of the star and UCD. The Gliese star is plotted in yellow and the BD is plotted in red. The large PM masks the small difference in alignment. The errors on the two components of the PM are plotted at the beginning of each arrow. The dashed lines are plotted to ease the comparison between the PMs directions.

In Figure 3.7 I show the separation between the components of the association as a function of time. The black line represents the separation between the BD and the host star (Gliese star 1) and the red line represents the separation between Gliese star 1 and the disrupting third body (Gliese Star 2). I can see that the system is disintegrating after the Gliese star 2 passes between Gliese star 1 and the BD. The spectroscopic binary continues on its path unaffected. The ejection velocity is high, as can be seen from the steep parabola, and the current separation between the BD and Gliese star 1 is 1500 AU, i.e. more than 1000 AU larger than the minimum. The uncertainty on the PM of both objects is small and therefore the shape and the minimum of the parabola are very reliable.

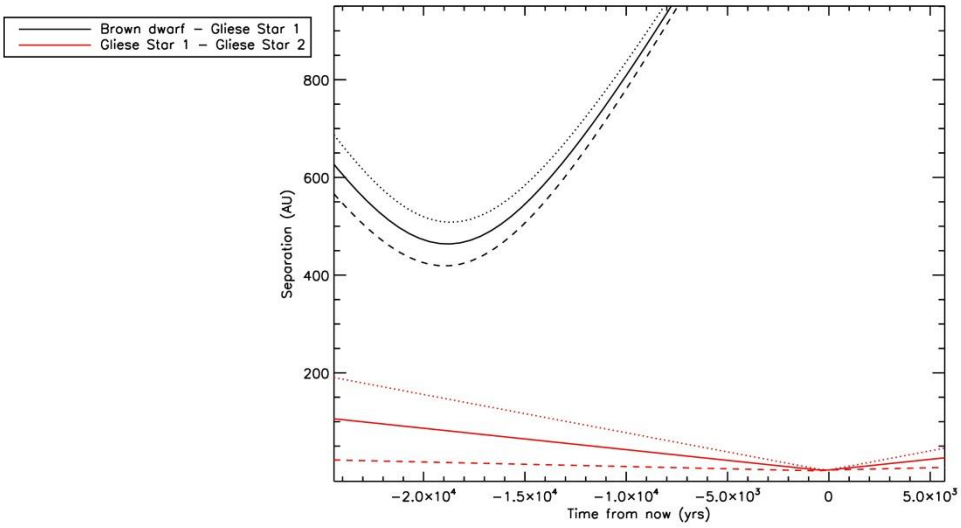

Figure 3.7: The separation between the components of the association as a function of time. The black line represents the separation between the BD and the host star (Gliese star 1) and the red line represents the separation between Gliese star 1 and the disrupting third body (Gliese Star 2). The association disintegrates after Gliese star 2 passes between the other two objects. For each parabola the one sigma error range is delimited by a dotted line (upper limit) and a dashed line (lower limit).

The properties of the association are summarized in Table 3.1.

Table 3.1: This table shows the properties of the objects of the disintegrating association.

Name of object	RA	DEC	D	PMra	PMdec	SpT	RV
GJ 570 A	14 57 28.00144	-21 24 55.7131	5.74 ± 0.20	1039.92 ± 2.50	-1737.58 ± 2.50	K4	26.79 ± 0.09
GJ 570 D	14 57 14.96	-21 21 47.8	5.84 ± 0.03	1034.03 ± 1.68	-1725.69 ± 1.53	T7.5	-
GJ 570 BC	14 57 26.53330	-21 24 41.5778	5.74 ± 0.20	975.25 ± 2.50	-1668.94 ± 2.50	M1.5	25.90 ± 2.00

Note: Distance is measured in pc, PM in mas/yr, and radial velocity is in km/s. In addition, GJ 570 A is a variable star and GJ 570 BC is a spectroscopic binary.

System 2

From the X-match of HMC with HMC, this association is made of 4 stars: one spectroscopic binary and 2 single stars. The spectroscopic binary is HR 4220, a B7 type star (Garcia et al. 1988), at a distance of 139.86 ± 9.00 pc. The third star is HR 4222, a B2.5 type star in the cluster IC 2602 (Garcia et al. 1988), at a distance of 134.59 ± 9.06 pc. The fourth star is HD 93738, a B9.5 type star (Houk & Cowley 1975) member of IC 2602 as well, at a distance of 138.70 ± 10.19 pc (all distances as measured by Hipparcos).

The proper motion of the stars is shown in Figure 3.8. The B7 spectroscopic binary is plotted in yellow while the B2.5 is plotted in red and the B9.5 is plotted in blue. I can see that the three PM align quite well, but the B7 binary has a higher PM compared to the other two stars. Nonetheless the

difference in PM is greater than 3 sigma. The fact that they are all cluster stars could explain the slightly different proper motions. Cluster members have about the same proper motion, but there is a bit of dispersion within the cluster. Conversely, a cluster represents a dense collection of stars, and members would be more likely to interact. So there are arguments on both sides as to whether this is likely to be a disintegrating system. For the spectroscopic binary, the two components of the PM are PMra=-18.87 ± 0.85 mas/yr and PMdec=12.06 ± 0.90 mas/yr. The two components of the PM of the third star are PMra=-17.75 ± 0.47 mas/yr and Pmdec=11.27 ± 0.40 mas/yr. For the fourth star, the two components of the PM are PMra=-17.95 ± 0.55 mas/yr and PMdec=10.35 ± 0.45 mas/yr (all PMs as measured by Hipparcos).

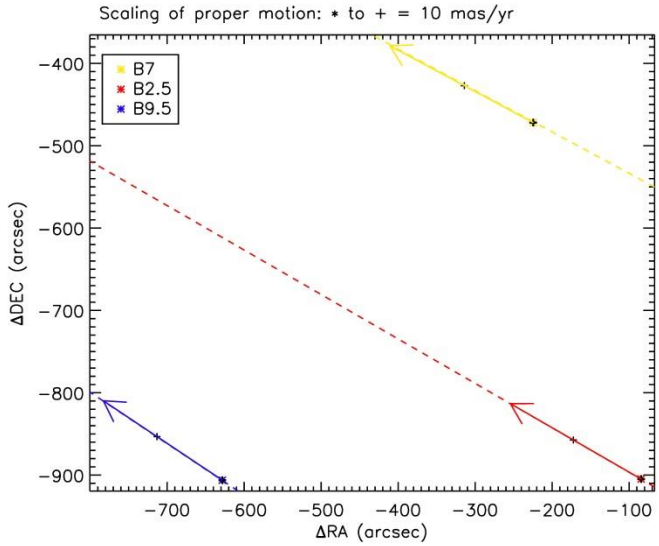

Figure 3.8: The proper motion of the stars. The B7 spectroscopic binary is plotted in yellow while the B2.5 is plotted in red and the B9.5 is plotted in blue. The three objects align very well while the B7 appear to have the highest PM of the group. The errors on the two components of the PMs are plotted at the beginning of each arrow. The dashed lines are plotted to ease the comparison between the PMs directions.

In Figure 3.9 I show the separation between the components of the system as a function of time. The separation between the B7 and the B2.5 is plotted in blue, the separation between the B7 and the B9.5 is plotted in yellow while the separation between the B2.5 and the B9.5 is plotted in red. I can see that the system is disintegrating. First the B7 interacts closely with the B9.5 and shortly after that the B2.5 and the B9.5 start moving apart from each other quickly.

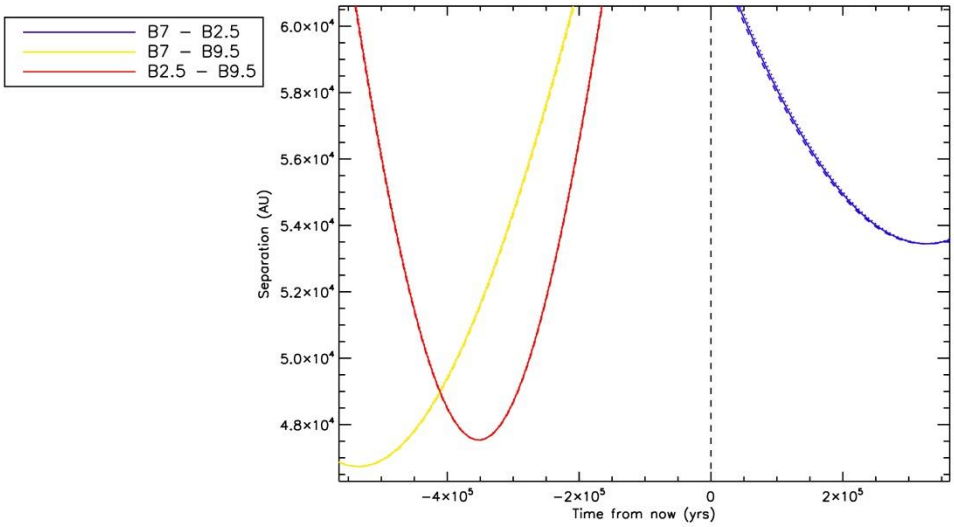

Figure 3.9: The separation between the components of the association as a function of time. The separation between the B7 and the B2.5 is plotted in blue, the separation between the B7 and the B9.5 is plotted in yellow while the separation between the B2.5 and the B9.5 is plotted in red. The association disintegrates after the B7 passes next to the B9.5. For each parabola the one sigma error range is delimited by a dotted line (upper limit) and a dashed line (lower limit).

The properties of the association are summarized in Table 3.2.

Table 3.2: This table shows the properties of the objects in the disintegrating association.

Name of object	RA	DEC	D	PMra	PMdec	SpT	RV
HR 4220	10 46 29.58853	-64 15 47.6653	139.86 ± 9.00	-18.87 ± 0.85	12.06 ± 0.90	B7	7.00 ± 1.00
HR 4222	10 46 51.21999	-64 23 00.5043	134.59 ± 9.06	-17.75 ± 0.47	11.27 ± 0.40	B2.5	12.00 ± 1.00
HD 93738	10 47 53.53059	-64 15 46.2247	138.70 ± 10.19	-17.95 ± 0.55	10.35 ± 0.45	B9.5	4 ± 1.00

Note: Distance is measured in pc, PM in mas/yr, and radial velocity is in km/s. In addition, HR 4220 is a spectroscopic binary and HR 4222 and HD 93738 are both members of IC 2602.

System 3

From the X-match between GJC and GJC, this system is made of 4 stars. The first star/system is a spectroscopic binary named HD 38A, a K6 type star (Tamazian et al. 2006), at a distance of 11.49 ± 0.50 pc. The third star is HD 38B, a M0.5 type star (Tamazian et al. 2006), at a distance of 11.49 ± 0.50 pc. The fourth star is BD+44 4548, a M2 type star (Joy & Abt 1974), at a distance of 11.49 ± 0.50 pc (all distances as measured by GJC).

The proper motion of the stars is shown in Figure 3.10. The K6 binary is plotted in yellow, the M0.5 is plotted in red, and the M2 is plotted in light blue. I can see that the M2 is passing between the K6

and the M0.5. Given the very small separation between the two M dwarfs it is very likely that this interaction triggered a disintegration of the K6-M0.5 system. Note that the difference between the PM of the K6 and M0.5 is larger than 3 sigma and is therefore a highly likely for it to be a genuine disintegrating system. For the spectroscopic binary, the two components of the PM are PMra=821.27 ± 2.50 mas/yr and PMdec=-171.57 ± 2.50 mas/yr. The two components of the PM of the third star are PMra=875.73 ± 2.50 mas/yr and PMdec=-127.75 ± 2.50 mas/yr (note that the errors are from GJC). For the fourth star, the two components of the PM are PMra=879.03 ± 2.50 mas/yr and PMdec=-162.92 ± 2.50 mas/yr (all PMs as measured by GJC).

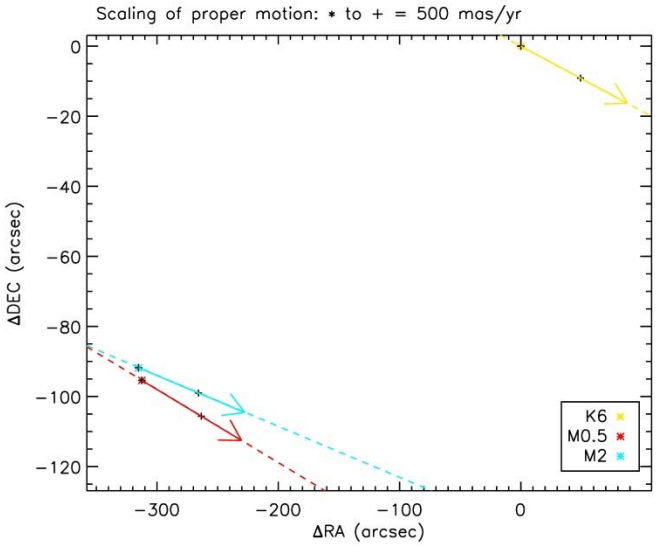

Figure 3.10: The proper motion of the stars. The K6 binary is plotted in yellow, the M0.5 is plotted in red, and the M2 is plotted in light blue. It is easy to see that the M2 is passing between the K6 and M0.5 and is therefore likely to disintegrate the K6-M0.5 system. The errors on the components of the PMs are plotted at the beginning of each arrow. The dashed lines are plotted to ease the comparison between the PMs directions.

In Figure 3.11 I show the separation between the components of the association as a function of time. The separation between the M2 and the K6 is plotted in yellow, the separation between the M0.5 and the K6 is plotted in red while the separation between the M2 and the M0.5 is plotted in blue. I can see that the system is disintegrating, because when the M2 gets closer to the M0.5 the separation between the M0.5 and the K6 starts increasing, approximately 3000 years ago.

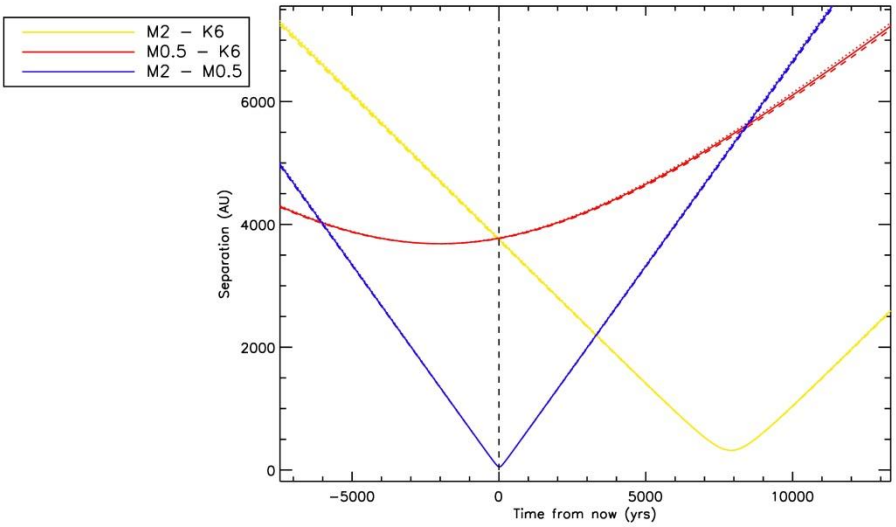

Figure 3.11: The separation between the components of the association as a function of time. The separation between the M2 and the K6 is plotted in yellow, the separation between the M0.5 and the K6 is plotted in red while the separation between the M2 and the M0.5 is plotted in blue. The interaction between the M2 and the M0.5 triggers the disintegration of the K6-M0.5 system. For each parabola the one sigma error range is delimited by a dotted line (upper limit) and a dashed line (lower limit).

The properties of the association are summarized in Table 3.3.

Table 3.3: This table shows the properties of the objects in the disintegrating association.

Name of object	RA	DEC	D	PMra	PMdec	SpT	RV
HD 38A	00 05 41.0129	+45 48 43.491	11.49 ± 0.50	821.27 ± 2.50	-171.57 ± 2.50	K6	3.50 ± 2.00
HD 38B	00 05 40.342	+45 48 38.73	11.49 ± 0.50	875.73 ± 2.50	-127.75 ± 2.50	M0.5	1.90 ± 2.00
BD+44 4548	00 05 10.88875	+45 47 11.6474	11.49 ± 0.50	879.03 ± 2.50	-162.92 ± 2.50	M2	-0.39 ± 0.09

Note: Distance is measured in pc, PM in mas/yr, and radial velocity is in km/s. In addition, HD 38A is a spectroscopic binary. The errors on the PMra and PMdec for HD 38B are acquired from GJC. Further, the error of RV for HD 38B is larger than the RV itself suggesting a rough measurement which needs to be improved perhaps in future work.

System 4

From the X-match between HMC and GJC, this system is made of 4 stars with 2 single stars and a known binary. The first star is HD 139323, a K3 type star (White et al. 2007), at a distance of 22.26 ± 0.36 pc (as measured by Hipparcos). The second star is HD 139341, a K1 type star (Gray et al. 2003), at a distance of 21.81 ± 0.37 pc (as measured by Hipparcos). The first star of the binary is BD+40 2905A, a K4 type star (Couteau 1966), at a distance of 21.28 ± 1.90 pc (as reported in GJC). The

second star of the binary is BD+40 2905B, a K5 type star (Couteau 1966), at a distance of 21.28 ± 1.90 pc (as reported in GJC).

The proper motion of the stars is shown in Figure 3.12. The K3 is plotted in blue, the K1 is plotted in light blue, and the K4 is plotted in yellow while the K5 is plotted in green. The K4 and the K5 are perfectly aligned as expected because they form a binary system. The K1 and the K3 seem to be getting closer to each other and neither of them aligns with the binary. The two components of the PM of the K3 are PMra=-448.91 ± 0.60 mas/yr and PMdec=50.29 ± 0.67 mas/yr (as measured by Hipparcos). The two components of the PM of the K1 are PMra=-482.47 ± 2.25 mas/yr and PMdec=27.52 ± 1.47 mas/yr (as measured by Hipparcos). The two components of the PM of the K4 are PMra=-461.23 ± 2.50 mas/yr and PMdec=59.08 ± 2.50 mas/yr (as measured by GJC). The two components of the PM of the K5 are PMra=-454.68 ± 2.50 mas/yr and PMdec=55.02 ± 2.50 mas/yr (as measured by GJC). The difference between the PMs is larger than 3 sigma.

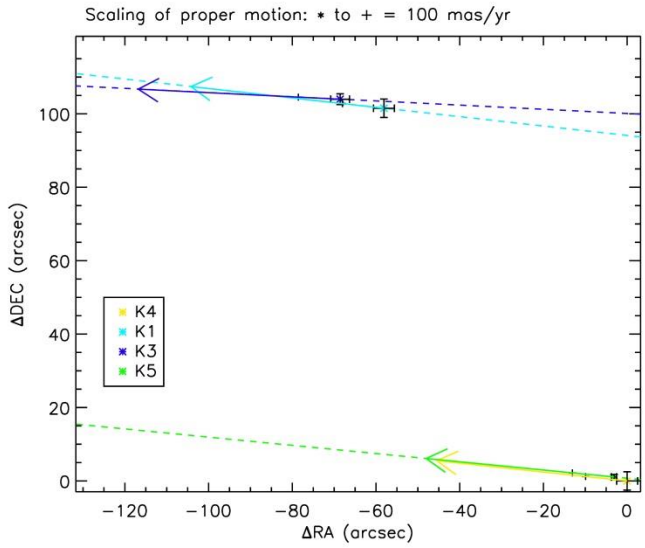

Figure 3.12: The proper motion of the stars. The K3 is plotted in blue, the K1 is plotted in light blue, and the K4 is plotted in yellow while the K5 is plotted in green. The K4 and the K5 clearly form a binary system, while the other two do not seem to be related. The errors on the components of the PMs are plotted at the beginning of each arrow. The dashed lines are plotted to ease the comparison between the PMs directions.

In Figure 3.13 I show the separation between the components of the association as a function of time. The separation between the K4 and the K1 is plotted in black, the separation between the K4 and the K3 is plotted in red, the separation between the K4 and the K5 is plotted in yellow, the separation between the K1 and the K3 is plotted in green, the separation between the K1 and the K5 is plotted in light blue while the separation between the K3 and the K5 is plotted in dark blue. I can see that the system is disintegrating. The four objects originally formed two separate binaries, the K4+K5 and the K1+K3 pairs. These two binaries interacted with each other and this caused the K1+K3 pair to be disintegrated, probably because their original separation was larger than the separation between the K4 and the K5. To confirm this theory one would need to run a dynamical simulation of the interaction.

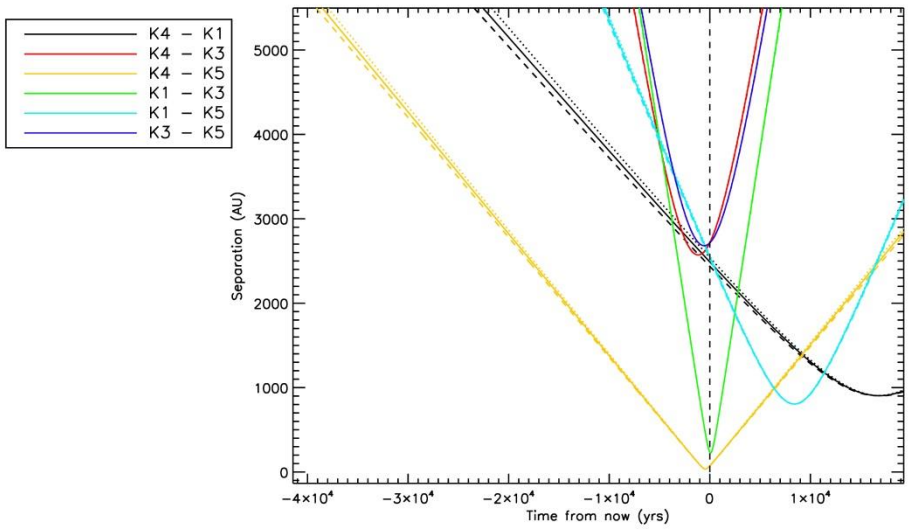

Figure 3.13: The separation between the components of the association as a function of time. The separation between the K4 and the K1 is plotted in black, the separation between the K4 and the K3 is plotted in red, the separation between the K4 and the K5 is plotted in yellow, the separation between the K1 and the K3 is plotted in green, the separation between the K1 and the K5 is plotted in light blue while the separation between the K3 and the K5 is plotted in dark blue. The interaction between the objects results in the K1+K3 pair being disintegrated. For each parabola the one sigma error range is delimited by a dotted line (upper limit) and a dashed line (lower limit).

The properties of the association are summarized in Table 3.4.

Table 3.4: This table shows the properties of the objects in the disintegrating association.

Name of object	RA	DEC	D	PMra	PMdec	SpT	RV
HD 139323	15 35 56.567	+39 49 52.03	22.26 ± 0.36	-448.91 ± 0.60	50.29 ± 0.67	K3	-66.88 ± 0.06
HD 139341	15 36 02.223	+39 48 08.91	21.81 ± 0.37	-482.47 ± 2.25	27.52 ± 1.47	K1	-66.70 ± 0.16
BD+40 2905A	15 36 02.239	+39 48 09.17	21.28 ± 1.90	-461.23 ± 2.50	59.08 ± 2.50	K4	-
BD+40 2905B	15 36 02.230	+39 48 09.53	21.28 ± 1.90	-454.68 ± 2.50	55.02 ± 2.50	K5	-

Note: Distance is measured in pc, PM in mas/yr, and radial velocity is in km/s. In addition, BD+40 2905A and BD+40 2905B form a binary system.

3.3 Other interesting systems

Although my main analysis identifies systems containing at least 3 components, I have also identified 2 double systems that contain a UCD (from DA) where the components have common distance, non-CPM, and are moving away from each other. However I have not included these associations in the previous section because there is not a third object nearby that can cause the ejection.

System 1

From the X-match between DA and GJC, this system is made of 1 star with 1 UCD. The star is GJ 1117, a DQ type white dwarf (Wills 1974), at a distance of 21.28 ± 1.36 pc (as stated in GJC). The UCD is 2MASS J08583467+3256275, a T1 type BD (Chiu et al. 2006), at a distance of 21.81 ± 5.02 pc (calculated using the Dupuy & Liu 2012 polynomial).

The proper motion of the objects is shown in Figure 3.14. The white dwarf is plotted in yellow and the BD is plotted in red. The two PMs are aligned quite well but the PM of the BD is almost twice the PM of the white dwarf. The two components of the PM of the white dwarf are PMra=-334.00 ± 2.50 mas/yr and PMdec=-2.00 ± 2.50 mas/yr (as reported in GJC). The two components of the PM of the BD are PMra=-652.50 ± 19.50 mas/yr and PMdec=20.90 ± 19.40 mas/yr (as stated in Dwarf Archive). The differences between the PM components are larger than 3 sigma.

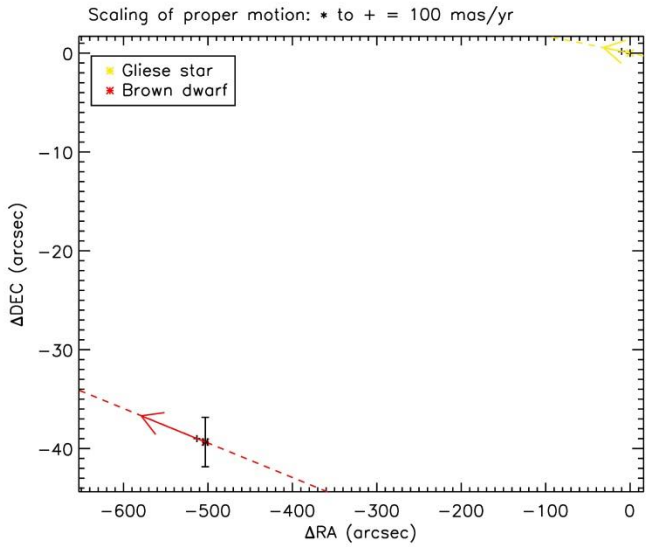

Figure 3.14: The proper motion of the star. The white dwarf is plotted in yellow and the BD is plotted in red. The BD is moving faster than the white dwarf, perhaps a sign that is being ejected. The error on the two components of the PM are plotted at the beginning of each arrow. The dashed lines are plotted to ease the comparison between the PMs directions.

In Figure 3.15 I show the separation between the components of the association as a function of time. I can see that the system is disintegrating. There is not any other object nearby that can be causing the ejection. However it is possible that the third object has not been detected yet, so I will need further deep observation around this association to look for additional components. Another possibility is that the BD is being ejected as a consequence of the evolution of the primary from main-sequence star to white dwarf. To confirm such possibility I have determined the age of the WD to check if the timing of the evolution of the WD matches the timing of the ejection of the T dwarf.

To do this, I first obtained T_{eff} and log g of the WD from Kleinman et al. (2013), T_{eff} = 12011 ± 166K and log g = 9.69 ± 0.103. I was then able to obtain the final mass (M_f) and the cooling age (t_c) of the WD, M_f = 1.366 $M_\odot$and t_c= 1.579 Gyr from the relations presented in Holberg & Bergeron (2006), Kowalski & Saumon (2006), Tremblay et al. (2011), and Bergeron et al. (2011). I could then estimate the mass of the progenitor of the WD (M_i) as 8 $M_\odot$ (using Catalan et al. 2008 initial-to-final mass

relation). I then used the main-sequence lifetime equation: $\frac{t}{t_{\odot}} \sim (\frac{\mathrm{M}}{\mathrm{M}_{\odot}})^{-2.5}$ where t is the main-sequence lifetime, $t_{\odot}$ is the age of the Sun ($\sim 10^{10}$yr), M is the mass of the progenitor, i.e. M_i, and $\mathrm{M}_{\odot}$ is the mass of the Sun, i.e. 1. I calculated the main-sequence age of the WD to be approximately 55 Myr. Hence the total age of the WD is then approximately 1.63 Gyr (t_c + t).

Hence for approximately 1335 years ago, when GJ 1117 and the T dwarf were about 1000 AU apart, GJ 1117 had already evolved into a WD. By determining the age of the WD, the initial conclusion is that the non-matching timing of the evolution of the WD and the ejection of the T dwarf rule out the possibility that the T dwarf is being ejected due to the evolution of the WD.

There is of course the possibility that this is not a real disintegrating system, but just two stars randomly nearby in the sky. To test this possibility I followed the method described in Gomes et al. (2013). First I have calculated the volume of a cone with the base radius equal to the separation between the DQ and the T1, and the height equal to the distance of the system. I then calculated the number of stars that could randomly happen to be in that volume, by multiplying that volume times the average density of stars. From Reid et al. (2007), this is 0.076 stars pc^{-3}. The number of stars that could randomly be in that volume is therefore 4.29×10^{-3}. Then I calculated the number of stars in GJ that have their PM aligned with the PM of the T1. I then divided that number by the area of the full sky, i.e. 41253 deg^2, to calculate the expected number of stars with PM in that direction per deg^2. Finally I have multiplied that number times the area of the sky occupied by the DQ + T1 system, i.e. simply the area of a circle with radius equal to the separation between the WD and the BD. This is the number of stars with PM in the same direction as the T1 that could randomly happen to be close to the T1. The number is 4.53×10^{-4}. The numbers calculated above are very small, and therefore I am reasonably confident that the GJ1117 system is a genuine disintegrating system.

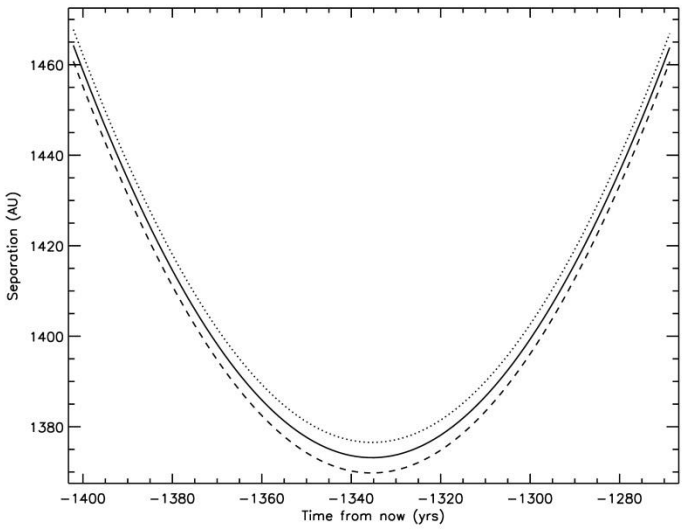

Figure 3.15: The separation between the components of the association as a function of time. The BD could be ejected because of a hidden third object or due to the evolution of the more massive primary. For each parabola the one sigma error range is delimited by a dotted line (upper limit) and a dashed line (lower limit).

The properties of the association are summarized in Table 3.5.

Table 3.5: This table shows the properties of the objects in the disintegrating association.

Name of object	RA	DEC	D	PMra	PMdec	SpT	RV
GJ 1117	08 59 14.76	+32 57 12.1	21.28 ± 1.35	-334.00 ± 2.50	-2.00 ±2.50	DQ	-
2MASS J08583467+3256275	08 58 34.672	+32 56 27.56	21.81 ± 5.01	-652.50 ± 19.50	20.90 ± 19.40	T1	-

Note: Distance is measured in pc, PM in mas/yr, and radial velocity is in km/s.

System 2

From the X-match between DA and HMC, this system is made of a spectroscopic binary with a UCD. The spectroscopic binary is eta CrB, a G2 type star (Struve & Franklin 1955), at a distance of 18.62 ± 0.43 pc (as measured by Hipparcos). The UCD is eta CrB C, a L8 type BD (Schneider et al. 2014), at a distance of 17.86 ± 0.25 pc (as reported in Dwarf Archive).

The proper motion of the objects is shown in Figure 3.16. The spectroscopic binary is plotted in yellow and the BD is plotted in red. It can be seen by eye that the two PMs are diverging. The two components of the PM of the spectroscopic binary are PMra=125.77 ± 0.62 mas/yr and PMdec=-176.48 ± 0.81 mas/yr (as measured by Hipparcos). The two components of the PM of the BD are PMra=142.99 ± 4.42 mas/yr and PMdec=-169.03 ± 4.89 mas/yr (as stated in Dwarf Archive). The difference between the PMs is larger than 3 sigma.

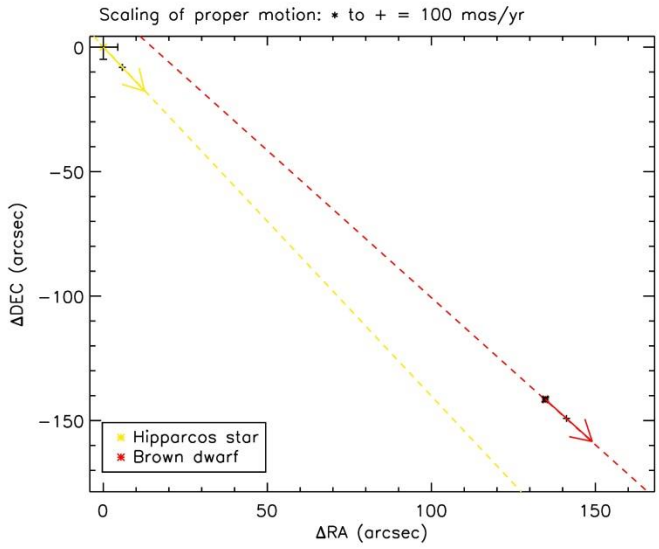

Figure 3.16: The proper motion of the stars. The spectroscopic binary is plotted in yellow and the BD is plotted in red. The difference between the PMs is very small. The errors on the two components of the PMs are plotted at the beginning of each arrow. The dashed lines are plotted to ease the comparison between the PMs directions.

In Figure 3.17 I show the separation between the components of the association as a function of time. I can see that the system is disintegrating. There is not any other object nearby that can be causing the ejection. However it is possible that the third object has not been detected yet, so I will

need deeper observations around this association to look for additional components. Another possibility is that the BD is being ejected as a consequence of the dynamical interaction with the spectroscopic binary, i.e. the system could be unstable to begin with, without needing any external influence. To confirm this theory one would need to run a dynamical simulation of the association.

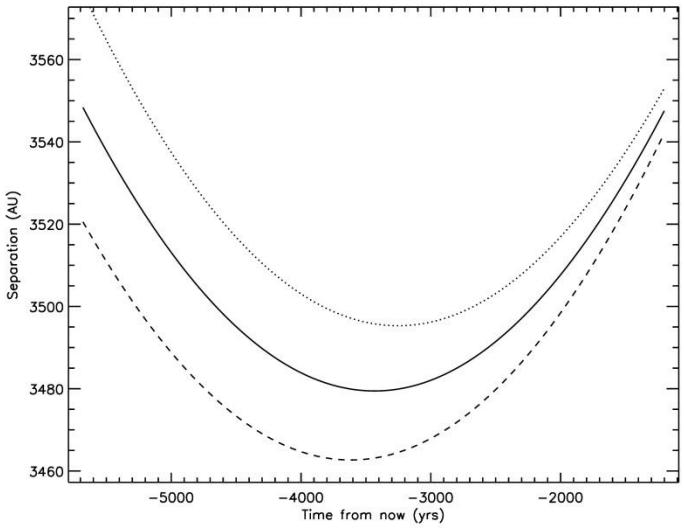

Figure 3.17: The separation between the components of the association as a function of time. The BD could be ejected because of a hidden third object or due to the dynamical interaction with the spectroscopic binary. For each parabola the one sigma error range is delimited by a dotted line (upper limit) and a dashed line (lower limit).

The properties of the association are summarized in Table 3.6.

Table 3.6: This table shows the properties of the objects in the disintegrating association.

Name of object	RA	DEC	D	PMra	PMdec	SpT	RV
eta CrB	15 23 12.305	+30 17 16.17	18.62 ± 0.43	125.77 ± 0.62	-176.48 ±0.81	G2	-7.26 ± 0.05
eta CrB C	15 23 22.63	+30 14 56.2	17.86 ± 0.25	142.99 ± 4.42	-169.03 ± 4.89	L8	-

Note: Distance is measured in pc, PM in mas/yr, and radial velocity is in km/s. Note that eta CrB is a spectroscopic binary.

I have identified similar systems from the other X-matches. There are 44 associations of this type from the HMC-HMC X-match, 56 from the GJC-GJC X-match, and 12 from the HMC-GJC X-match. As for the systems above, these require further investigation.

Chapter 4

4. Conclusions and future work

4.1 Conclusions

This project was carried out with the motivation of expanding our knowledge of the orbital population of very low-mass stars, BDs and giant planets. This task is challenging due to the very faint nature of low-mass objects compared to the much brighter primary stars in the systems (especially at visible wavelengths). Moreover, the proximity to the primary star makes these low-mass objects even harder to study, since the glare of the parent star "washes out" the companions. To observe them, one needs to block the light from the primary stellar object (hence reducing its glare), but this is a technical challenge. Such problem can be avoided identifying systems where the low-mass members are being ejected dynamically.

The contribution in searching for possible disintegrating multiple systems in this project is fundamental in providing further constrains to the formation models.

Knowing the mass of a stellar object is fundamental for astrophysicists to determine the properties and nature of the observed body. This important parameter in general can be derived via the mass-luminosity relation. However UCDs do not have substantial initial mass to ignite and sustain nuclear fusion. Measuring the luminosity of these low-mass objects is proven to be a challenge. Although only a few of them have been discovered so far, benchmark systems (systems consisting of at least one main-sequence star and at least one BD, preferably with a good age estimate) play a key role in this case. It is known that the components of most binary systems form around the same time from the same cloud. Under this logic, the components should share similar metallicity and age. To determine the mass of a dim object, it is crucial to know its age and T_{eff} (see Chapter 1, Figure 1.1). It is possible to deduce the age of the primary star in the system and assume the same age for the secondary dimmer object. However to obtain T_{eff}, a precise measurement of the distance of the primary object is necessary. This requirement is fulfilled by the use of the Hipparcos catalog in this study. Note that the binary systems were born from the same molecular cloud hence both components are within the same distance. Though, Hipparcos solely provide information for the primary. The information for the secondary object comes from NIR sensitive surveys, e.g. SDSS, 2MASS and UKIDSS. To obtain T_{eff}, from known distance and apparent magnitude, with the aid of the distance modulus, the absolute magnitude can be determined. Then by using a bolometric correction (a constant depending on the spectral type of the secondary object), the bolometric luminosity can be determined. T_{eff} is then calculated using the Stefan-Boltzmann equation. Note that benchmark systems can also be used to test out models and theories (i.e. evolutionary models, e.g. Mohanty et al. 2004a,b; Dupuy et al. 2009, and atmospheric models, e.g. Burningham et al. 2009; Pinfield et al. 2012).

Given the extremely dim nature of UCDs, detecting them can be challenging. More advanced near-infrared telescopes, more effective in picking up these very low-mass objects, have been built over

the years. Astronomers came up with new methods to try to spot these very dim UCDs, exploiting the very deep modern near-infrared surveys. Yet there are still a lot of these UCDs not being detected, hence the need for more fresh ideas are always on demand. An example of this will be the recent discovery of Luhman 16, a faint UCD binary located in the solar neighbourhood (Luhman 2014). Another problem is to study UCDs while they are part of a multiple system, because especially for close systems, the glare of the parent star could make it extremely difficult. To overcome this issue, being able to search for and study multiple systems that are disintegrating can become essential. While the multiple systems are disintegrating, the less massive component can be ejected and become suitable to study once it gets out of the glare of the parent star. Furthermore, while the multiple systems are disintegrating, the orbit/s of the ejected object/s is/are likely to be unstable. And if there are even less massive objects bound to the ejected UCDs, the chances are that these will get ejected too.

Understanding the dominant formation mechanism of ultra-cool objects have been for a long time one of the main research interests among the low-mass community. Various formation models have been suggested, but to improve these models, observational constrains are fundamental, especially on the IMF and the binary fraction. This work might provide an answer to the origin of some of the field object and even the initial requirements in capture.

A method has been defined to identify candidate disintegrating multiple systems using (i) distance measurements and constraints from trigonometric parallax and spectrophotometric techniques, (ii) relative proper motions and their associated measurement uncertainties, and (iii) relative component positions that are tracked back and projected forward through time. This method has been applied to three catalogue/database compilations, namely DA (for UCDs), HMC, and GJC. This has resulted in four candidate disintegrating multiple systems with >2 components (all four being quadruples showing some evidence of possible disintegration). The proper motions of the system components are not strongly divergent within each system, but in all cases there is one component whose proper motion is significantly different, always >3 sigma from the other constituents, and ranging up to ∼10 sigma difference in one case. One of these four systems contains a UCD (GJ 570 D), although this is not the component with a divergent proper motion. Another consists mainly of known members of the open cluster IC 2602, and the other two systems consist of M-K dwarfs and K dwarfs respectively.

In addition I have identified two candidate disintegrating double systems, each containing one UCD component. The first one contains a T dwarf and a white dwarf, with the T dwarf having a proper motion approximately twice the magnitude of the white dwarf's (∼15 sigma difference), and in essentially the same direction. The second one has been previously identified as a bound multiple system, though the proper motions of its components differ by ∼8 sigma. In both cases the relative motions show that the components were closer together in the past, with the T-white dwarf system predicted to be within ∼1400 AU about 1300 year ago. My analysis method has thus been successful in identifying possible disintegrating multiple systems that are inconsistent with gravitationally bound wide multiples. Moreover, there are 44 associations of this type from the HMC-HMC X-match, 56 from the GJC-GJC X-match and 12 from the HMC-GJC X-match.

As a by-product of my search I have also identified several CPM multiple systems that were either previously unreported or contain more components than have previously been recognised. The spectral type of the components in these three multiple systems are; K1+K5 (spectroscopic binary), M0+M2 and M1+M3.5+M4. It was expected that my analysis method would re-identify many CPM multiples, but a potential for previously unreported wide separation components has also been realised, due to the large separation range searched.

Confirmation and further study of my candidate disintegrating multiple systems should be able to place new constraints on the typically unseen constituents of multiple systems, by revealing the full range of components during disintegration. The observed frequency of disintegrators will also inform us about the rate at which such systems interact in the Galactic disk. And through further work I should be able to extend the low-mass range over which I can identify disintegrating components.

4.2 Future work

The candidate disintegrating systems identified in this work should be examined further using *Gaia* (Cacciari, Pancino & Bellazzini 2015) data and ground-based follow-up observations. More accurate proper motion and parallax measurements of the components would assess my own selection criteria at higher accuracy. And it would be particularly interesting to examine early *Gaia* proper motions to confirm if the GJ 570 system really does have a member with divergent proper motion. Radial velocity measurements (from *Gaia* or ground based telescopes) would also give 3-D velocities for the components of my candidate systems, which would allow dynamical studies to determine if the systems are gravitationally unbound. If the T dwarf + WD disintegrating double system is confirmed by *Gaia*, then a detailed study could constrain the white dwarf cooling age, and search for any unusual features of the T dwarf spectrum that may have arisen during a period when the components were in closer proximity.

I also plan to investigate the possibility that my disintegrating multiple systems could have additional faint components that do not appear in DA. Deep near infrared imaging in the region of my candidates might reveal cooler components that are also involved in the disintegration process. The dynamical interaction that resulted in the disintegration could potentially have released additional lower mass components, and these could now be widely separated from their original host and thus detectable.

Beyond my current analysis of the DA, HMC and GJC database/catalogue resources, I can also expand my method to additional surveys and facilities. *Gaia* will soon provide extremely accurate proper motions and parallaxes for stars and UCDs down to V=20. And a much larger sample of UCDs could be included by selecting photometric candidates from UKIDSS, UHS, VISTA, WISE and SDSS.

Reference

Aarseth, S. J. 2003, Regularization tools for binary interactions, in Astrophysical Supercomputing Using Particle Simulations, ed. J. Makino, & P. Hut (ASP), 295

Aarseth, S. J. 2004, in The Environment and Evolution of Double and Multiple Stars, IAU Colloq. 191, RevMexAA, Ser. Conf., 21, 156

Abel, M. & Frommhold, L., 2013, CaJPh, 91, 857

Abt, H. 1983, ARAA, 21, 343

Abt, H. 1987, ApJ, 317, 353

Adams, F. C., Ruden, S. P., & Shu, F. H. 1989, ApJ, 347, 959

Ahmic, M., Jayawardhana, R., Brandeker, A., et al. 2007, ApJ, 671, 2074

Aitken, R. G. 1935, The Binary Stars (New York: McGraw—Hill), 275

Alibert Y., Mordasini C., Benz W., & Winisdoerffer, C. 2005, A&A, 434, 343

Allard, F., Homeier, D., Freytag, B. 2013, Memorie della Societa Astronomica Italiana, v. 84, No. 4, p. 1053

Allard, F. 2014, Exploring the Formation and Evolution of Planetary Systems, IAU Symposium, Volume 299, pp. 271-272

Allard, F., Hauschildt, P. H., Alexander, D. R., & Starrfield, S. 1997, ARA&A, 35, 137

Allard, F. et al. 2011, ASPC, 448, 91

Allen, P. R., Koerner, D. W., McElwain, M. W., Cruz, K. L., & Reid, I. N. 2007, AJ, 133, 971

Alves de Oliveira, C., Moraux, E., Bouvier, J., Bouy, H., 2012, A&A, 539, A151

Alves de Oliveira, C., Moraux, E., Bouvier, J., Duchene, G., Bouy, H., Maschberger, T., Hudelot, P., 2013, A&A, 549, A123

Andersen, M., Meyer, M., Greissl, J., & Aversa, A. 2008, ApJ, 683, L183

Andersen, M., Meyer, M. R., Robberto, M., Bergeron, L. E., Reid, N., 2011, A&A, 534, A10

Anderson, D. et al. 2010, ApJ, 726, L19

André, P., Ward-Thompson, D., & Greaves, J. 2012, Science, 337, 69

Anosova, J. P. 1989, in Highlights of Astronomy, vol. 8, ed. D. McNally (Dordrecht: Kluwer), 143

Anosova, J. P., 1990, Celest. Mech. Dyn. Astron., 48, 357

Attwood, R., Good win, S., Stamatellos, D, & Whitworth, A. 2009, A&A, 495, 201

Bakos et al. 2007, sptz, prop, 297

Bakos et al. 2011, ApJ, 742, 116

Baraffe, I., Chabrier, G., & Barman, T. 2008, A&A, 482, 315

Baraffe, I., Chabrier, G., & Barman, T. 2010, Reports on Progress in Physics, 73, 016901

Barrado y Navascués, D., Bouvier, J., Stauffer, J. R., Lodieu, N., McCaughrean, M. J., 2002, A&A, 395, 813

Basri, G., Marcy, G. W., & Graham, J. R. 1996, ApJ, 458, 600

Basri, G., & Reiners, A. 2006, AJ, 132, 663

Bastian, N., Covey, K. R., & Meyer, M. R. 2010, ARA&A, 48, 339

Bate, M. R. 2000, MNRAS, 314, 33

Bate, M. R. 2009, MNRAS, 392, 590

Bate, M. R. 2012, MNRAS, 419, 3115

Bate, M. R., Bonnell, I. A., & Bromm, V. 2002, MNRAS, 332, L65

Becklin, E. E. & Zuckerman, B. 1988, Nature, 336, 656

Bergeron et al. 2011, ApJ, 737, 28

Berriman & Reid 1987, MNRAS, 227, 315

Bodenheimer, P. 1978, ApJ, 224, 488

Bodenheimer, P., Ruzmaikina, T., & Mathieu, R. 1992, in Protostars and Planets III, eds. E. Levy, J. Lunine, & M. S. Matthews (Tucson: University of Arizona Press), in press.

Bodenheimer, P. 1992, IAUS, 151, 9

Bodenheimer, P. H. 2011, Principles of Star Formation: Astronomy and Astrophysics Library. ISBN 978-3-642-15062-3, Springer-Verlag Berlin Heidelberg

Boley, A. C. et al. 2010, Icarus, 207, 509

Boley, A. C. 2009, ApJ, 695, L53

Boss, A. P. et al. 2003, in Brown Dwarfs, ed. E., Martín, (ASP, San Francisco), IAU Symposium, 211, 529

Boss, A. P. 1986, ApJS, 62, 519

Boss, A. P. 1988, Comments Ap, 12, 169

Boss, A. P. 1991, Nature, 351, 298

Boss, A. 1997, Science, 276, 1836

Boss, A. P. 2012, MNRAS, 419, 1930

Bouchy, F. et al. 2011, A&A, 525, A68

Boudreault, S., Lodieu, N., Deacon, N. R., Hambly, N. C., 2012, MNRAS, 426, 3419

Bouy, H., Brandner, W., Mart´ın, E. L., Delfosse, X., Allard, F., & Basri, G. 2003, AJ, 126, 1526

Boyd, D. & Whitworth, A. 2005, A&A, 430, 1059

Bressert, E. et al. 2010, MNRAS, 409, L54

Burgasser, A. J. et al. 2000a, AAS, 19510913

Burgasser, A. J. et al. 2000b, ApJ, 531L, 57

Burgasser, A.J. et al. 2002, ApJ, 564, 421

Burgasser, A. J., Kirkpatrick, J. D., Liebert, J., & Burrows, A. 2003b, ApJ, 594 ,510

Burgasser, A. J. et al. 2003c, ApJ, 586, 512

Burgasser, A. J. et al. 2005, AJ, 129, 2849

Burgasser, A. J., Geballe, T. R., Leggett, S. K., Kirkpatrick, J. D., & Golimowski, D. A. 2006, ApJ, 637, 1067

Burgasser, A. J. et al. 2007, prpl, conf, 427

Burgasser, A. J. et al. 2010, ApJ, 710, 1142

Burleigh et al. 2009, sptz, prop60161

Burningham, B. et al. 2009, MNRAS, 395, 1237

Burningham, B. et al. 2010, MNRAS, 406, 1885

Burningham, B. et al. 2013, MNRAS, 433, 457

Burrows, A., Hubbard, W. B., Lunine, J. I., & Liebert, J. 2001, Reviews of Modern Physics, 73, 719

Burrows, A., Sudarsky, D., & Lunine, J. I. 2003, ApJ, 596, 587

Burrows, A. et al. 2006, ApJ, 640, 1063

Caballero, J. 2010, A&A, 514A, 98

Caballero, J. et al. 2006, A&A, 460, 635

Caballero, J. et al. 2007, A&A, 470, 903

Cacciari, C., Pancino, E. & Bellazzini, M. 2015, arXiv, 151203658

Casewell, S. L. et al. 2007, MNRAS, 378, 1131

Casewell, S. L. et al. 2012, ApJ, 759, 34

Casewell, S. L. & Hambly, N. 2013, ASSP, 37, 291

Catalan, S. et al. 2008, A&A, 477, 901

Catalan, S. et al. 2008, A&A, 477, 213

Chabrier, G. 2002, ApJ, 567, 304

Chabrier, G. 2003, PASP, 115, 763

Chabrier, G. 2005, in Astrophysics and Space Science Library, Vol. 327, The Initial Mass Function 50 Years Later, 41

Chabrier, G. & Baraffe, I. 1997, A&A, 327, 1039

Chabrier, G. & Baraffe, I. 2000, ARA&A, 38, 337

Chabrier, G. et al. 2010, IAUS, 276, 171

Chabrier, G., Johansen, A., Janson, M., & Rafikov, R. 2014, arXiv, 1401, 7559

Chauvin, G. et al. 2004, A&A, 425, L29

Chiu et al. 2006, AJ, 131, 2722

Clarke, C., and Pringle, J. E. 1991a, MNRAS, 249, 584

Clarke, C., and Pringle, J. E. 1991b, MNRAS, 249, 588

Couteau, P. 1966, JO, 49, 369

Cowley et al. 1967AJ, 72, 1334

Cross et al. 2012, A&A, 548A, 119

Cruz et al. 2007, AAS, 210, 9601

Cruz et al. 2009, AJ, 137, 3345

Cushing, M. C., Kirkpatrick. J. D., Gelino, C. R., et al. 2011, ApJ, 743, 50

Cushing, M. C. et al. 2006 ApJ, 648, 614

Davidson, K. 1975, Does the Solar System Include Distant but Discoverable Infrared Dwarfs?, Icarus, Volume 26, p. 99-101

Day-Jones 2010, Ph. D. dissertation, University of Hertfordshire

Day-Jones et al. 2011, MNRAS, 410, 705

Deleuil, M., et al. 2008, A&A, 491, 889

Delorme et al. 2012, A&A, 548A, 26

Delorme et al. 2013, Memorie della Societa Astronomica Italiana, v.84, No. 4, p.1013

De Rosa, R. J., Patience, J., Wilson, P. A., et al. 2014, MNRAS, 437, 1216

Dhital, S., Burgasser, A. J., Looper, D. L., & Stassun, K. G. 2011, AJ, 141, 7

Dupuy, T. J., & Liu, M. C. 2012, ApJS, 201, 19

Dupuy, T. J. et al. 2009, IAUS, 258, 337

Duquennoy, A., & Mayor, M. 1991, A&A, 248, 485

Durisen, R. H., Gingold, R. A., Tohline, J. E., & Boss, A. P. 1986, ApJ, 305, 281

Emerson et al. 2004, Msngr, 117, 27

Epchtein, N. et al. 1999, A&A, 349, 236

Faherty, J. K., Burgasser, A. J., Cruz, K. L., et al. 2009, AJ, 137, 1

Faherty, J. K. et al. 2010, AJ, 139, 176

Fekel, F. C., Jr 1981, ApJ, 246, 879

Fregeau et al. 2004, MNRAS, 352, 1

Frommhold, L. 2006, Collision-induced Absorption in Gases: Cambridge University Press

Folkes et al. 2007, MNRAS, 378, 901

Forgan, D. & Rice, K. 2011, MNRAS, 417, 1928

Fortney, J. J., Marley, M. S., & Barnes, J. W. 2007, ApJ, 659, 1661

Fortney, J. J., Marley, M. S., Saumon, D., & Lodders, K. 2008, ApJ, 683, 1104

Gagne' et al. 2014, ApJ, 783, 121

Garcia, B. et al. 1988, Ap&SS, 148, 163

Geballe, T. R., Knapp, G. R., Leggett, S. K. et al, 2002, ApJ, 564,466

Gizis J. E., Kirkpatrick J. D., Wilson J. C., 2001, AJ, 121, 2185

Gliese & Jahreiß 1979, A&AS, 38, 423

Golimowski, D. A. et al. 2004, AJ, 128, 1733

Gomes et al. 2013, MNRAS, 431, 2745

Goodwin, S., Whitworth, A., & Ward-Thompson, D. 2004, A&A, 414, 633

Gray et al. 2003, AJ, 126, 2048

Gray et al. 2006, AJ, 132, 161

Grether, D. & Lineweaver, C. H. 2006, ApJ, 640, 1051

Guenther E. W., and Wuchterl G. 2003, Astron. Astrophys., 401, 677-683

Halbwachs, J.-L. 1987, A&A, 183, 234

Hambly et al. 2008, MNRAS, 384, 637

Heller, C. 1991, Ph. D. dissertation, Yale University

Helling, C. et al. 2008, ApJ, 675L, 105

Helling, C. et al. 2008, MNRAS, 391, 1854

Helling, C. & Casewell, S. 2014 A&ARv, 22, 80

Hennebelle, P. & Chabrier, G. 2008, ApJ, 684,395

Hennebelle, P. & Chabrier, G. 2009, ApJ, 702, 1428

Henry, T. J. 2009, in ASS Meeting #213, #407.5: Bulletin of the American Astronomical Society, Vol. 41, p.203

Hester, J. J., Scowen, P. A., Sankrit, R., et al. 1996, AJ, 111, 2349

Hills, J. G. 1976, MNRAS, 175,1P

Hills, J. G., and Day, C. A. 1976, ApL, 17, 87

Holberg & Bergeron 2006, AJ, 132, 1221

Houk & Cowley 1975, mcts, book

Hoyle, F. 1953, ApJ, 118, 513

Hubbard, W. B. 1977, Icarus, 30, 305

Jarvis, M. 2012, sngi, confE, 13

Jeans, J. H. 1929, Astronomy and Cosmogony, 2nd ed. (Cambridge: Cambridge University Press)

Joergens, V. 2006, A&A, 446, 1165

Joergens, V. 2008, A&A, 492, 545

Johnson, J., et al. 2011, ApJ, 730, id.79

Joy & Abt 1974, ApJS, 28, 1

Kirkpatrick, J. D. 2005, ARA&A, 43, 195

Kirkpatrick, J. D. 2008, in ASP Conf. Ser. 384, 14th Cambridge Workshop on Cool Stars, Stellar Systems, and the Sun, ed. G. van Belle (San Francisco, CA: ASP), 85

Kirkpatrick, J. D. et al. 1991, ApJS, 77, 417

Kirkpatrick, J. D., Henry, T. J., & Liebert, J. 1993, ApJ, 406, 701

Kirkpatrick, J. D., Reid, I. N., Liebert, J., et al. 1999, ApJ, 519, 802

Kirkpatrick, J. D. et al. 2000, AJ, 120, 447

Kirkpatrick J. D., Dahn C. C., Monet D. G., Reid I. N., Gizis J. E., Liebert J., Burgasser A. J., 2001, AJ, 121, 3235

Kirkpatrick, J. D., Cushing. M. C., Gelino, C. R. et al., 2011, ApJS, 197, 19

Kirkpatrick, J. D., Gelino, C. R., Cushing, M. C., et al. 2012, ApJ, 753,156

Kleinman, S.J. et al 2013, ApJS, 204, 5

Knapp, G. R. et al. 2004, AJ, 127, 3553

Kobulnicky, H. A., and Fryer, C. L. 2007, Astrophys. J., 670, 747

Konopacky, Q. M., Barman, T. S., Macintosh, B. A., & Marois, C. 2013, Science, 339, 1398

Kowalski & Saumon 2006, ApJ, 651, L137

Kroupa, P. 2001, MNRAS, 322, 231

Kumar, S. S. 1963, AJ, 137, 1121

Kurosawa et al. 2006, MNRAS, 372, 1879

Lada C. J. 2006, ApJ, 640L, 63

Larson, R. B. 1990, in Physical Processes in Fragmentation and Star Formation, eds. R. Capuzzo-Dolcetta, C. Chiosi, & A. DiFazio (Dordrecht: Kluwer), 389

Lattanzio, J. C., & Henriksen, R. N. 1988, MNRAS, 232, 565

Lattanzi, M. G., Jancart, S., Morbidelli, R., et al. 2004, in The Three- Dimensional Universe with Gaia, ed. C. Turon, K. S. OFlaherty, & M. A. C. Perryman, 251

Lawrence, A., Warren, S. J., Almaini, O., et al. 2007, MNRAS, 379, 1599

Leconte, J., Baraffe, I., Chabrier, G., Barman, T., & Levrard, B. 2009, A&A, 506, 385

Leconte, J., Chabrier, G., Baraffe, I., & Levrard, B. 2011, EPJ Web of Conferences, 11, id.03004

Leggett, S. K. et al. 2008, ApJ, 682, 1256

Leggett, S. K. et al. 2010, ApJ, 710, 1627

Li, P. J. et al. 2009, A&A, 504, 277

Li, X. et al. 2012, ICCMSE 2009, AIPC, 1504, 100

Liebert, J., et al., 1984, ApJ, 282, 758

Linsky, J. L., 1969, ApJ, 156, 989

Liu, M. C., Delorme, P., Dupuy, T. J. et al., 2011, ApJ, 740, 108

Lodieu, N., Dobbie, P. D., Deacon, N. R., Hodgkin, S. T., Hambly, N. C., Jameson, R. F., 2007, MNRAS, 380, 712

Lodieu, N., Zapatero Osorio, M. R., Rebolo, R., Martín, E. L., Hambly, N. C., 2009, A&A, 505, 1115

Lodieu et al. 2011, A&A, 527, A24

Lodieu, N., Deacon, N. R., Hambly, N. C. 2012a, MNRAS, 422, 1495

Lodieu, N. et al. 2013,MNRAS,435,2474

Lucas, P. W. et al. 2001, MNRAS, 326, 695

Lucas, P. W., Tinney, C. G., Burningham, B. et al. 2010, MNRAS, 408, L56

Luhman, K. L. 2004, ApJ, 617, 1216

Luhman, K. L. 2012, ARA&A, 50, 65

Luhman, K. L. 2014, ApJ, 781, 4

Luhman K. L., McLeod K. K., and Goldenson N. 2005, Astrophys. J., 623, 1141-1156

Luhman, K. L. et al. 2007, Protostars and Planets V, B. Reipurth, D. Jewitt, and K. Keil (eds.), University of Arizona Press, Tucson, 951 pp., 2007., p.443-457Marcy, G. W. & Butler, R. P. 2000, PASP, 112, 137

Luhman, K. L. et al. 2011, ESS, 2, 1503

Luyten, W. J. 1979, Proper Motion Survey, University of Minnesota, 52, 1

Ma, B. & Ge, J. 2014, MNRAS, 439, 2781

Mace, G. N. et al. 2013, ApJS, 205, 6

Madhusudhan, N., et al. 2011, Nature, 469, 64

Malmberg et al. 2007, MNRAS, 378, 1207

Malo et al. 2014, ApJ, 788, 81

Marchal, C. 1990, The Three-body Problem (Elsevier)

Marcy G. W., Benitz K. J., 1989, ApJ, 344, 441

Marcy, G. W. & Butler, R. P. 2000, PASP, 112, 137

Marley, M. S. et al. 2002, ApJ, 568, 335

Marley, M. S. & Robinson, T. D. 2015, ARA&A, 53, 279

Marocco, F. et al. 2014, Monthly Notices of the Royal Astronomical Society, Volume 439, Issue 1, p.372-386

Marocco, F. et al. 2010, A&A, 524A, 38

Martín, E. L. et al. 2000, ApJ, 543, 299

Martín E. L., Barrado y Navascu´es D., Baraffe I., Bouy H., and Dahm S. 2003, Astrophys. J., 594, 525-532

Mathieu, R. 1992, IAUS, 151, 21

Mathieu, R., Walter, F., & Myers, P. 1989, AJ, 98, 987

Mayor, M., & Queloz, D. 1995, Nature, 378, 355

Maxted P. F. L. and Jeffries R. D. 2005, Mon. Not. R. Astron. Soc., 362, L45-L49

Maxted et al. 2008, MNRAS, 385, 2210

McCaughrean, M. et al. 2004, A&A, 413, 1029

McLean, I. S., McGovern, M. R., Burgasser, A. J. et al., 2003, ApJ, 596, 561

Mikkola, S. 1983, MNRAS, 203, 1107

Miller, G. E. & Scalo, J. M. 1979, ApJS, 41, 513

Miyama, S., Hayashi, C., & Narita, S. 1984, ApJ, 279, 621

Mizuno, Z. 1980, Prog. Th. Phys., 64, 544

Moeckel & Veras 2012, MNRAS, 422, 831

Mohanty et al. 2004a, ApJ, 609, 854

Mohanty et al. 2004b, ApJ, 609, 885

Monaghan, J. J., & Lattanzio, J. C. 1991, ApJ, 375, 177

Mordasini, C., Alibert, Y., & Benz, W. 2009, A&A, 501, 1139

Morgan WW, Keenan PC, Kellman E. 1943. An Atlas of Stellar Spectra with an Outline of Spectral Classification. Chicago, IL: Univ. Chicago Press

Morley, C. V. et al. 2012, ApJ, 756, 172

Morley, C. V. et al. 2014, ApJ, 787, 78

Nakajima, T., Oppenheimer, B. R., Kulkarni, S. R., et al. 1995, Nature, 378, 463

Nelson, L. A., Rappaport, S., & Chiang, E. 1993, ApJ, 413, 364

Öberg, K. I., Murray-Clay, R., & Bergin, E. A. 2011, ApJ, 743, L16

Oppenheimer, B. R., Kulkarni, S. R., Matthews, K., & van Kerkwijk, M. H. 1998, ApJ, 502, 932

Padoan, P. & Nordlund, A. 2002, ApJ, 576, 870

Padoan, P. & Nordlund, A&A. 2004, ApJ, 617, 559

P´al, A., et al. 2010, MNRAS, 401, 2665

Patience, J., et al. 2002, ApJ, 581, 654

Perryman et al. 1997, A&A, 323L, 49

Pinfield D. J., Dobbie P. D., Jameson R. F., Steele I. A., Jones H. R. A., et al. 2003, Mon. Not. R. Astron. Soc., 342, 1241- 1259

Pinfield, D. J., et al. 2006, MNRAS, 368, 1281

Pinfield, D. J. et al., 2008, MNRAS, 390, 304

Pinfield, D. J. et al. 2012, MNRAS, 422, 1922

Pinfield, D. J. et al. 2013, MmSAI, 84, 1154

Pinfield, D. J. et al. 2014, MNRAS, 444, 1931

Podsiadlowski, P. 1989, PhDT, 38

Pringle, J. E. 1989, MNRAS, 239, 361

Rafikov, R. 2006, ApJ, 648, 666

Raghavan, D., McAlister, H. A., Henry, T. J., et al. 2010, ApJS, 190, 1

Rebolo, R., Martín, E. L., & Magazzù 1992, ApJ, 389L, 83

Rebolo, R., Zapatero Osorio, M. R., & Martín, E. L. 1995, Nature, 377, 129

Rebolo, R., Martín, E. L., Basri, G., Marcy, G. W., & Zapatero Osorio, M. R. 1996, ApJ, 469, L53

Reggiani, M. M. & Meyer, M. R. 2011, ApJ, 738, 60

Reid, I. N., & Gizis, J. E. 1997, AJ, 114, 1992

Reid, I. N., Gizis, J. E., Kirkpatrick, J. D., & Koerner, D. W. 2001b, AJ, 121, 489

Reid I. N., Kirkpatrick J. D., Liebert J., Gizis J. E., Dahn C. C., et al. 2002b, Astron. J., 124, 519-540

Reid, I. N., et al. 2007, AJ, 133, 2825

Reipurth, B. & Clarke, C. 2001, AJ, 122, 432

Rodriguez, D. R et al. 2011, ApJ, 732L, 29

Rogers, P. D. & Wadsley, J. 2012, MNRAS, 423, 1896

Ruzrnaikina, T. V. 1981a, Adv. Space Res, Vol 1, N0 7, 49

Ruzmaikina, T. V. 1981b, Pisma Astr. J. U. S. S. R., 7, 188

Sahlmann, J., Ségransan, D., Queloz, D. et al. 2011, A&A, 525, 95

Salpeter, E. E. 1955, ApJ, 121, 161

Saslaw, W. C., Valtonen, M. J., & Aarseth, S. J. 1974, ApJ, 190, 253

Sasselov, D., & Rucinski, S. 1990, ApJ, 351, 578

Saumon, D. & Marley, Mark S. 2008, ApJ, 689, 1327

Saumon, D. et al 2012, ApJ, 750, 74

Seager, S., Kuchner, M., Hier-Majumder, C. A., & Militzer, B. 2007, ApJ, 669, 1279

Schmidt, S. J. et al. 2010, AAS, 21542426

Schneider et al. 2014, AJ, 147, 34

Scholz, K., Muzic, K., Geers, V. et al. 2012, ApJ, 744, 6

Shu, F. H., Tremaine, S., Adams, F. C., & Ruden, S. P. 1990, Apl, 358, 495

Simon, M., Chen, W. P., Howell, R. R., Benson, J. A., & Slowik, D. 1991, ApJ, in press

Skrutskie, M. F., Cutri, R. M., Stiening, R. et al. 2006, AJ, 131, 1163

Smart, R. L. et al. 2010, A&A, 514A, 84

Sotin, C., Grasset, O., & Mocquet, A. 2007, Icarus, 191, 337

Stahler, S. W. & Palla, F. 2005, The Formation of Stars, pp. 865. ISBN 3-527-40559-3. Wiley-VCH

Stamatellos, D. 2013, in European Physical Journal Web of Conferences, Vol. 47, 8001

Stamatellos, D. 2014, in The Labyrinth of Star Formation, Astrophysics and Space Science Proceedings, Volume 36, 17

Stamatellos, D., Hubber, D. A., & Whitworth, A. P. 2007, MNRAS, 382, L30

Stamatellos, D. & Whitworth, A. P. 2009a, MNRAS, 392, 413

Stamatellos, D. & Whitworth, A. P. 2009b, MNRAS, 400, 1563

Stamatellos, D. & Herczeg, G. J. 2015, MNRAS, 449, 3432

Stauffer, J. R., Hamilton, D., & Probst, R. G. 1994, AJ, 108, 155

Stauffer et al. 2010, PASP, 122, 885

Steele et al. 2009, A&A, 500, 1207

Stephens & Leggett 2004, PASP, 116, 9

Stevenson, D. J. 1982, Ann. Rev. of earth and planetary sc., 10, 257

Stoughton et al. 2002, AJ, 123, 485

Strom, S. 1991, S&T, 82, 18

Struve & Franklin 1955, ApJ, 121, 337

Sumi, T., Kamiya, K., Bennett, D. P., et al. 2011, Nature, 473, 349

Szebehely, V. 1972, AJ, 77, 169

Tamazian et al. 2006, PASP, 118, 814

Tarter, J. C., 1975, The interaction of gas and galaxies within galaxy clusters, Ph.D. Thesis California Univ., Berkeley

Tassoul, J.-L. 1978, Theory of Rotating Stars (Princeton: Princeton University Press)

Torres, G. 1991, Ph. D. dissertation, Cordoba University, Argentina

Tremblay et al. 2011, ApJ, 730, 128

Tsuji, T. 2002, ApJ, 575, 264

Udry, S. & Santos, N. 2007, ARA&A, 45, 397

Valencia, D., Sasselov, D. D., & O'Connell, R. J. 2007, ApJ, 665, 1413

van Biesbroeck 1961, AJ, 66, 528

van Leeuwen 2007, ASSL, 350

Vorobyov, E. I., & Basu, S. 2010, ApJ, 714, L133

Vrba, F. J. et al. 2004, AJ, 127, 2948

Vyssotsky, A. N. 1943 ,ApJ, 97,381

Ward-Duong et al. 2014, MNRAS, 449, 2618–2637

White et al. 2007, AJ, 133, 2524

Whitworth, A. P. & Zinnecker, H. 2004, A&A, 427, 299

Whitworth, A. P. et al. 1995, MNRAS, 277, 727

Wills 1974, MNRAS, 167P, 79

Wilson J. C., Kirkpatrick J. D., Gizis J. E., Skrutskie M. F., Monet D. G., Houck J. R., 2001, AJ, 122, 1989

Winters et al. 2015, AJ, 149, 5

Wootten, A. 1989, ApJ, 337, 858

Wright, E. L., Eisenhardt, P. R. M., Mainzer, A. K. et al. 2010, AJ, 140, 1868

York, D. G., et al. 2000, AJ, 120, 1579

Zapatero Osorio et al. 2004, Ap&SS, 292, 673

Zapolsky, H. S. & Salpeter, E. E. 1969, ApJ, 158, 809

Zhang, Z. H., Pinfield, D. J., Day-Jones, A. C., et al. 2010, MNRAS, 404, 1817

Zuckerman B., Becklin E. E., 1992, ApJ, 386, 260